LATVIAN JOURNAL of PHYSICS and TECHNICAL SCIENCES

ISSN 0868 - 8257

3

SPECIAL ISSUE
(Vol. 59)

2022

CONTENTS

LATVIAN JOURNAL of PHYSICS and TECHNICAL SCIENCES

LATVIJAS FIZIKAS un TEHNISKO ZINĀTŅU ŽURNĀLS

ЛАТВИЙСКИЙ ФИЗИКО-ТЕХНИЧЕСКИЙ ЖУРНАЛ

Published six times a year since February 1964
Iznāk sešas reizes gadā kopš 1964. gada februāra
Выходит шесть раз в год с февраля 1964 года

3 Special Issue (Vol. 59) • 2022

RĪGA

Language Editor: O. Ivanova
Computer Designer: I. Begicevs

INDEXED (PUBLISHED) IN

www.scopus.com
www.sciendo.com
EBSCO (Academic Search Complete, www.epnet.com), INSPEC (www.iee.org.com).
VINITI (www.viniti.ru), Begell House Inc/ (EDC, www.edata-center.com).

Issuers: Institute of Physical Energetics,
Institute of Solid State Physics, University of Latvia
Registration Certificate Number: 000700221

Editorial Contacts:
14 Dzerbenes Street, Riga, LV - 1006
Ph.: + 371 67551732
E-mail: leo@lza.lv
www.fei-web.lv

sciendo

LATVIAN JOURNAL OF PHYSICS
AND TECHNICAL SCIENCES
2022, N 3

THE 7TH INTERNATIONAL SCIENTIFIC CONFERENCE "BALTIC APPLIED ASTROINFORMATICS AND SPACE DATA PROCESSING" (BAASP 2021)

Space science is fundamentally influenced and empowered by computation and information technology and this stimulates its further technological developments. Astronomy, like many other fields, is becoming exponentially data-rich. The tasks of data management, acquisition and mining become central to space research activities, bringing together many technical and methodological challenges. Information technologies also provide the stage where we collaborate and interact, and publish, preserve, use and disseminate knowledge. All the mentioned above makes emerging a new branch of science – astroinformatics.

Recent challenges are directed to more human-orientated, highly personalized and trustworthy systems enabling their users to cope with a large variety of frameworks, technologies, data volumes and tools needed to accommodate emerging scientific applications. Therefore, one of the areas of focus is quantitative and qualitative methods for exploiting, predicting, and understanding the value that information and communication state-of-art technologies bring to space science, astronomy, geodesy and related fields.

The first BAASP conference in August 2012 was successful and it was decided to make these conferences as a regular event. After nine years, the BAASP 2021, the seventh international scientific conference "Baltic Applied Astroinformatics and Space Data Processing (BAASP)" organised by Engineering Research Institute "Ventspils International Radio Astronomy Centre (ERI VIRAC) of Ventspils University of Applied Sciences (VUAS) was held on 23–24 September 2021 in Ventspils, Latvia.

The BAASP conferences are intended as a collaboration platform for cross-border partnership and knowledge transfer in the Baltic regions, as well as in Europe for astronomers, astrophysicists, space researchers, engineers, and experts in related research disciplines in fields, such as informatics, electronics, satellite technology, geodesy and environmental sciences.

While the general scope of BAASP is wide, the specific themes of the BAASP 2021 were astronomy, radio astronomy, space sciences and technologies, instrumentation and data processing, from near Earth space to cosmological distances. Part of the presentations was also dedicated to the modernization and improvement of astronomical and radio astronomical instruments. This year, scientists from Latvia, Russia, Ukraine, Finland, Poland, Sweden, the Netherlands, Italy, Egypt, India, Japan and Greece presented their results. As a result, the conference became not only the European event.

Due to the existing epidemiological constraints, BAASP 2021 took place online using the ZOOM platform. Thanks to the possibility of attending the conference remotely, a significant number of participants from distant counties, such as Japan and India, Greece and the Netherlands, took part. The conference featured 38 presentations, including 32 oral presentations and 6 online posters. 117 participants used the opportunity to register for the conference. As the conference was organised during two days, the total number of participants varied from day to day: on 23 September – 63 and on 24 September – 60 people participated.

It should also be noted that BAASP 2021 not only provided an opportunity to get acquainted with the reports (recorded presentations of the participants' reports are also available online in the VIRAC YouTube channel[1] and BAASP 2021 conference home page[2]), but also provided an opportunity for its participants to establish new personal contacts. For example, researchers from VIRAC were able to show their new scientific results to the wider professional auditory. It also was interesting to hear the discoveries made by researchers from other institutes and observatories around the world, with whom VIRAC had been cooperating for several decades. For example, the conference was attended by representatives from the JIV-ERIC Institute (Netherlands), Lund Observatory (Sweden), Odessa Astronomical Observatory and the Institute of Radio Astronomy of the National Academy of Sciences of Ukraine (Ukraine) and the Nizhny Novgorod Institute of Radiophysics (Russia). The auditory was impressed by the conversion of old Ukrainian and Greek telecommunications antennas to radio astronomical tasks, as well as the involvement of thousands of Indian students in the processing of astronomical data and the search for asteroids (reported by representative of the Science and Technology Department of the Government of Rajasthan). During the conference, the possibility of using artificial intelligence for radio astronomical data processing was also discussed.

The participants of the conference were offered an unique opportunity to participate in a virtual tour of the VIRAC radio telescopes, and even climb to the highest point of the radio telescope RT-32 – the primary focus platform of the antenna, more than 50 m height, as well as visit the Soviet Army underground tunnels and, even going back to the past, to track how radio telescopes changed over the last 15 years of modernization. The record of this excursion is also available on YouTube VIRAC channel[3].

The BAASP 2021 was supported by the project "Support for Preparation of Ventspils University of Applied Sciences International Cooperation Projects in Research and Innovations (ATVASE, No. 1.1.1.5/18/I/009)". We greatly appreciate the efforts of Eva Meijere and Linda Udre for their administration and technical support of the Conference.

Ivar Shmeld,

Chairman of the Scientific and
Local Organising Committee

Vladislavs Bezrukovs,

Vice-Chairman of the Local
Organising Committee

---

[1] https://www.youtube.com/channel/UCWNJkexYySp-Raq7dXJPLJQ/videos

[2] https://www.virac.eu/en/baasp2021

[3] https://www.youtube.com/watch?v=Cq1hWS-i7GU

sciendo

LATVIAN JOURNAL OF PHYSICS
AND TECHNICAL SCIENCES
2022, N 3

DOI: 10.2478/lpts-2022-0019

MICROWAVE OBSERVATIONS OF THE SUN WITH VIRAC RT-32 RADIO TELESCOPE: THE EXPANSION OF POSSIBILITIES

D. Bezrukovs

Engineering Research Institute
"Ventspils International Radio Astronomy Centre",
Ventspils University of Applied Sciences,
101 Inzenieru Str., Ventspils, LV-3601, LATVIA
E-mail: dmitrijs.bezrukovs@venta.lv

Nowadays there is increasing interest in narrowing coronal areas with reduced brightness temperatures (LTR – Low Temperature Regions) associated with local open magnetic fields (S-web, “coronal partings”, “dark coronal corridors”) as one of the eventual sources of slow solar wind. Ventspils International Radio Astronomy Centre (VIRAC) performs routine spectral polarimetric observations of the Sun with RT-32 radio telescope equipped with the multichannel (16 frequency channels) spectral polarimeter for the wave length range of 3.2–4.7 cm (6.3–9.3 GHz) and both circular polarizations simultaneously. The analysis of relevant tasks of clear and reliable observations and detections of LTR shows the necessity to improve noise parameters, dynamic range and stability of the actual solar spectral polarimeter and to expand its wavelength range. Taking into account these requirements, the low noise and thermally stabilized solar spectral polarimeter was developed. The new multi-channel spectral polarimeter is expected to observe right and left circular polarization of the solar emission in the wavelength range of 2.1–7.5 cm (4.1–14.3 GHz) divided into 12 frequency bands. The dynamic range was expanded to >36 db and the signal/noise ratio (referred to as quiet Sun brightness temperatures) was enhanced to > 22–24 db.

The paper deals with some test observations of the newly developed solar spectral polarimeter and its feature analysis. Some eventual problems of solar physics which could be solved with the spectral polarimeter are also discussed.

Keywords: *Radio astronomy, slow solar wind, solar physics, spectral polarimeter.*

1. INTRODUCTION

Microwave spectral polarimetric observations of the Sun still remain one of the main trends in solar physics solving problems of an analysis of plasma parameters and magnetic fields in the chromosphere and lower corona. Since 2013, the RT-32 radio telescope of Engineering Research Institute "Ventspils International Radio Astronomy Centre" (VIRAC) has a possibility to implement routine microwave spectral polarimetric observations of the Sun in a “single dish” mode [5], [6]. These observations are performed using the multi-channel solar spectral polarimeter (SP3) with a frequency range of 6.3–9.3 GHz (3.2–4.6 cm) divided into 16 frequency bands. The result of the observational session of the Sun and the further data processing represent the set of 16 simultaneous 2D Stokes I and V maps of solar brightness temperatures with spatial resolution of 3.9–5.2 arcminutes.

Nowadays there is increasing interest in various coronal hole-like structures (“dark coronal corridor”, “coronal lane”, “coronal partings”, “s-web”) as the eventual sources of slow solar wind [1]–[3], [8]. These areas of interest are observed in X-rays and UV as elongated narrow lanes between coronal holes or peripheries of active regions. Local or global coronal hole-like structures have an evident association with local open magnetic fields [2]–[4], [8], and the reduced plasma densities and kinetic temperatures persist in them due to plasma outflow. In microwaves, coronal holes [7] and coronal hole-like structures could be observed as areas with reduced brightness temperatures below the ordinary brightness temperature of the quiet Sun at a corresponding wavelength (Low Temperature Region – LTR) [4], [8]–[10]. The known microwave observations of LTRs showed its low contrast, and especially a unambiguous detection of LTRs is a rather difficult task in terms of solar radio astronomy. The analysis of conditions of a coronal hole-like structure of microwave emission and the experience of previous solar observations with SP3 spectral polarimeter show a necessity for a fundamental upgrade of the current spectral polarimetric hardware, development of data processing methods and overall improvement of solar observation quality.

The paper provides the description of the newly developed solar spectral polarimeter (Low Noise Spectral Polarimeter ver. 4 – LNSP4) with improved noise parameters and expanded wavelength range of 2.1–7.5 cm, which is expected for further routine observations of the Sun and especially for LTR observations during the solar activity in 2024 or 2025 at the latest.

2. SIMULATION OF MICROWAVE EMISSION OF A “DARK CORONAL CORRIDOR”

In order to work out some requirements for a new solar spectral polarimeter, which could provide actual observations of characteristic LTRs, a number of simple but effective simulations of its microwave emission were done. The example of the cross-section model of a straight “dark coronal corridor” is presented in Fig. 1a. The magnetic field is simulated by two straight wires below the photosphere of the Sun at the ordinary width of “dark coronal corridor”. Plasma parameters of the “corridor” could be presented by two parts: a relatively dense plasma of the quiet Sun outside and a rarified plasma, which ordinarily permits coronal holes inside the "corridor". It is known that photospheric magnetic field inductions of LTRs are weak enough (<20–30 Gs) to consider only the thermal free-free mechanism of the microwave emission overall the "coronal corridor".

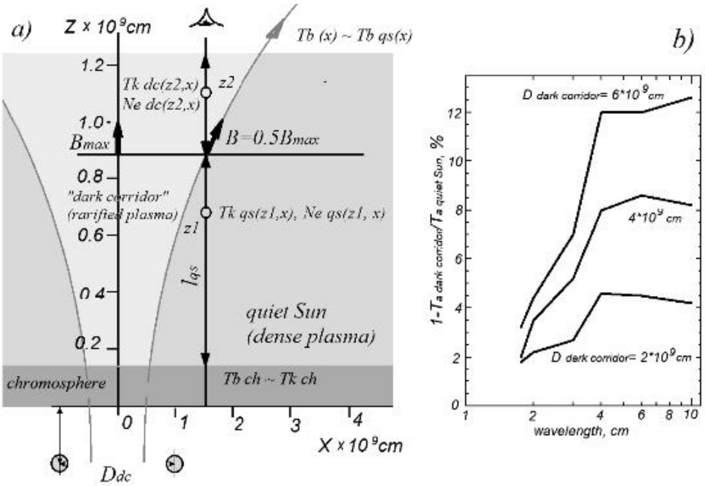

Fig. 1. The model of the cross-section of the strait "dark coronal corridor" (a) and the dependence of the expected reduction of its antenna temperature on the wavelength and the width of "corridor" in percent of the quiet Sun antenna temperature observed with VIRAC RT-32 radio telescope.

The Obridko-Staude distribution of the plasma electron density and kinetic temperature over the height [15] were assumed for the dense plasma of the quiet Sun part along the sight line, and the Borovik model of the atmosphere [7] for coronal holes was used to represent the plasma inside the "corridor". Results of the simulation of brightness temperature distributions across the "corridor" are mainly in accordance with dependencies of quiet Sun and coronal hole brightness temperatures on wavelengths observed with RATAN-600 [7]. Figure 1b presents simulated dependences of the expected LTR contrast (i.e., the reduction of the observed antenna temperature below the quiet Sun one in percent) observed with VIRAC RT-32 radio telescope antenna on microwave emission wavelength and characteristic widths of the "dark coronal corridor".

A number of simulations of the microwave emission of characteristic "dark coronal corridor" proved that the contract of LTRs, i.e., the depression of LTR antenna temperatures observed with the RT-32 antenna in a "single dish" mode, should be expected about some percent (~ 2–4 %) below the quiet Sun ones. Therefore, the possibility of reliable observations of LTRs in microwaves is limited by system noise, its fluctuations and precise measurements and absolute calibrations of actual brightness temperatures of the quiet Sun.

Thus, the main requirements for the new solar spectral polarimeter are the system noise suppression (at least S/N ratio better than 22–24 db) and the implementation of the long-term stability of spectral polarimeter parameters. The actual wavelength range has to be expanded to at least 2.0–8.0 cm.

3. THE MAIN FEATURES OF THE LOW NOISE SPECTRAL POLARIMETER

The low noise spectral polarimeter was developed, designed and produced in 2019 and 2020 according to a list of technical requirements for future routine observations of the Sun with VIRAC RT-32 radio telescope and taking into account the implementation of reliable detection and analysis of LTRs with the contrasts about some percent below quiet Sun brightness temperatures. In March 2021, the spectral polarimeter was delivered to VIRAC and numerous measurements of its parameters and test observations of the Sun were performed till the end of 2021.

The newly developed spectral polarimeter LNSP4 is expected to receive the solar emission of right and left circular polarizations in the frequency range of 4.1–14.3 GHz (2.1–7.5 cm) divided into 12 frequency channels. The distribution of channel frequencies corresponds to the known frequency grid of the RATAN-600 solar spectral polarimeter for the possibility to compare observations.

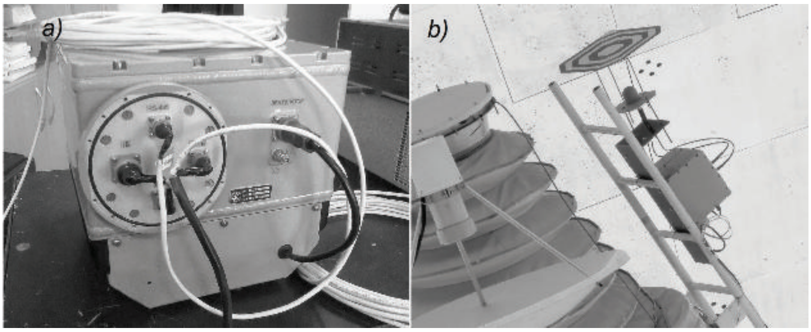

Fig 2. The multi-channel spectral polarimeter LNSP4 unit under tests in the laboratory (a) and the temporary test installation of LNSP4 spectral polarimeter + wide band feed 2-18 GHz + Fresnel lens set onto VIRAC RT-32 radio telescope antenna in the secondary mirror focal plane.

LNSP4 is controlled via the RS485 interface by its own set of commands. Measurements of detected analogue signal of the total channel power are implemented by the same 16 bit ADC which was used for SP3. The CPU unit implements the control of LNSP4 regimes and provides the communication of LNSP4 with the data acquisition and storage system.

The new spectral polarimeter has the thermally stabilized hermetic case, and the separate thermal stabilization system provides an internal temperature of +32–33 °C under the wide range of external temperatures of -30...+40 °C. The precise calibration noise generator with the wide adjustment range is also installed.

The spectral polarimeter LNSP4 under test in the laboratory is presented in Fig. 2a. The main parameters of the LNSP4 and their comparison with the SP3 ones is presented in Table 1. One can see that LNSP4 has the significantly enlarged signal/noise ratio (i.e. the brightness temperature of the quiet Sun referred to as RMS of a system noise track) compared with SP3, an enhanced dynamic range and common sensitivity (the input total power starting the linear power detection for each polarization). Obviously, the thermal stabilization of the case improves overall parameters of LNSP4.

Table 1. The Main Parameters of the LNSP4 and their Comparison with the SP3

	SP3	LNSP4
Frequency range	6.3–9.3 GHz	4.1–14.3 GHz
Number of channels	16	12
Band width	80–100 MHz	250–800 MHz
Polarization	RCP+LCP	RCP+LCP
S/N ratio ($\mathrm{T}quietSun/3*\sigma*\mathrm{T}sysnoise$)	~14–16 db	>22–24 db
Dynamic range	~18–20 db	>36 db
Sensitivity	~72 dbm	<80–82 dbm
Sampling rate	>80 sample/sec	~10 sample/sec
ADC resolution	16 bit	16 bit
Internal thermal stabilization	no	yes
Internal calibration noise generator	no	yes

4. TEST OBSERVATIONS OF THE SUN

Numerous test observations of the Sun with LNSP4 and VIRAC RT-32 antenna were performed to confirm the ability of the new spectral polarimeter to obtain some reliable and adequate observational data. The temporary installation of the spectral polarimeter set onto VIRAC RT-32 antenna is shown in Fig. 2b. The set consists of the spectral polarimeter LNSP4, wide band feed Q-par 2–18 GHz for both circular polarizations, the Fresnel lens prototype, power supplies and the external data and control unit. The Fresnel lens were used to optimize the illumination of the wide band and wide angle feed in the current mirror system. This hardware set was integrated into the antenna control system, the precise time service and the data acquisition and storage system were used for solar observations with the SP3 spectral polarimeter before. The mechanical installation was made with feed spatial offsets from the geometrical axis of the antenna. It caused geometrical distortions of the solar disk image in the focal plane and a kind of chromatic aberration which could be corrected with linear methods. The permanent installation of the LNSP4 spectral polarimeter as the main solar instrument and its integration into a radio telescope common receiving system was expected after the reconstruction of RT-32 central cabin and the mirror system adjustment in 2022.

Some long observations of the sky at all LNSP4 frequency channels were made to evaluate the sensitivity and the common long-term stability of spectral polarimeter parameters. The level of an artificial RFI around the radio telescope was also evaluated. The example of the record of RCP and LCP antenna temperatures for 6.52 cm on almost whole day is shown in Fig. 3. One could make sure that the stability of parameters of the LNSP4 is much better than SP3 at a wide range of external temperatures during the whole day. The sensitivity of the spectral polarimeter is enough to note some fluctuations of clear sky brightness temperatures about ~5–10K. The level of RFI is significant to disturb observations of the Sun and has to be considered in future.

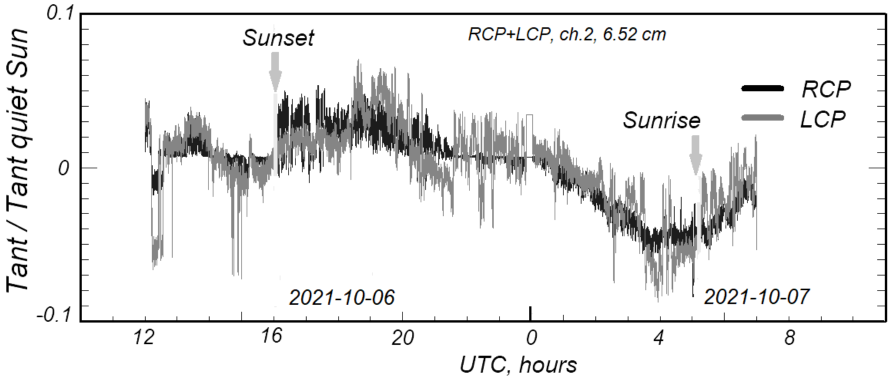

Fig. 3. The record of the clear sky antenna temperature in the zenith at 6.52 cm for RCP and LCP with VIRAC RT-32 radio telescope equipped by LNSP4.

A number of transit records of the Sun for all channels of the spectral polarimeter were carried out. The solar disk came through the antenna beam while the antenna had the preliminary calculated immovable position. Some vertical shift of the antenna beam from the calculated position of the solar disk optical centre was also performed. The main goal of transit observations were measurements of spectral polarimeter common gains, S/N ratio from channel to channel, expected antenna temperatures of the quiet Sun, the adjustment of the current mirror system and the correspondence of the measured HPBWs to calculated ones. Some examples of transit records are shown in Fig. 4. Two weak active regions are presented onto the Sun disk in both cases. The common gain of the spectral polarimeter and noise features are good enough to fix out slight polarization of its and side lobes of the antenna system.

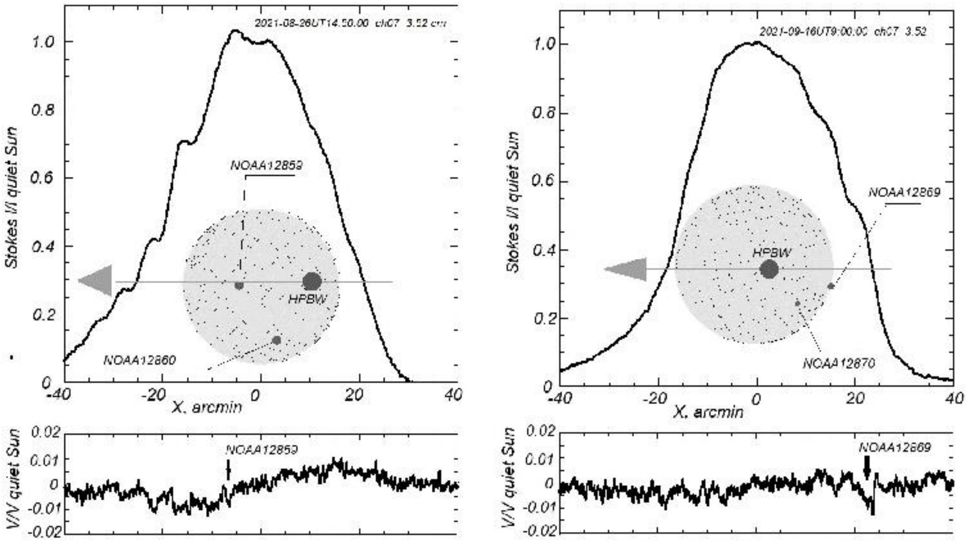

Fig. 4. Some record examples of Sun transit of antenna temperatures at 3.57 cm for Stokes I and V implemented with VIRAC RT-32 radio telescope equipped by LNSP4. Points show the position of active regions on the solar disk on the epoch of observations. The tracks of the antenna beam crossed the centre of the optical solar disk. The relative size of the antenna HPBW is also shown.

The most common task of microwave solar observations for VIRAC is the construction of 2D Stokes I and V maps after the spatial scanning procedure of the solar disk in the screen plane. The series of 2D maps were obtained with the LNSP4 hardware set as well. The scanning procedure was represented by the spiral movement of the antenna beam around the calculated solar disk centre [11]. Further the map was constructed after recalculations of observed samples from a time-antenna position domain to the screen plane by the regularization with bilinear or modified Richardson-Lucy (MLM) methods [12]. Examples of two simultaneous 2D Stokes I maps of antenna temperatures referred to quiet Sun ones at corresponding frequency for two wavelengths are presented in Fig. 5. Maps were constructed without the correction of geometric distortions caused by the spatial shift of the feed electrical axis from geometrical one of the antenna. The analysis of Stokes I map fine structures showed that the quality of the obtained set of maps was sufficient for LTR detection with wavelet analysis methods.

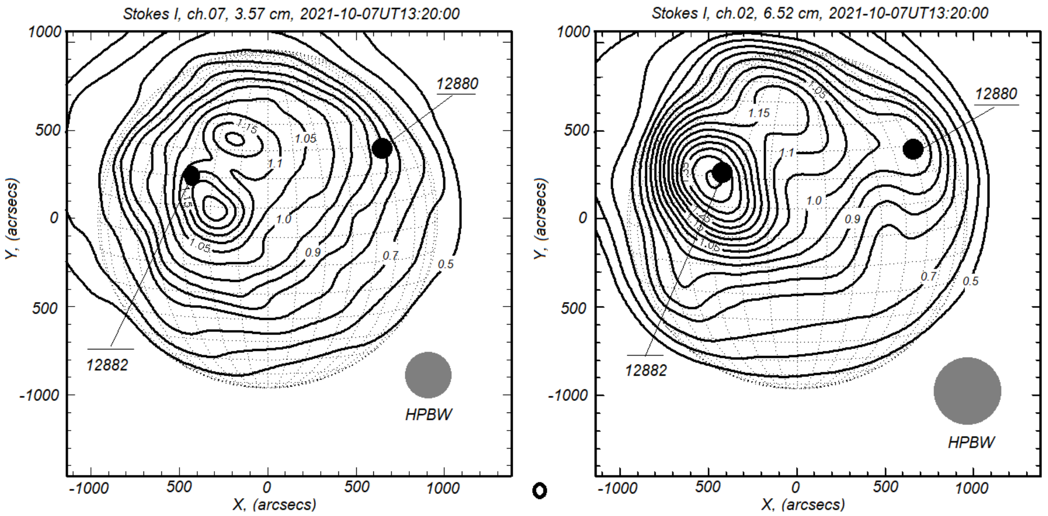

Fig. 5. The example of the 2D distribution of the antenna temperatures Stokes I for 3.57 and 6.52 cm over the solar disk constructed after spiral scanning of the Sun with VIRAC RT-32 radiotelescope equipped with LNSP4. The grid shows the position of the optical disk of the Sun. Points mark the position of active regions on the epoch of observations. Relative size of RT-32 antenna HPBW is shown. Some geometrical distortions of the 2D distribution are caused evidently by known RT-32 antenna misadjustments and spatial shifts of the feed from the geometrical axis of the antenna (chromatic aberration).

5. DISCUSSION

Some solutions of prospective solar physics tasks based on observations of coronal hole-like structures performed by the newly developed spectral polarimeter:

1. Clear and reliable observations and especially adequate detection of coronal areas with reduced brightness temperatures in microwaves for its precise spatial association with local open magnetic fields [8].

2. Studies of a spatial distribution of plasma densities and coronal temperatures in coronal hole-like structures in chromosphere and lower corona based on an analysis of multichannel microwave emission intensities [3].
3. Open magnetic fields magnetography in coronal hole-like structures based on known methods of the polarisation analysis for free-free emissions [13] and polarization inversion of the quasi-transverse propagation of microwave emissions [14].
4. Studies of origins and creation conditions of slow solar wind.

6. CONCLUSIONS

The usage of the newly developed multichannel low noise spectral polarimeter of 2.1–7.5 cm wavelength range offers new possibilities to implement microwave observations of the Sun and significantly improves its adequacy. The permanent installation of the spectral polarimeter hardware set after the reconstruction of the central cabin of the RT-32 radio telescope allows performing regular routine observations of the Sun automatically.

The low noise ratio and the long-term thermal stabilization of the spectral polarimeter parameters are reliable for an adequate observation and precise detection of low contrast coronal hole-like areas with brightness temperatures below quiet Sun ones. The new spectral polarimeter is mainly expected for observations of anticipated coronal hole-like areas at the maximum of the solar activity in 2024–2025 to provide some new studies of spatial structures of eventual sources of slow solar wind.

REFERENCES

1. Nikulin, I. F., & Dumin, Y. V. (2016). Coronal Partings. *Advances in Space Research, 57* (3), 904–911.
2. Antiochos, S.K., Mikic, Z., Titov, V.S., Lionello, R., & Linker, J. A. (2011). A Model of the Sources of the Slow Solar Wind. *The Astrophysical Journal, 731* (2), 1–28.
3. Bezrukovs, D.A., & Ryabov, B.I. (2014). Persistence of Relatively Low Plasma Density in the Atmosphere of Sun Spot. *Latvian Journal of Physics and Technical Sciences, 51* (2), 65–72.
4. Ryabov, B., Bezrukovs, D., & Kallunki, J. (2017). Low Brightness Temperature in Microwaves at Periphery of Some Solar Active Regions. *Latvian Journal of Physics and Technical Sciences*, *54* (3), 58–66.
5. Bezrukovs, D. (2013). Spectral Polarimetric Observations of the Sun by VIRAC RT-32 Radio Telescope: First Results. *Baltic Astronomy, 22* (1), 9–13.
6. Bezrukovs, D., Kallunki, J., & Ryabov, B. (2018) Spectral Polarimetric Observations of the Sun by VIRAC RT-32 Radio Telescope: Calibrations. *Space Research Review,* 5, 1–16.
7. Borovik, V.N., Kurbanov, M.S., Livshits, M.A., & Ryabovy, B.I. (1990). Coronal Holes against the Background of the Quiet Sun: Observations with the RATAN-600 in the 2–32 cm Range. *Astron. J., 67*, 1038–1052.
8. Ryabov, B.I., & Shibasaki, K. (2016). Depressed Emission between Magnetic Arcades near Sunspot. *Baltic Astronomy, 25* (2), 252.
9. Kallunki, J. (2018). Rotation of the Low Temperature regions (LTR) at 8 mm. *Phys. Astron. Int. J., 2* (5), 403–406.

10. Braiša, R., Ruždjak, V., Vršnak, B., Wohl, H., Pohjolainen, S., & Urpo, S. (1999). An Estimate of Microwave Low-Brightness-Temperature Regions Obtained Measuring their Rotation Velocity. *Solar Physics, 184*, 281–296.
11. Mangum, J.G., Emerson, D.T., & Greisen, E.W. (2007). The On-The-Fly Imaging Technique, *A&A, 474*, 679–687.
12. White, R. L. (1994). Image Restoration Using the Damped Richardson-Lucy Method. *Astronomical Data Analysis Software and System III, ASP Conference Series, 61*.
13. Grebinskij, A., Shibasaki, K., & Zhang, H. (1998). Microwave Measurements of the Solar Magnetic Fields at Chromosphere-Corona. *Solar Physics with Radio Observations, Proceedings of Nobeyama Symposium*, NRO report 479, 59–64.
14. Bezrukov, D. A., Ryabov, B. I., Bogod, V. M., Gelfreikh, G. B., Maksimov, V. P., Drago, F., … & Borisevich, T. P. (2005). On the Technique of Coronal Magnetography through Quasi-Transverse Propagation of Microwaves. *Baltic Astronomy, 14* (1), 83–103.
15. Obridko, V.N., & Staude, J. (1988). A Two-Component Working Model for the Atmosphere of a Large Sunspot Umbra. *Astron. Astrophys., 189*, 232–242.

LATVIAN JOURNAL OF PHYSICS
AND TECHNICAL SCIENCES
2022, N 3

DOI: 10.2478/lpts-2022-0020

OBSERVATIONS OF WEAK GALACTIC OH MASERS IN 1.6 GHZ FREQUENCY BAND USING IRBENE RT-32 RADIO TELESCOPE

K. Skirmante*, Vl. Bezrukovs, M. Bleiders, G. Jasmonts,
N. Jekabsons, M. Nechaeva

Engineering Research Institute
"Ventspils International Radio Astronomy Centre",
Ventspils University of Applied Sciences,
101 Inzenieru Str., Ventspils, LV-3601, LATVIA
*e-mail: karina.krinkele@venta.lv

Ventspils International Radio Astronomy Centre (Ventspils University of Applied Sciences) is implementing the scientific project “Complex Investigations of the Small Bodies in the Solar System” (lzp-2018/1-0401) related to the research of the small bodies in the Solar system (mainly, focusing on asteroids and comets) using methods of radio astronomy and signal processing. One of the research activities is weak hydroxyl (OH) radical observation in the radio range – single antenna observations using Irbene RT-32 radio telescope. To detect weak (0.1 Jy) OH masers of astronomical objects using radio methods, a research group in Ventspils adapted the Irbene RT-32 radio telescope working at 1665.402 and 1667.359 MHz frequencies. Spectral analysis using Fourier transform and continuous wavelet transform was applied to radio astronomical data from multiple observations related to weak OH maser detection. Multiple observation sessions of OH maser objects (R LMi, RU Ari, V524 Cas, OH 138.0+7.2, U Aur, etc) were carried out in 2020–2021.

Keywords: *Data processing, radio telescopes, weak OH masers.*

1. INTRODUCTION

The main goal of the research is to determine the lowest possible level of the detection using the radio telescope 1.6 GHz system of Ventspils International Radio Astronomy Centre (VIRAC) and implementing data processing methods with the aim to successfully detect OH masers on comets, which are weak in radio frequency range in the near future. Previous studies [1]–[4] have shown that the typical peak source flux densities of the comet in 1.6 GHz frequency band are in the range of 0.004 Jy to 0.04 Jy, although the flux density of the bright comets OH masers can reach 0.4 Jy [5]. Using radio methods, opposed to optical methods, gives a possibility to clarify comet behaviour near the Sun.

There are four known (1612.231, 1665.402, 1667.359 and 1720.530 MHz) hyperfine transitions of OH at 18 cm wavelength, which have been used for 40 years, historically to observe comets, but only two of them – 1665.402 MHz and 1667.359 MHz – are with potential for the weak object detection because of the RFI in other frequency bands. The 18 cm line is the result of an excitation from resonance fluorescence, whereby molecules absorb solar radiation and then re-radiate the energy. The OH molecule absorbs the UV solar photons and cascades back to the ground state Lambda doublet, where the relative populations of the upper and lower levels strongly depend upon the heliocentric radial velocity (the ‘Swings effect’) [6].

Theoretical estimations of the overall radio telescope 1.6 GHz system were performed before the observation phase and showed the possibility to detect weak objects if the integration time was large enough, but it was necessary to prove the estimations using observations. It should be noted that the radiation of comets has a tendency to decrease, for example, the comet OH brightness usually fades very fast, and the comets are not the best choice for the proof of the estimated calculations. That is why the multiple interstellar OH maser observations were carried out and the choice of targets was done evaluating the target brightness level. For example, the targets with flux densities of around 0.3 Jy and 2 Jy were chosen to simulate bright OH maser on a comet with flux density of ~0.5 Jy.

2. EXPERIMENTAL

Preparation of the Irbene RT-32 radio telescope includes design and installation of the dedicated low-cost L-band (18 cm wavelength) receiver, capable of receiving hyperfine transitions of the interstellar OH masers and the OH masers of comets. A suitable receiver developed by VIRAC team consists of a compact feed horn with dual circular polarized channels and parabolic reflector, which together with existing Cassegrain antenna forms a triple mirror system. Room temperature low noise amplifiers are used for both channels (right and left circular polarization), which allows us to achieve system noise temperatures of less than 60 K. Estimated aperture efficiency at 1.65 GHz is between 30 and 50 %, which translates to RT-32 radio telescope gains of at least 0.1 K/Jy [7]. The overall estimated sensitivity SEFD is between 650 and 900 Jy depending on the elevation of the antenna, and the weak object detection could be a challenging task. The main activities to increase the overall sensitivity were related to implementation of effective methods during the data recording and processing steps.

The theoretical estimations of the sensitivity level of Irbene RT-32 1.6 GHz system were carried out before the observations. The main research goal was to adapt RT-32 radio telescope for comet OH maser detection, but at the beginning of the research it was necessary to check RT-32 readiness level for weak object observations using more stable objects, for example, interstellar OH masers. Weakness of the radio signal of a comet OH maser is the main challenging factor. The calculated results of the noise floor dS vs. integration time showed that the detection of the source with the flux density below 0.4 Jy was possible by RT-32 antenna if integration time was larger than 8 hours and total power bandwidth (BW) – 10 KHz [8].

A spectrometer backend based on software defined radio USRP X300/310+TwinRX is applied to record data using 16 bit + 16 bit (real + imaginary part) per sample [9]. For spectral data calibration, the frequency switching method [10] is currently used and the object is observed in 4 phases: local oscillator with noise diode on/off and reference local oscillator with noise diode on/off. This allows calculating the system temperature, which together with position and degrees per flux unit gives us a spectrum of spectral flux density. To improve time resolution, data are overlapped (in this case with a 66.1 % overlapping coefficient which was chosen for its effectiveness [11]), creating bins of data, which must be processed using Fourier transform with the addition of Blackman-Harris windowing function. Each bin results in an individual spectrum and, to get the result, all spectrums are averaged. To prevent numerous technical errors, it is important to monitor the system temperature in order to check for anomalies in data. Since data are still valid for the part where the read system temperature is invalid, it is possible to predict potential system temperature values for a specific time moment. In this system, it is implemented using wavelet transformation, a low precision wavelet to get the shape of the spectrum, and replacing an incorrect value by the predicted value. Data processing is implemented to collect data using long integration time and to calculate the spectrum of the object. To decrease the noise level of the spectrum, the multiple observation sessions were combined.

3. RESULTS

To verify calculations of the estimation model and to evaluate the RT-32 radio complex sensitivity level, multiple observations of interstellar OH masers in 1.6 GHz were performed. To check RT-32 readiness level for weak object observations, the observations of variable star R LMi (spectrum shown in Fig. 1), OH/IR star Ru Ari (spectrum shown in Fig. 2), variable star U Aur (spectrum shown in Fig. 3), OH/IR star OH 138.0 +7.2 (spectrum shown in Fig. 4), variable star V524 Cas were carried out.

Table 1 lists the observed objects and their parameters. The first four columns include the source name, source type and J2000 equatorial coordinates. In the fifth column, the observation lines are shown. The sixth column contains the flux density at the total intensity peak or peaks (if the spectrum consists of multiple parts), together with the noise level (1σ). The seventh column shows hours needed for detection ~3σ or ~2σ for weaker objects. The eighth column gives the velocity of peak flux density.

Table 1. The Obtained Results of Weak OH Maser Observations Using RT-32 and 1.6 GHz Receiver.

Name	**Type**	**RA**	**Dec**	**Line (MHz)**	**Flux density peak/s (RMS level) in Jy**	**Hours needed for detection with ~3σ**	**V(LSR), km/s**
R LMi	Variable Star of Mira Cet type	09 45 34.28	34 30 42.83	1665 1667	3.22 and 1.95 (0.12) 2.92 and 2.16 (0.12)	2h 2h	-4.01, 4.22 -4.14, 4.63
Ru Ari	OH/IR star	02 44 45.50	12 19 02.89	1665 1667	0.60 (0.3) 1.76 and 0.78 (0.5)	12h (2σ) 6h and 10h	22 25.00, 22.25
U Aur	Variable Star of Mira Cet type	05 42 09.06	32 02 23.58	1665 1667	0.43 (0.2) 0.28 (0.2)	22h (2σ) 22h (2σ)	3.47 3.03
OH 138.0 +7.2	OH/IR star	03 25 08.40	65 32 07.06	1665 1667	no detection (0.3) 1.72 and 0.6 (0.3)	16 h observed 6h and 16h	- -46.15, -27.63
V524 Cas	Variable Star of Mira Cet type	00 46 00.13	69 10 53.63	1665 1667	no detection no detection	26 h observed 26 h observed	- -

Three out of five objects were detected successfully in both frequencies, although the SNR in the weaker signals was ~2σ. The characteristics of the spectra and the obtained velocities were compared with results from scientific publications [12]–[14] and maser.db [15]. The obtained results were verified and considered correct. Target OH 138.0 +7.2 was detected only at 1.667 GHz, but the previous research showed that in other observatory observations the detection at 1.665 GHz was not clear. Although variable star V524 Cas was not detected at any frequency band, this could be explained by the fact that the magnitude of the variable star decreased compared to previous observations in 1999, when the flux densities were 0.2 Jy (at 1665 MHz frequency) and 0.1 Jy (at 1667 MHz frequency) [16].

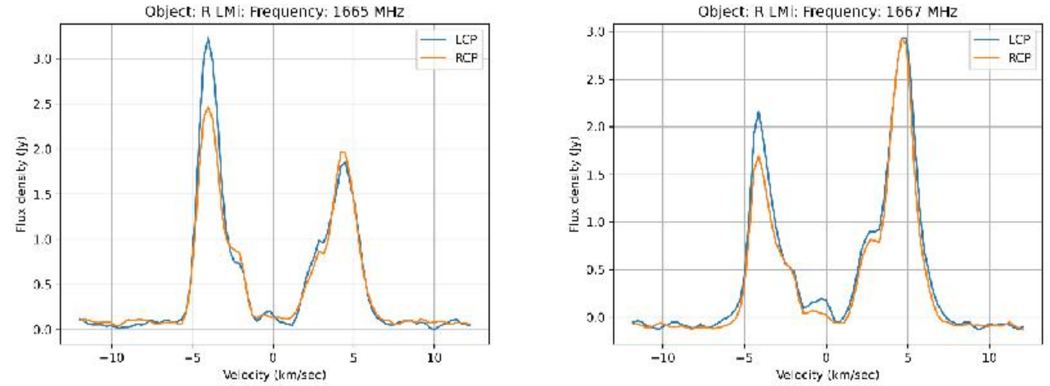

Fig. 1. Object – variable star R LMi. Frequency – 1665 MHz (left side) and 1667 MHz (right side). Polarisation – left circular polarisation (in blue) and right circular polarisation (in orange).

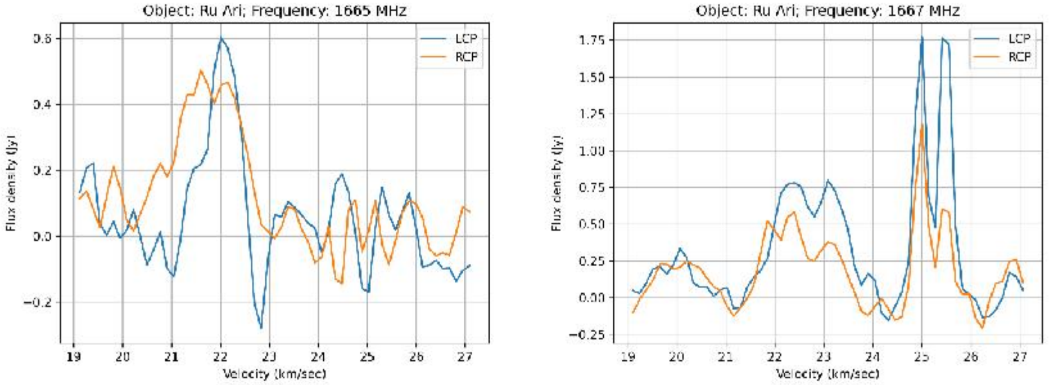

Fig. 2. Object – OH/IR star Ru Ari. Frequency – 1665 MHz (left side) and 1667 MHz (right side). Polarisation – left circular polarisation (in blue) and right circular polarisation (in orange).

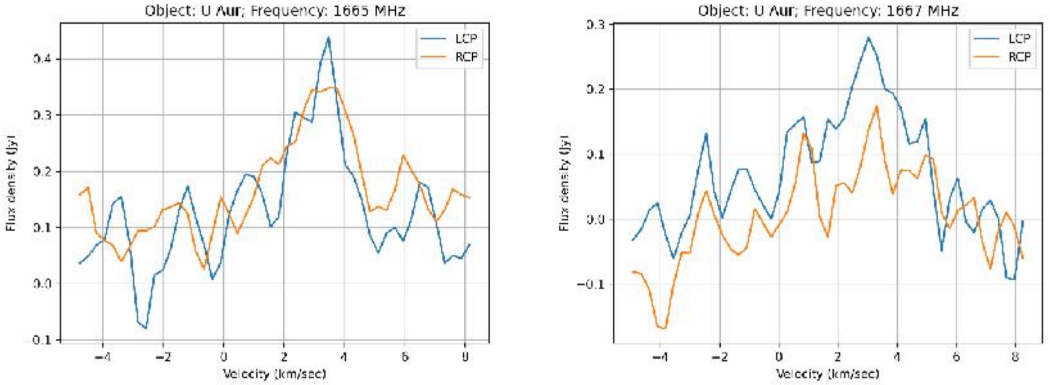

Fig. 3. Object – variable star U Aur. Frequency – 1665 MHz (left side) and 1667 MHz (right side). Polarisation – left circular polarisation (in blue) and right circular polarisation (in orange).

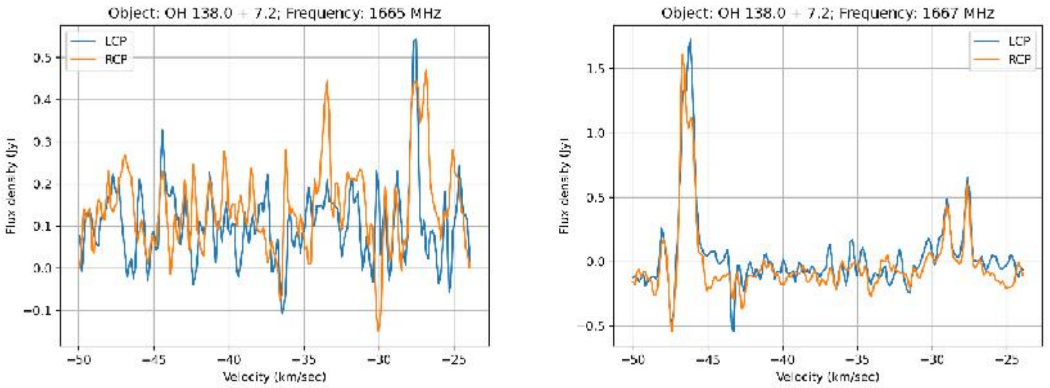

Fig. 4. Object – OH star OH 138.0 + 7.2. Frequency – 1665 MHz (left side) and 1667 MHz (right side). Polarisation – left circular polarisation (in blue) and right circular polarisation (in orange).

The results of the first observations of variable Star of Mira Cet type R LMi showed successful detection at both frequencies and R LMi was chosen as a calibrator target for other observations as well. Overall, the data set of R LMi consists of 50 hours of observation data. The spectra of both data sets are shown in Fig. 5, where the noise level of the 2-hour dataset is ~ 0.52 Jy, but the noise level of the 50-hour dataset is 0.10 Jy, which is promising to detect OH masers on bright comets. Figures 6 and 7 show results of the applied methodology if the radiation of the observed target is weak. Results of the 2-hour dataset processing are not clear because of the high SNR, but usage of multiple data processing methods reduces SNR; thus, the object can be detected.

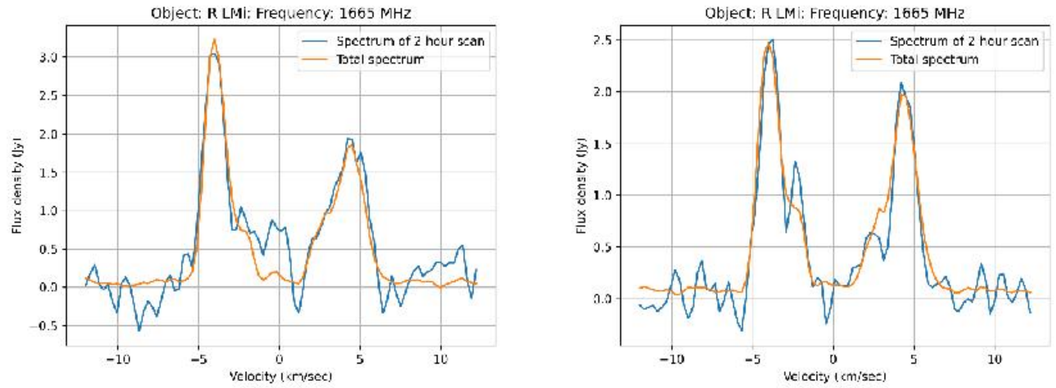

Fig. 5. Object – variable star R LMi, frequency – 1665 MHz, polarisation – left circular polarisation (left side) and right circular polarisation (right side). Spectrum of the 2-hour dataset is shown in blue, spectrum of 50-hour dataset – in orange.

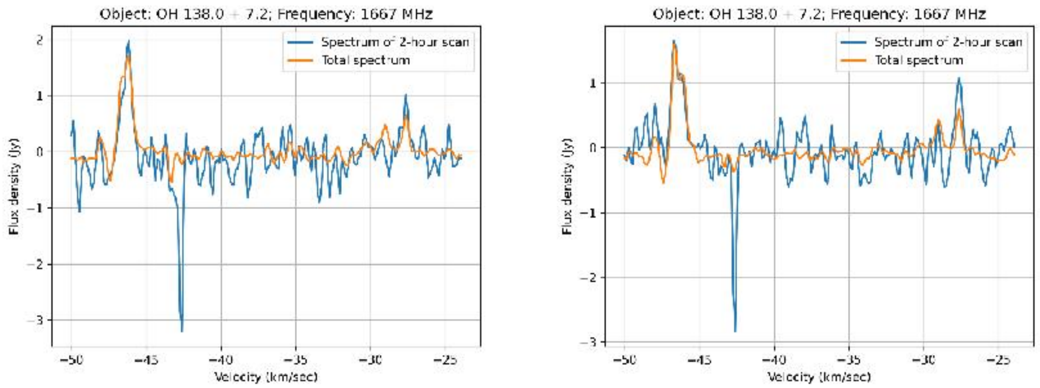

Fig. 6. Object – OH star 138.0+7.2, frequency – 1667 MHz, polarisation – left circular polarisation (left side) and right circular polarisation (right side). Spectrum of 2-hour dataset is shown in blue, spectrum of 16-hour dataset – in orange.

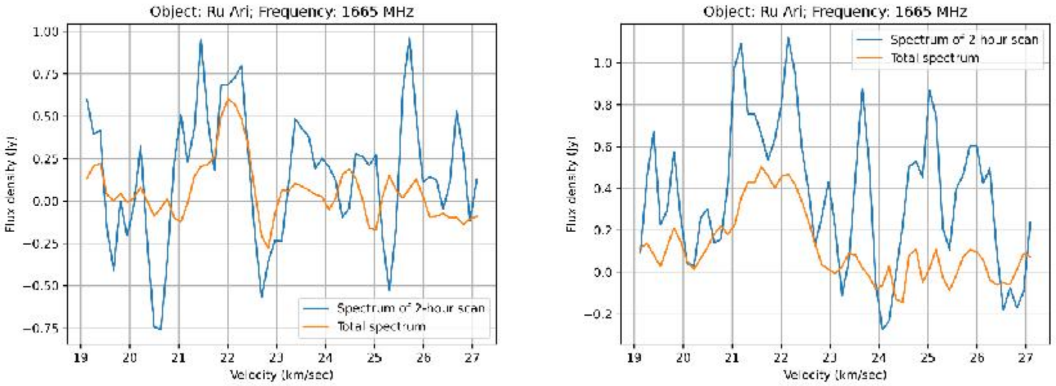

Fig. 7. Object – OH/IR star Ru Ari, frequency – 1665 MHz, polarisation – left circular polarisation (left side) and right circular polarisation (right side). Spectrum of 2-hour dataset is shown in blue, spectrum of 12-hour dataset – in orange.

Based on the processed observation data and the corresponding results, it is concluded that practically the sensitivity level is 6.7 times larger than estimation in the theoretical model. This can be explained by receiver stability loss during the long-term observations, in a pair with random drift of system temperature. For example, to detect targets with the flux density of ~0.4 Jy, more than 22 hours are needed, for ~0.04 Jy detection – more than 300 hours are needed, which is cost ineffective to use radio telescopes for the observations of comet OH maser.

4. CONCLUSIONS AND FUTURE WORK

The developed flux detection threshold estimation model, which is related to noise floor dS vs integration time, shows that the detection of the source with the flux density below 0.4 Jy is possible using radio telescope RT-32 complex if the spectral channel bandwidth is small and integration time is large [8]. Practically, existing RT-32 1.6 GHz receiver and data processing methods allow identifying the weak OH masers with emission being below 0.4 Jy. The expected increase in sensitivity of RT-32 radio complex after planned modernization (by 2023) seems to be essential to measure delay and frequency of interference using hyper-fine transitions of OH molecules. This study combined with previous experience on acquiring and processing data from the DA14 asteroid [17] (15 February 2013) offers a good starting point for further development. The ultimate goal is to achieve a fine OH maser location of the comet approaching the Sun.

Also, more effective data processing tools can be used, for example, weak OH signal filtration from background noise using the Karhunen–Loève Transform (KLT) for detection and RFI identification, isolation, and removal. KLT provides the ability to extract weak signals from background noise better than FFT. In several examples, the FFT algorithm was unable to detect signal from the noise with SNR = -23 dB, even though the KLT could achieve it [18], [19]. Also practical studies show the difference between only FFT usage and KLT and FFT usage where generated 60 Hz signals with different SNR levels were applied, but, in summary, KLT detection level was -39db, but FFT only -25db. KLT can be used for time-independent random functions, which allows multiple non-sequential radio astronomy datasets to be processed, in this case, in large integration time.

Further research can deal with the comparison of radio and optical observations for the same events on the same comets in order to get further insight into the physics of both interstellar OH masers and comets.

ACKNOWLEDGEMENTS

The research has been funded by the Latvian Council of Science, project “Complex Investigations of the Small Bodies in the Solar System”, project No. lzp-2018/1-0401.

REFERENCES

1. Crovisier, J., Colom, P., Biver, N., Bockel´ee-Morvan, D., & Boissier, J. (2013). Observations of the 18-cm OH Lines of Comet 103P/Hartley 2 at Nancay in Support to the EPOXI and Herschel Missions. *Icarus, 222* (2), 679– 683.
2. Lovell, A. J., Howell, E. S., Schloerb, F. P., Lewis, B. M., & Hine, A. A. (2002). Arecibo observations of the 18 cm OH lines of six comets. In B. Warmbein, ed., *Asteroids, Comets, and Meteors*: *ACM 2002*, vol. 500 of ESA Special Publication, (pp. 681–684).
3. Turner, B. E. (1974). Detection of OH at 18-CENTIMETER Wavelength in Comet Kohoutek (1973f). *Astrophysical Journal, 189*, L137–L139.
4. Volvach, A. E., Berezhnoi, A. A., Volvach, L. N., Strepka, I. D., & Volvach, E. A. (2011). Observations of OH Maser Lines at an 18-cm Wavelength in 9p/Temper1 and Lulin c/2007 n3 Comets with rt-22 at the Crimean Astrophysical Observatory. *Bulletin of the Crimean Astrophysical Observatory, 107* (1), 122–124.
5. Crovisier, J. (2021). *Results from the Nançay Database of OH 18cm Lines in Comets*. Available at https://lesia.obspm.fr/planeto/cometes/basecom/

6. Despois, D., Gerard, E., Crovisier, J., & Kazes, I. (1981). The OH Radical in Comets – Observation and Analysis of the Hyperfine Microwave Transitions at 1667 MHz and 1665 MHz. *Astronomy and Astrophysics, 99*, 320–340.
7. Bleiders, M., Berzins, A., Jekabsons, N., Skirmante, K., & Bezrukovs, Vl. (2019). Low-Cost L-Band Receiving System Front-End for Irbene RT-32 Cassegrain Radio Telescope. *Latvian Journal of Physics and Technical Sciences, 56* (3), 50–61.
8. Skirmante, K., Eglitis, I., Jekabsons, N., Bezrukovs, V., Bleiders, M., Nechaeva, M., & Jasmonts, G. (2020). Observations of Astronomical Objects Using Radio (Irbene RT-32 Telescope) and Optical (Baldone Schmidt) Methods. *Astronomical and Astrophysical Transactions, 32* (1), 13–22.
9. Bleiders, M., Antyufeyev, O., Patoka, O., Orbidans, A., Aberfelds, A., Steinbergs, J., … & Shmeld, I. (2020). Spectral Line Registration Backend Based on USRP X300 Software Defined Radio. *Journal of Astronomical Instrumentation, 9* (2), 2050009.
10. Winkel, B., Kraus, A., & Bach, U. (2012). Unbiased Flux Calibration Methods for Spectral-Line Radio Observations. *Astronomy and Astrophysics, 540*, A140.
11. Heinzel, G., Rüdige, A., & Schilling, R. (2002). *Spectrum and Spectral Density Estimation by the Discrete Fourier Transform (DFT), Including a Comprehensive List of Window Functions and Some New Flat-Top Windows.* Available at https://holometer.fnal.gov/GH_FFT.pdf
12. Lewis, B. M. (1997). Main-line OH Observations of the Arecibo Set of OH/IR Stars. *Astrophysical Journal Supplement Series, 109,* 489È515.
13. Fix, J. D., & Weisberg, J. M. (1978). A Low-Detection Limit Search for OH Emission from the Infrared Stars. *The Astrophysical Journal, 220*, 836–840.
14. Wolak, P., Szymczak, M., & Gérard, E. (2012). Polarization Properties of OH Masers in AGB and Post-AGB Stars. *A&A, 537*, A5. doi: 10.1051/0004-6361/201117263.
15. Sobolev, A. M., Ladeyschikov, D. A., & Nakashima, J. (2019). Database of Molecular Masers and Variable Stars. *RAA, 19* (3), 34. doi: 10.1088/1674–4527/19/3/34.
16. Szymczak, M., & Le Squeren, A. M. (1999). A Comparison of OH and H2O Maser Properties of Mira and Semiregular Variable Stars. *Mon. Not. R. Astron. Soc., 304* (2), 415–420.
17. Nechaeva, M., Antipenko, A., Bezrukov, D., Bezrukovs, Vl., Dementjev, A., Dugin, N., … & Voytyuk, V. (2013). First Results of the VLBI Experiment on Radar Location of the Asteroid 2012 DA14. *Baltic Astronomy, 22,* 341–346.
18. Trudu, M., Pilia, M., Hellbourg, G., Pari., P., Antonietti, N., Maccone, C., … & Trois, A. (2020). Performance Analysis of the Karhunen–Loeve Transform for Artificial and Astrophysical Transmissions: Denoising and Detection. *MNRAS, 494*, 69–83. doi:10.1093/mnras/staa694
19. Maccone, C. (2010). The KLT (Karhunen–Loeve Transform) to Extend SETI Searches to Broad-Band and Extremely Feeble Signals. *Acta Astronautica, 67* (11–12), 1427–1439.

LATVIAN JOURNAL OF PHYSICS
AND TECHNICAL SCIENCES
2022, N 3

DOI: 10.2478/lpts-2022-0021

RADAR OBSERVATIONS OF OLD CENTAUR ROCKET FROM 1966

Yu. Bondarenko*, D. Marshalov

Institute of Applied Astronomy, Russian Academy of Sciences,
10 Kutuzova Embarkment, St.Petersburg, 191187, RUSSIA
*e-mail: bondarenko@iaaras.ru

We report the results of radar observations of a near-Earth object discovered on 17 September 2020, with the Pan-STARRS 1 telescope at the Haleakala Observatory in Hawaii. Initially, this object was considered an asteroid and even received the standard provisional designation 2020 SO by the Minor Planet Center. However, its Earth-like orbit and low relative velocity suggested that the object may be of artificial origin, being the Centaur rocket booster from the Surveyor 2 mission that was launched to the Moon on 20 September 1966. In the period from November 2020 to March 2021, this object approached the Earth twice within one lunar distance of the Earth. Radar observations were conducted on 30 November in bistatic mode with the 70-m Goldstone Solar System Radar DSS-14 and 32-m radio telescope RT-32 at the Svetloe Observatory, while the object was in the visibility window of two antennas at about 200 thousand km from the Earth. The main goal of the study was to determine the physical properties of this object using radar astronomy to clarify its origin.

Keywords: *Near-Earth objects, radar observations, spacecraft, space debris.*

1. INTRODUCTION

On 17 September 2020, one unusual near-Earth object was discovered by the Pan-STARRS 1 telescope at the Haleakala Observatory on the island of Maui. At first, it was assumed that this is an ordinary asteroid approaching the Earth, so the object received the standard designation 2020 SO by the Minor Planet Center [1]. On 8 November 2020, the object was temporarily captured by the Earth's gravity and made two large eccentric orbits around the Earth–Moon system, leaving Hill's sphere in March 2021. During this interval, the object twice approached the Earth on 1 December

2020 at 0.13 lunar distances (LD) and on 2 February 2021 at 0.58 LD. Figure 1 shows the temporary orbit of 2020 SO around the Earth from September 2020 to May 2021.

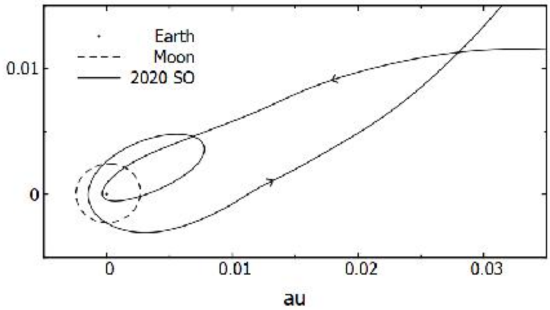

Fig. 1. The orbital trajectory of 2020 SO (solid line) relative to the Earth from September 2020 to May 2021 in projection onto the ecliptic plane. The arrows show the direction of motion, while the dashed line represents the orbit of the Moon.

However, the fact that 2020 SO had a low relative velocity of ~0.6 km/s, and its orbit around the Sun was very similar to that of the Earth, led to doubts that it was an ordinary asteroid. An analysis of additional observations showed a significant effect of solar radiation pressure on the 2020 SO trajectory, confirming its low-density nature, which was not typical of asteroids. The assumption that 2020 SO was a remnant of an old space mission was made by the director of the Center for Near-Earth Object Studies (CNEOS) at NASA's Jet Propulsion Laboratory Paul Chodas [2]. He found that this object came close enough to the Earth in late 1966, coinciding with the launch of the Surveyor 2 mission.

The Surveyor 2 lunar lander was launched from Cape Canaveral on 20 September 1966, on an Atlas-Centaur rocket. Immediately after the launch, Surveyor 2 separated from its Centaur upper-stage rocket booster, heading towards the Moon, and the spent upper-stage ended up into an unknown orbit around the Sun. Figure 2 shows Centaur upper-stage before being assembled with the Atlas rocket and during the launch of NASA's Surveyor 2 moon lander on top of the Atlas-Centaur rocket. It was made of stainless steel and had a cylindrical shape with a height of 9.6 meters and a diameter of 3.05 meters.

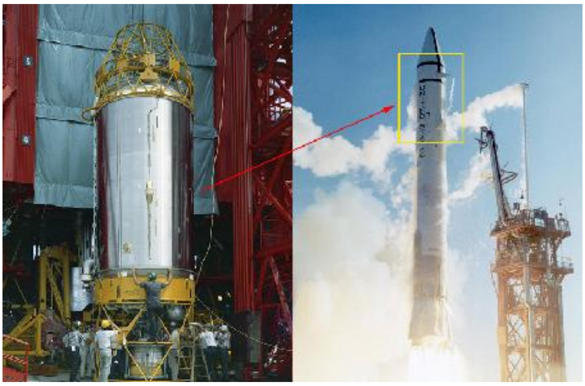

Fig. 2. Centaur upper-stage rocket booster (left) and launch of NASA's Surveyor 2 moon lander a top of Atlas-Centaur rocket (right). Credits: NASA.

Over the past 20 years, at least four human-made objects have received asteroid designations [3]–[6]. The ability to distinguish between natural and artificial objects is important, as countries continue to increase research in space, and more artificial objects are in orbit around the Sun. Today radar astronomy is one of the most precise methods to obtain information about the dynamic and physical properties of near-Earth objects. The size, shape, spin period and surface properties can be obtained with radar observations. The principal goal was to obtain the physical properties of near-Earth object 2020 SO using radar astronomy to understand whether it is a natural object or an old rocket body.

2. RADAR OBSERVATIONS

Radar observations were carried out in cooperation with the Asteroid Radar Research group from the Jet Propulsion Laboratory. Observations involved the 70-meter diameter antenna (DSS-14) of the Goldstone Deep Space Communications Complex and the 32-meter diameter radio telescope (RT-32) at the Svetloe observatory. The parameters of the radio telescopes used in the observations are provided in Table 1. Due to the close approach distances, the observations were carried out in bistatic mode with transmission at DSS-14 and reception at RT-32. We used this mode because the round-trip signal time (RTT) to the target and back was about 1.4 s, which was half the time it took to switch from transmitting to receiving at DSS-14.

Table 1. Radio Telescopes Used in the Observations

UT Date	**DSS-14**	**Svetloe (RT-32)**
Geographical coordinates	35.4258° N, 116.8895° W	60.5343° N, 29.7794° E
Diameter, m	70	32
Aperture efficiency	0.64	0.56
Transmitter frequency, MHz / cm	8560 / 3.5	NA
Transmitter power, kW	440	NA
System temperature, °K	18	52

We observed 2020 SO on 30 November, while the object was in the visibility window of two antennas at about 203 thousand km from the Earth near to its closest approach on 1 December. First DSS-14 transmitted 440 kW circularly polarized continuous wave (CW) at a carrier frequency of 8560 MHz (3.5 cm) and then modulated the transmitted carrier with a repeating pseudo-random code using binary phase coding (BPC). RT-32 antenna received echoes simultaneously in the same circular (SC) and opposite circular (OC) polarizations as transmitted, sampled them and recorded. Table 2 lists the observing start and stop times with the corresponding round-trip signal times, length of the pseudo-random code used, duration of each code element (or baud) and the range resolution of corresponding setup.

Table 2. Masterlog of Radar Observations of 2020 SO

UT Date	Start-Stop hh:mm:ss – hh:mm:ss	RTT s	Setup	Code	T_{baud} μs	δr m
30 Nov 2020	04:56:15–05:14:40	1.37	CW	–	–	–
	05:17:52–05:21:47	1.37	BPC	127	10	1500
	05:23:37–05:37:30	1.36	BPC	127	1	150
	05:37:39–05:50:52	1.35	BPC	127	0.125	19
	06:05:00–06:25:45	1.33	BPC	127	0.125	19

We used a monochromatic continuous wave to measure the total power of the echo, its frequency and Doppler broadening. The modulated carrier was used to resolve the target in two dimensions – time-delay (or range) and frequency (or Doppler shift) forming a range-Doppler radar image. The range resolution along the line-of-sight depends on the selected baud duration and the frequency resolution depends on the fast Fourier transform (FFT) length or integration time.

3. DATA PROCESSING RESULTS

We cross-correlated the PBC echo time series with a replica of the transmitted code and applied FFT in each range bin to obtain range-Doppler images (Fig. 3). A series of images in Fig. 3 are arranged in chronological order and correspond to one of four object rotational phases, repeating with a period of about 9.5 sec. The integration time of each image is a half second. Range (distance from the observer) increases down at 19 m per pixel and Doppler frequency increases to the right at 10 Hz per pixel.

The radar images show that the entire object fits within one range bin. This suggests that the selected modulation mode did not allow the object to be resolved in range, since the size of 2020 SO did not exceed 19 meters. However, the frequency resolution allowed us to accurately estimate the dimensions of this object.

If the transmitted signal is reflected from a rotating target, one part of which is approaching the observer, and the other recedes, then the signal is broadened due to the Doppler effect. From the obtained series of images, we estimated the Doppler broadening, which varied from 100±10 Hz to 400±10 Hz during the object's rotation phase. For a spherical object, the echo bandwidth B is given by:

$$B = \frac{4\pi D(\phi)}{\lambda P} \cos\delta,$$

where $D(\phi)$ is the diameter (breadth) of the object at rotation phase ϕ; λ is the transmitted wavelength; P is its rotation period, and δ is an angle between the observer line-of-sight and the object's apparent equator. Considering the rotation period of P=9.5 sec and assuming $\delta = 0°$ we obtained that the size of 2020 SO varied from 2.6±0.2 m to 10.6±0.2 m depending on the rotation phase. This indicates that the object has an elongated shape with the ratio of 4:1.

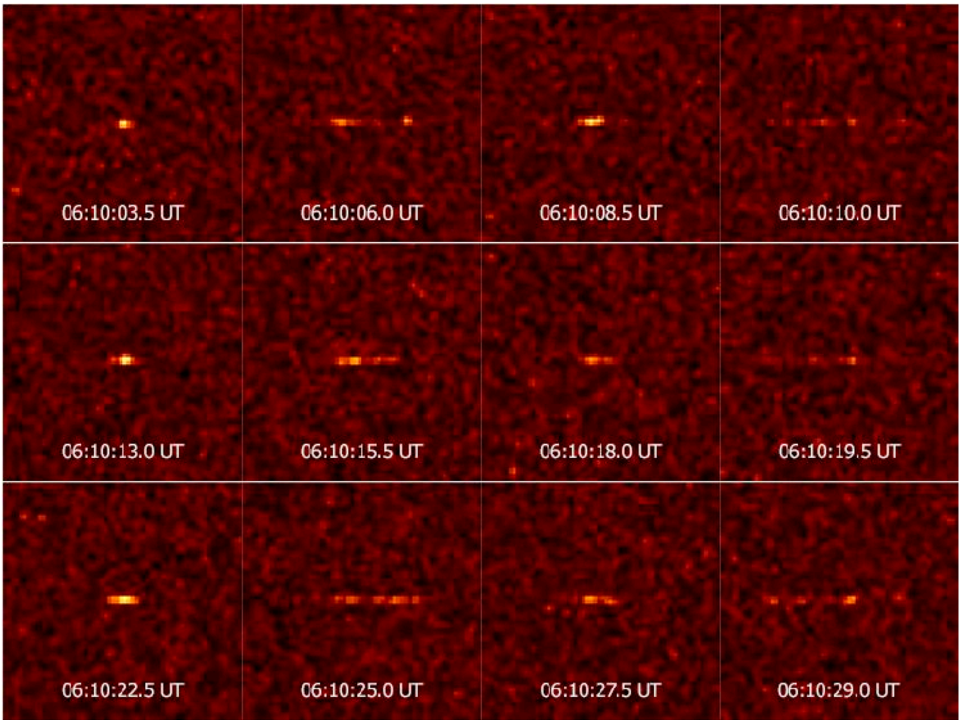

Fig. 3. A series of range-Doppler radar images of near-Earth object 2020 SO on 30 November 2020 showing three complete rotations.

Considering the Doppler frequency as a function of time, we applied FFT to the 10 second of CW echo time series to obtain echo power spectra of 2020 SO (Fig. 4). Echo power is plotted in standard deviations of the background noise versus Doppler frequency. The frequency resolution Δf is 10 Hz. Zero frequency in the figure corresponds to the frequency calculated for the object's center of mass. Solid and dashed lines show OC and SC spectra, respectively.

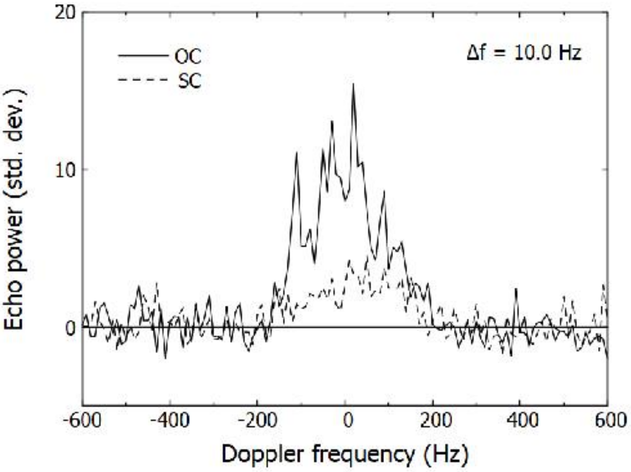

Fig. 4. Continuous wave echo power spectra of 2020 SO obtained on 30 November 2020, from 05:00:02 to 05:00:12 UT.

Circular polarization of the signal is reversed after reflection from the plane surface and the maximum power of the reflected signal is expected in the OC polarization, though some of the signal, due to multiple reflections or scattering from a rougher surface is received in the SC polarization. Therefore, a higher SC/OC ratio indicates a greater degree of near-surface wavelength-scale roughness or multiple scattering. We estimated the circular polarization ratio of ~0.31, which suggested that the surface of 2020 SO had irregularities responsible for multiple signal reflections on a centimeter scale.

The signal-to-noise ratio (SNR) of the received echo can be estimated as the ratio of the received echo power P_{rx} to the standard deviation of the receiver noise ΔP_{noise} using the radar equation [7]:

$$SNR = \frac{P_{rx}}{\Delta P_{noise}} \sim \frac{P_{tx} G_{tx} A_{rx} \sigma}{T_{sys} R^4} \sqrt{\Delta\tau / B},$$

where P_{tx} is the transmitted power, G_{tx} is the transmitting antenna gain, A_{rx} is the receiving antenna effective aperture, T_{sys} is the receiver temperature, σ is the radar cross-section of the target, B and $\Delta\tau$ are the bandwidth and integration time of the echo signal.

By integrating the OC continuous wave echo power spectra in Fig. 4 and using data from Table 1, we obtained the radar cross-section of σ=17.6 m^2. The radar cross-section is given by $\sigma=\hat{\sigma}A$, where $\hat{\sigma}$ is the radar albedo and A is the projected area of the target. Albedo indicates the radar reflectivity of a surface compared to a perfectly reflective isotropic scatterer. If 2020 SO is a rotating cylinder that is 10 m long and 3 m in radius, then its OC radar albedo can be estimated at about 95 %, which indicates a high reflectivity of its surface in the radio range, typical of metals.

4. CONCLUSIONS

On 1 December, when 2020 SO made its closest approach to the Earth, several observatories reported the rotation period of the object from photometric observations to be 9.4 seconds [8], [9], and an amplitude of about 2.5 magnitude suggests a 10:1 ratio between the maximum and minimum dimensions of the object, which is in good agreement with radar results.

In late November, a team from the University of Arizona performed spectroscopy observations of 2020 SO using NASA's Infrared Telescope Facility (IRTF). They compared the obtained near-infrared spectrum with the spectra of another old Centaur D rocket, which had been in geostationary orbit from 1971. It turned out that obtained spectra are consistent with each other, thus finally concluding that 2020 SO is also a Centaur rocket booster [10].

As a result of radar observations, the rotation period of 2020 SO was determined to be only 9.5 seconds, which was too fast for known asteroids. Obtained range-Doppler radar images confirm that the object has an elongated shape with a length of about 10 meters and a width of about 3 meters, which corresponds to the size of Centaur upper-stage rocket booster. Obtained circular polarization ratio of ~0.31 can be explained by the presence of surface irregularities at centimeter scales. The radar albedo of 95 % confirms that the surface of 2020 SO has a high reflectivity in the radio range, typical of metals. Our results are consistent with observational data obtained in other ranges of the spectrum. We have demonstrated the ability of radar astronomy to distinguish between natural and artificial near-Earth objects.

2020 SO was finally removed from the Minor Planet Center database on 19 February 2021 due to its artificial origin [11].

ACKNOWLEDGEMENTS

We would like to thank Lance A. M. Benner and the technical staff at Goldstone and Svetloe for the help with the radar observations.

REFERENCES

1. MPEC 2020-S78: 2020 SO. (2020). *Minor Planet Electronic Circular*. Available at https://www.minorplanetcenter.net/mpec/K20/K20S78.html
2. JPL News. (2020). *Earth May Have Captured a 1960s-Era Rocket Booster*. Available at https://www.jpl.nasa.gov/news/earth-may-have-captured-a-1960s-era-rocket-booster
3. Jorgensen, K., Rivkin, A., Binzel, R., Whitely, R., Hergenrother, C., Chodas, P., … & Vilas, F. (2003). Observations of J002E3: Possible Discovery of an Apollo Rocket Body. *Bulletin of the American Astronomical Society*, *35*, 981.
4. MPEC 2007-V69: 2007 VN84. (2007). *Minor Planet Electronic Circular*. Available at https://www.minorplanetcenter.net/mpec/K07/K07V69.html
5. Miles, R. (2011). The Unusual Case of 'Asteroid' 2010 KQ: A Newly Discovered Artificial Object Orbiting the Sun. *Journal of the British Astronomical Association*, *121* (6), 350–354.
6. MPEC 2018-A63: 2018 AV2. (2018). *Minor Planet Electronic Circular*. Available at https://www.minorplanetcenter.net/mpec/K18/K18A63.html
7. Ostro, S.J. (1993). Planetary Radar Astronomy. *Reviews of Modern Physics*, *65*, 1235–1279.
8. Virtual Telescope Project. (2020). *Near-Earth Object 2020 SO: Rotation and Time-Lapse*. Available at https://www.virtualtelescope.eu/2020/12/02/near-earth-object-2020-so-rotation-and-time-lapse-01-dec-2020
9. Great Shefford Observatory. (2020). *Phased Plot: 2020 SO*. Available at https://birtwhistle.org.uk/images/2020_SO_20201201.06_PBirtwhistle.png
10. Reddy, V., Battle, A., Campbell, T., Chodas, P., Conrad, A., Engelhart, D., … Wainscoat, R. (2021). Challenges in Differentiating NEOs and Rocket Bodies: 2020 SO Study. In: *IAA Planetary Defense Conf.*, 26–30 April 2021, Vienna, Austria.
11. MPEC 2021-D62. (2021). *Minor Planet Electronic Circular*. Available at https://www.minorplanetcenter.net/mpec/K21/K21D62.html

LATVIAN JOURNAL OF PHYSICS
AND TECHNICAL SCIENCES
2022, N 3

DOI: 10.2478/lpts-2022-0022

IMPORTANCE OF SPECTRUM MANAGEMENT IN RADIO ASTRONOMY

J. Kallunki*[1], V. Bezrukovs[2], W. Madkour[3,4], P. Kirves[1]

[1] Aalto University, Metsähovi Radio Observatory,
Metsähovintie 114, 02540 Kirkkonummi, FINLAND
[2] Engineering Research Institute
“Ventspils International Radio Astronomy Centre”,
101 Inzenieru Str., Ventspils, LV-3601, LATVIA
[3] Committee on Radio Astronomy Frequencies (CRAF),
European Science Foundation
[4] Institute for VLBI ERIC (JIVE),
Oude Hoogeveensedijk 4, 7991 PD Dwingeloo, the NETHERLANDS
*e-mail: juha.kallunki@aalto.fi

The increasing terrestrial and space-borne communications are causing major problems to the radio astronomy observations. Only a minor part of the frequencies is allocated to the passive services, such as Radio Astronomy Services (RAS). There are only a few, relatively narrow frequency bands below 20 GHz, which are still suitable for the radio astronomical observations. In addition, Out-of-Band (OoB) emissions will be a real threat to the observations on these bands. On behalf of all European radio astronomers, the Committee on Radio Astronomy Frequencies (CRAF) of the European Science Foundation (ESF) coordinates activities to keep the frequency bands used by radio astronomy and space sciences free of interference. Along with interference caused by active radio communication services, the local electronic device selection should be considered in the observatories. For instance, more common LED based lamps could cause harmful interference for the observations. Thus, it is very important to perform continuous radio frequency interference (RFI) monitoring locally, in each radio observatory.

Keywords: *Frequency allocation, radio astronomy, radio frequency interference (RFI), spectrum management.*

1. INTRODUCTION

The radio astronomical observations play a key role when we are studying the universe. Quasars or active galactic nuclei (AGN), pulsar and Sun are few sources, which could be observed at radio frequencies. The radio domain between 10 MHz and 1000 GHz is the only domain in the electromagnetic spectrum, apart from the optical/infrared window, which can be observed in theory with ground-based telescopes [1], [2]. The observed radio astronomical signals are usually very weak, except signals from the Sun, for instance.

The radio frequencies are allocated between several services and users. Only a minor part of frequency bands is allocated to the passive service, especially to radio astronomy services (RAS). For this reason, it is very important to coordinate frequency activities with other frequency users and frequency administrations. On behalf of all European radio astronomers, the Committee on Radio Astronomy Frequencies (CRAF) of the European Science Foundation (ESF) performs such work. In addition, the radio observatories closely collaborate with their local frequency administrations on the issues related to frequency allocation. Apart from frequency allocation, usually radio observations have a protection zone around them at least for some frequencies or devices, e.g., ground radars. However, many European radio observatories are close to settlement. For this reason, a sufficiently large protective zone cannot be achieved. Radio observatories are usually quiet areas, where unnecessary radio transmitters should be switched off.

Some radio astronomical observations are made at bands without primary allocation to RAS. For instance, geodetic-VLBI (Very Long Baseline Interferometry) observations on S-band (2.21–2.35 GHz) are an example of such observations. Currently, in many locations S-band observations are not possible due to increasing RFI, but this must be accepted when operating on non-passive service bands. Also, low-frequency solar observations are mainly done at frequencies, which are not allocated to RAS. However, solar radio observations are not so sensitive to RFI. In general, frequencies below 15–20 GHz are full of various services, and these services pose also greater risk to RAS. At higher frequencies (> 30 GHz), there is still a limited number of various services, and radio astronomical observations are less vulnerable to interference.

One of the main threats to radio astronomy is Out-of-Band (OoB) emissions that are mainly caused by the harmonics of other active service bands. In addition, the adjacent interference from bands next to RAS band could cause interference. Figure 1 shows the sources of unwanted emission. Naturally, in-band emission is the most critical for the RAS. ITU-R (The International Telecommunication Union) Recommendation RA 796-2 (Protection criteria used for radio astronomical measurements) forms an overall framework for the protection of RAS. The recommendation, for instance, defines RFI power threshold levels, which are allowed for the radio astronomical observations in different modes. Besides the spectrum management, another important aspect is how different observatories respond to the interference issue. Daily decision making, for instance, regarding the selection of electronic components, plays a key role when addressing the interference issue in the individual observatory.

Relatively new and major potential threat to RAS is posed by new satellite services.

Hundreds of nanosatellites will be operating on NGSO (non-geostationary satellite orbit). In theory, satellite orbits could be calculated beforehand, and radio astronomical observation could avoid those tracks. However, an issue is getting difficult if there are hundreds of satellites in the sky [3].

Various interference mitigation techniques have been developed, starting from high-conductive front-end filters to the software processing, such as a waveform filtering [4].

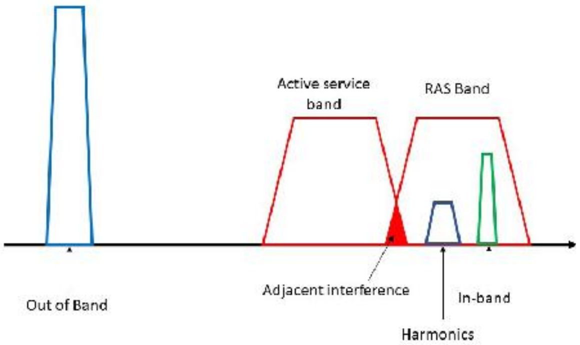

Fig. 1. Out-of-Band emission and adjacent interference to the radio astronomical services (RAS).

Figure 2 presents a scenario of the RFI emission entering the radio telescope. Interfering emission could enter the radio telescope either through direct or reflected paths – hitting the main beam or sidelobes.

When operating a large dish antenna and performing observations at high frequencies, the beam size is rather small. For instance, with a 14-metre dish and at the observing frequency of 37 GHz, the beam size is 2.4 arc min (40 millidegree). Also, the sidelobes of currently used radio telescopes are negligible small (ITU SA.509-2). This works as a good front-end filter. There are some technical solutions how to protect the signal chain from interference caused by observatories' own devices. Signal paths (cables) should be properly shielded, and the most sensitive equipment should be placed on the shielded racks or rooms. For instance, various data transmission should be implemented using the optical link, if possible. Many observatories are located in the seacoast, mountains, or valley. These natural geographical obstacles form a protective shield for radio observatories.

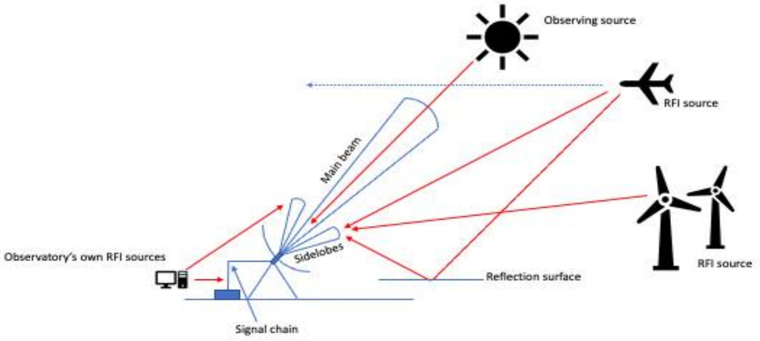

Fig. 2. Scenario of how the various RFI sources could enter radio astronomical observations through various paths.

Even if the other frequency services act as a major threat to RAS, in many cases a critical threat is posed by observatory-based sources of RFI. The high-end computing and high-speed electronics are most obvious sources of wide-band interfering emission. In addition, common LED based lamps and other household electronics could cause harmful interference. Currently, even domestic appliances are equipped with the radio transmitter, e.g., Bluetooth. It has been noticed that these interferences could be strong and occupy a very wide band.

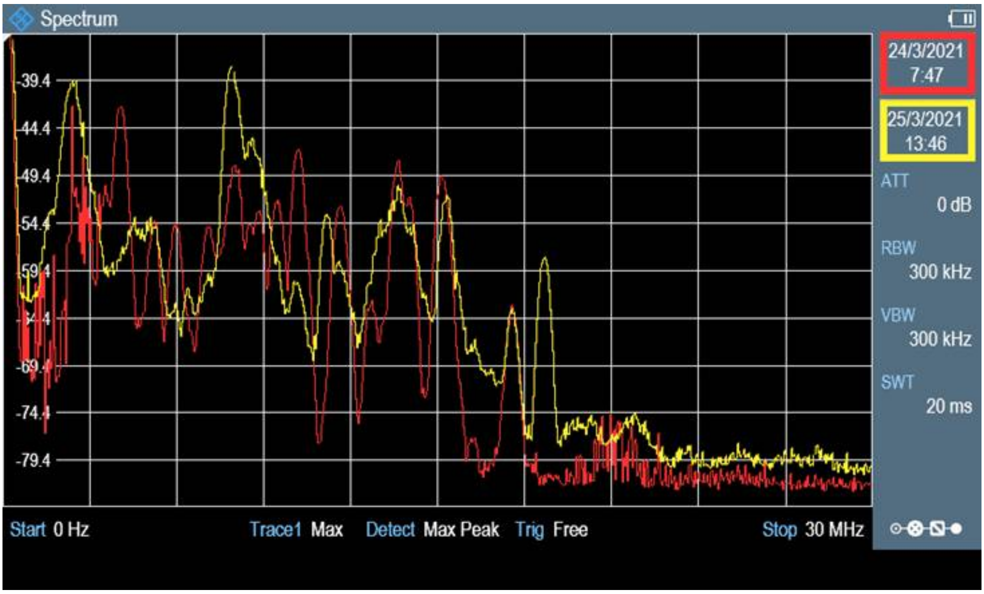

ATT 0 dB
RBW 300 kHz
VBW 300 kHz
SWT 20 ms
Start 0 Hz
Trace1 Max
Detect Max Peak
Trig Free
Stop 30 MHz

Fig. 3. HF spectrum on days when all electronic devices were switched off (red curve) and observatory was in normal mode (yellow curve). At lower frequencies, some intermodulation results are provided.

In March 2021, there was a long and planned power outage in Metsähovi Radio Observatory of Aalto University, Finland. On that day (24 March 2021), the HF (High Frequency) spectrum was measured when all observatory's electronic devices were switched off. The measurement was repeated on the following day (25 March 2021) when observatory was again fully operational. The measurement was carried with G5RV multiband wire HF antenna and R&S spectrum analyser (Spectrum Rider FPH) was used as a backend. Figure 2 demonstrates that the HF emissions and propagation conditions vary sometimes considerably and the observatory itself creates a lot of unwanted emissions, which increase, for instance, the noise floor level. This could be clearly seen at the frequency range between 20 and 30 MHz. To find out a more specific interference source, it requires performing detailed measurements by switching on observatory devices one by one. This takes times and, therefore, it is challenging to implement in practice.

3. PRACTICAL EXAMPLE OF RFI

Mainly, due to energy saving reasons, traditional bulb lamps were replaced with LED (light-emitting diode) based lightning solution in the past decade. In general, this change has been positive. However, this has brought new interference issues. The light consists of LED and LED driver. The LED driver is usually a reason for interference. It has been noted in practice that if the driver is not shielded properly, it causes interference. Also, if the earth conductor is not connected to the driver, it is a reason to suspect the interference properties of the light. Figure 3 shows HF spectrum of certain LED light. On the spectrum, it is possible to see a wide band peak at the centre frequency of 14.26 MHz (marker position in Fig. 3). The peak maximum intensity is more than 20 dB above the noise floor level.

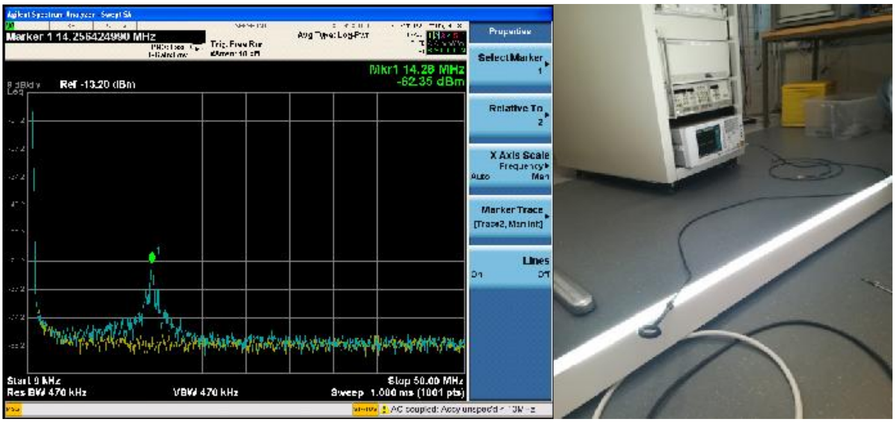

Marker 1 14.256424990 MHz

Trig: Free Run

Avg Type: Log-Pwr

Mkr1 14.28 MHz
-62.35 dBm

Ref -13.20 dBm

Start 9 kHz
Res BW 470 kHz

VBW 470 kHz

Stop 50.00 MHz
Sweep 1.000 ms (1001 pts)

Fig. 4. On the right, HF spectrum of certain LED light. In yellow, the noise floor level and in green, the spectrum when light was on. On the left, measuring setup is shown. A simple near-field probe was in use in this specific measurement.

The spectrum was measured with the near-field EMC (electromagnetic compatibility)-probe, and Agilent spectrum analyser (EXA – N9010A) was used as a backend.

4. RFI OBSERVATIONS

It is necessary to emphasise the importance of continuous RFI monitoring locally in each observatory. Each observatory should conduct radio environment observations regularly. The most usable interference monitoring system should cover observatory's whole observing bands. This usually means the bandwidth of several tens of gigahertz. Such systems are technically challenging and rather expensive. Also, the calibration of RFI measurements is challenging. Observations must be calibrated properly so that interference signal levels could be compared with the allowed interference power level or density. Measurement values, for instance, from the spectrum analyser are not sufficient. Other measurement setup parameters are needed. The power readings could be converted to flux units (S_{dB} in dBW/m^{2}Hz) using the following equation [5]:

$$S_{dB} = P_{SA_{dB}} - 10\log(B_S) - G_{R_{dB}} + k_{A_{dB}} - 35.77, \tag{1}$$

where P_{SAdb} is power in dBm read by a spectrum analyzer, B_s is a resolution bandwidth, G_{Rdb} is a receiver system gain and k_{Adb} is an antenna factor. The antenna factor could be defined as follows:

$$k_{A_{dB}} = 20\log(f) - G_{dBi} - 29.79, \tag{2}$$

where f is a frequency in MHz and G_{dBi} is an antenna gain.

In many cases, for instance, VLBI observations, observation data are post-processed in the correlator and observatories are not fully aware of RFI, which is possible in data. Thus, the dialogue among all operators is very important.

K-band (21.98–22.48 GHz) is an important radio astronomical observing band for EVN (European VLBI Network) community, since it is a frequency of water (H20) molecule line. Figure 5 shows frequency allocation on K-band in Finland. This is a typical situation in almost every radio astronomical observation on different observing bands.

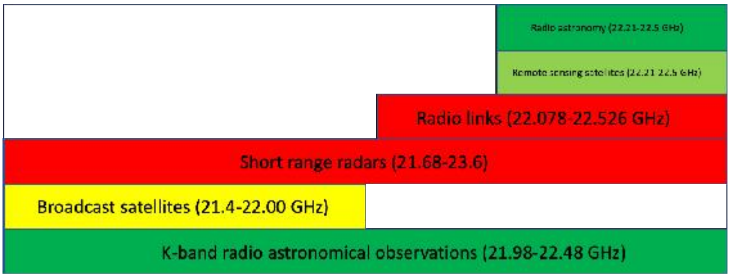

Fig. 5. Frequency allocation of 21.98–22.48 GHz in Finland.

In June 2021, preliminary interference measurements were made at K-band. Measurements were made with a 14-metre telescope by Metsähovi Radio Observatory of Aalto University and K-band VLBI receiver. As a back-end, a simple SDR-dongle (Nooelec NESDR Nano 3) was in use. SDRs had been earlier used successfully for interference monitoring, e.g., [6]. The scanning was made at four different azimuth directions (0°, 90°, 180°, 270°) and two different elevation angles (15°, 30°). Figure 6 illustrates interference observations.

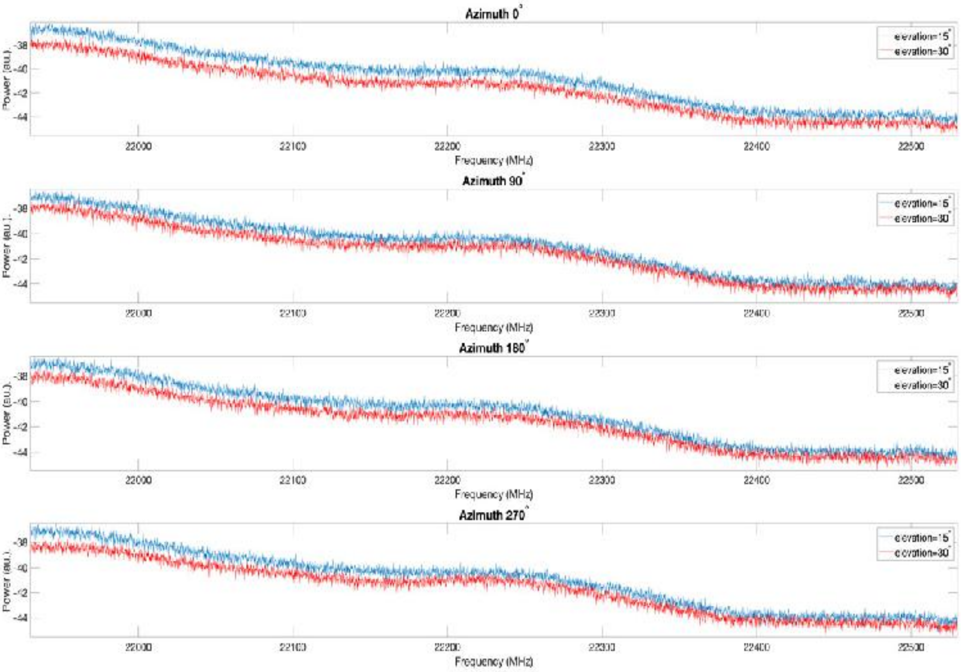

Fig. 6. Interference measurements at K-band on 7 June 2021.

It can be noticed that K-band is still very free of continuous interference and, thus, it is suitable for radio astronomical observations.

5. SPECTRUM MANAGEMENT

Spectrum management is the first line of defence against RFI, i.e., RFI is what happens when spectrum management fails. The radio spectrum is shared among several radio communication services. For the spectrum below 86 GHz, around 2 % is only allocated to a primary basis for the radio astronomy services. The situation improves for the higher frequencies where RAS allocations constitute around 15 % of the overall spectrum. Despite the fact that the radio astronomy observations go beyond these protected bands, it is important to preserve those bands as the clean islands of RFI in the radio spectrum. Also, those RFI-free bands play an important role in calibrations for the observations on the wider bands. For these reasons, it is very important to coordinate radio astronomical activities with other radio communication services to maintain the protected bands free of RFI.

On behalf of European radio astronomers, CRAF plays this coordination role. CRAF represents the European RAS at the International Telecommunications Union (ITU) level and at the regional level through the European Conference of Postal and Telecommunications Administrations (CEPT). CEPT covers 48 countries cooperating to regulate radio spectrum and communication networks. CRAF members also follow the radio regulation implementation at the national level, where every member state has the sovereign rights to apply its own regulations in accordance with the international regulations. CRAF is a Sector Member of the Radio Communication Sector of ITU and it has a formal observer status within the CEPT. Such a status enables CRAF to fully and independently contribute to the discussions at both levels, though it does not give voting privileges. That is why it is essential for CRAF to seek member states' support for its positions.

At present, CRAF has 26 members from 22 countries in Europe, in addition to South Africa. CRAF operates both at regulatory and technical levels. It also has an educational role in making other, particularly active radio spectrum users aware of the sensitivity and consequent need for the protection of radio astronomy frequencies. CRAF has developed its own tool for compatibility studies "PYCRAF" that has been widely used in defining the required protection for RAS, such as calculating the separation distances around radio telescopes and possible limits on power levels for emissions from active radio services.

6. CONCLUSIONS

The protection of radio frequencies is an important and critical task. It is a technical and administrative challenge at the same time. It needs continuous RFI measurements, simulations, and administrative work together with other frequency users and management bodies. Increasing activity, even higher frequency bands, will be a threat to the scientific community that uses radio frequencies. That is why all work done for protecting RAS is important. Also, the work done at observatories is critical. Self-made interference is a real threat to radio astronomical observations. Common electronic devices include radio transmitters (e.g., Bluetooth), which could be harmful for observations. Also, electronic devices are getting cheaper, and less attention is paid to EMC issues. An attitude towards RFI issues is still the most important aspect. This means, for instance, proper choice of components and devices at observatories. In addition, the other important aspect is related to the type of transmitters that are allowed in an observatory area. The interference issue is a large and complex area, which requires additional resources. Unfortunately, in most places, there are not enough resources to deal with this issue.

7. REFERENCES

1. van Driel, W. (2009). Radio quiet, please! - protecting radio astronomy from interference. *Instrumentation and Methods for Astrophysics*. doi.org/10.48550/arXiv.0906.2268.
2. CRAF. (2005). *Handbook for Radio Astronomy* (3rd ed.). Strasbourg: European Science Foundation. Available at https://craf.eu/wp-content/uploads/2015/02/CRAFhandbook3.pdf
3. UN Office for Outer Space Affairs. (2020). *Dark and Quiet Skies for Science and Society*. Available at https://www.unoosa.org/oosa/en/ourwork/psa/schedule/2020/2020_dark_skies.html
4. An, T., Chen, X., Mohan, P., & Lao, B. Q. (2017). Radio Frequency Interference Mitigation. *Acta Astronomica Sinica, 58* (5).

5. Hase, H., Gancio, G., Perilli, D., Larrarte, J. J., Guarrera, L., Garcia, L., … & Plötz, C. (2013). *Reports of the Finnish Geodetic Institute*. In 21st Meeting of the European VLBI Group for Geodesy and Astronomy (pp. 49–54), 5–8 March 2013, Espoo, Finland.
6. Kallunki, J., Bezrukov, D., Avotins, V., & Bleiders, M. (2019). Particularly Low-Cost Portable Radio Frequency Interference Monitoring System. *International Journal of Electromagnetic (IJEL), 2* (1), 1–7. Available at https://airccse.com/ijel/papers/2119ijel01.pdf

LATVIAN JOURNAL OF PHYSICS
AND TECHNICAL SCIENCES
2022, N 3

DOI: 10.2478/lpts-2022-0023

RELATIONSHIP BETWEEN SOLAR MILLIMETER AND SOFT X-RAY EMISSIONS

J. Kallunki*, M. Tornikoski

Aalto University, Metsähovi Radio Observatory, Finland,
Metsähovintie 114, Kylmälä, 02450, FINLAND
*e-mail: juha.kallunki@aalto.fi

The connection between solar radio and soft X-ray emission has earlier been studied at various radio frequencies. For instance, the intensity peak times during solar flares have been compared between these two wavelength regimes. It has been reported that solar radio emission peaks before soft X-ray emission during a flare. However, opposite results have also been presented. In this study, we compare millimetre (8 mm) solar and soft X-ray emissions (0.5–4 Å and 1–8 Å). The radio observations were made at Metsähovi Radio Observatory of Aalto University in Finland between 2015 and 2019. The soft X-ray data were observed with GOES-15 (Geostationary Operational Environmental Satellite). The data show that the solar millimetre emission can peak either before or after soft X-ray peak emission. In this study, we present two different scenarios, which could explain the peaking time differences and behaviour. The first scenario proposes a tight connection between the millimetre (8 mm) and soft X-ray emissions, the second one is for cases where the emission mechanisms are more separate.

Keywords: *Chromosphere, corona, instrumentation and data management, radio bursts, radio emission.*

1. INTRODUCTION

The connection between radio and X-ray emission during solar flares has earlier been studied on wide wavelength range, from metre (e.g., [1]) to millimetre (e.g., [2]) wavelengths. Millimetre-wavelength data has been used in studies, which have reported that the solar radio emission peaks before the soft X-ray emission during flares, e.g., [2], or the other way round, e.g., [3], [4]. In addition, it has been reported that the peak times also coincide, e.g., [4], [5]. The connection has also been studied statistically at frequencies below 17 GHz with Nobeyama Radio Polarimeter, NRP [6], compared against soft X-ray fluxes from the GOES (Geostationary Operational Environmental Satellites). 65 % of the flares with an impulsive component were found to have their impulsive radio emission reach a peak value ahead of the soft X-ray fluxes and this fraction was reported to increase with the radio frequency.

Soft-X-rays are usually produced by electrons with energies below 10 keV, and microwaves by electrons in the range of 100 keV–1 MeV, and more precisely, millimetre wavelength emission by electrons with energies of 0.5 MeV and even above [2]. The GOES soft X-ray data are most sensitive to plasma at a temperature of approximately 10 MK. The brightness temperature of the Quiet Sun Level (QSL) at 8 mm is 8100 K ± 300 K. It should also be noted that the radio emission is produced by electrons, whereas the soft X-ray emission has a large contribution from lines of highly-ionized atoms of elements heavier than hydrogen [7].

In addition, it has been reported that the soft X-ray data typically show only very smooth variations in time [8], whereas the millimetre emission in the impulsive phase does not correlate with the soft X-ray emission and thus is unlikely to contain any significant thermal bremsstrahlung component [9].

It this study, we investigate the connection between solar millimetre (8 mm) brightness intensity and soft X-ray intensities. In Section 2, we describe the instruments and in Section 3 – the observations. Results are presented in Section 4, and in Chapter 5, we propose a scenario for the formation of the solar millimetre and soft X-ray emissions. Using this scenario, we explain why in some cases the radio brightness peaks before the soft X-ray intensity peak and why in some other cases the other way round.

2. INSTRUMENTATION

Observations were carried out at Metsähovi Radio Observatory (MRO) of Aalto University in Finland (Helsinki region; GPS coordinates: N 60:13.04, E 24:23.35). The solar radio maps were observed at 8 mm with the MRO 14-meter radio telescope (RT-14). RT-14 is a radome-enclosed Cassegrain-type antenna with a diameter of 13.7 m. The usable wavelength range of the telescope is 13.0 cm–2.0 mm. During solar observing sessions, the antenna is used for solar mapping (Figs. 1 and 2, middle panels), partial mapping, and tracking of any selected areas on the solar disk. The observing frequency was 37 GHz, where the beam size of the telescope was

2.4 arc min marked as white circles in Figs. 1 and 2 (middle panels). The receiver is a Dicke-type radiometer with a Peltier element temperature stabilization and with a noise temperature of approximately 280 K. The temporal resolution during observations is 0.1 s or lower. The data are recorded in intensities. Solar radio maps can be observed in both linear and logarithmic scales and measured in both right ascension and declination directions. The logarithmic scale data are used only for strong solar radio brightenings. The time between two consecutive solar radio maps is around 140 seconds at fastest [10]–[12].

The soft X-ray data were received from GOES (Geostationary Operational Environmental Satellites) on two different channels: 0.5–4 Å (XS) and 1–8 Å (XL). The data were captured at 0.5 Hz sampling. The soft X-ray emission of solar flares comes mainly from the bright coronal loops at the highest temperatures normally achieved in the flare process. Used channels respond to temperatures above 4 MK. The soft X-ray emissions of solar flares come mainly from the coronal loops at the highest temperatures normally achieved in the flare process. GOES satellites have been measuring solar soft X-ray irradiance since 1975 with their X-ray sensor (XRS) [13].

3. OBSERVATIONS

The solar radio observations were made between June 2015 and May 2019, which included 35 millimetre flaring events in total. The solar radio brightness intensity profile was reconstructed on basis of consecutive solar radio intensity maps. The time gap between two consecutive solar radio maps is around 140 seconds at fastest. All individual maximum brightness intensity values were taken from the same radio brightening. In the upper plot of Fig. 1, we show the radio brightness intensity profile on 20 August 2015 and soft X-ray (for bands: 0.5–4 Å and 1–8 Å) profiles from the same day. In the middle plot, the radio brightness intensity map on 20 August 2015 is shown. The active region, NOAA 12403, which produced the solar flare, can be seen in the southern hemisphere. In addition, AIA 171 Å maps are shown in Fig. 1. In the lower panels, AIA 171 Å map during the X-ray peak time is shown (left) and AIA 171 Å map during the radio brightness intensity peak time is shown (right). In Fig. 2, similar information from the active region NOAA 12673 on 9 September 2017 is shown.

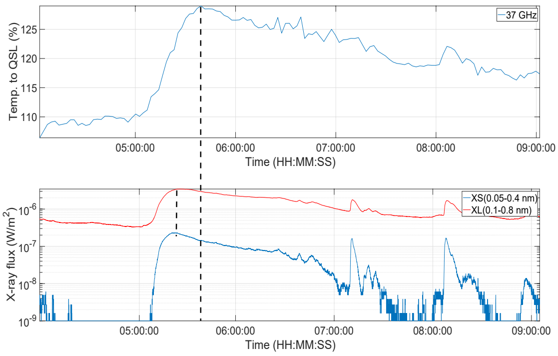

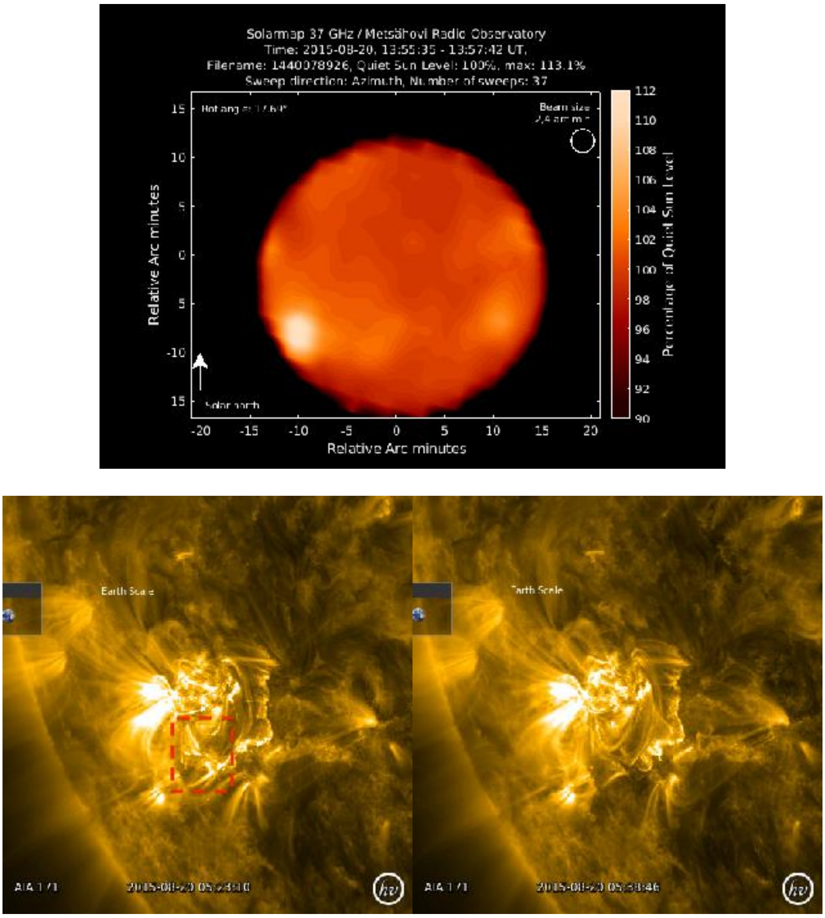

Fig. 1. In the upper panel, 8 mm radio brightness intensity profile and X-ray profiles (0.5–4 Å and 1–8 Å) on 20 August 2015. In the middle panel, 8 mm radio brightness intensity map from the same day. The radio brightness intensity peaked at 05:29 UT (longer dashed blue line). Shorter wavelength X-ray band (0.5–4 Å) peaked at 5:23 UT and longer X-ray band (1–8 Å) at 5:27 UT. In the lower panels, AIA 171 Å maps during the peak times (soft-X ray and radio brightening) are shown. The red box in the lower left panel shows the rapid energy release, which could indicate a magnetic reconnection.

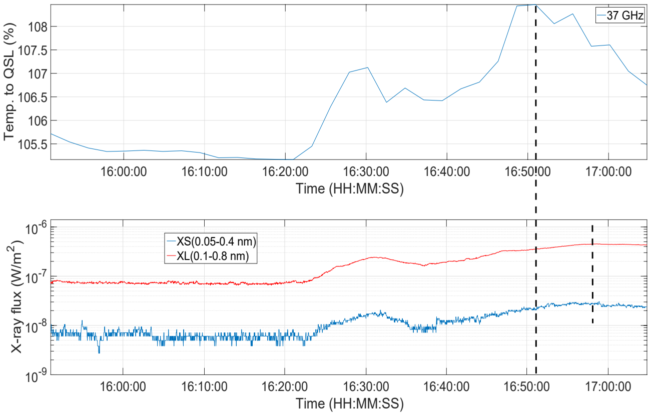

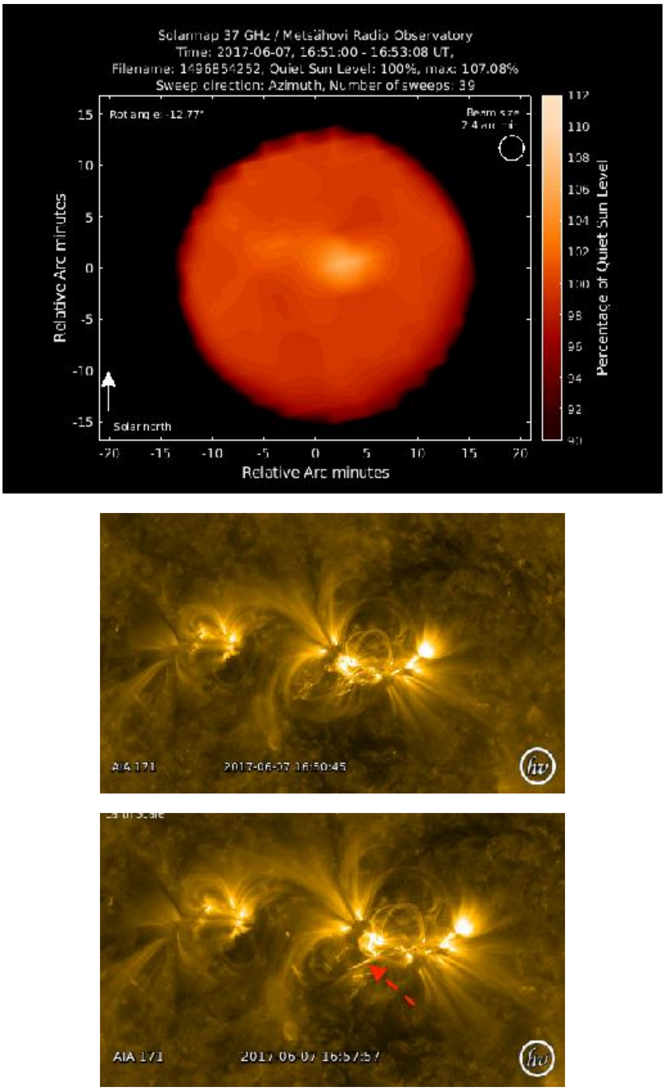

Fig. 2. In the upper panel, 8 mm radio brightness intensity profile and X-ray profiles (0.5–4 Å and 1–8 Å) on 7 June 2017. In the middle panel, 8 mm radio brightness intensity map from the same day. The radio brightness intensity peaked at 11:09 UT (longer dashed blue line). Shorter wavelength X-ray band (0.5–4 Å) peaked at 11:03 UT and longer X-ray band (1–8 Å) at 11:04 UT. In the lower panels, AIA 171 Å maps during the peak times (soft-X ray and radio brightening) are shown. The red arrow in lower panel shows the rapid energy release, which could indicate a magnetic reconnection.

The first event presented here (20 August 2015, Fig. 1) shows that radio intensity peaks after the soft X-ray peak intensity. The second example (7 June 2017, Fig. 2) is the opposite. Especially the second radio event is relatively strong, the maximum brightness intensity being around 180 % relative to the Quiet Sun Level (QSL). In the first event (Fig. 1), shorter wavelength (0.5-4 Å) X-ray peaked first. In the second example, both X-ray fluxes peaked simultaneously. For each observed radio event (35 in total), the peak time was defined. Similar analysis was also performed for both soft X-ray 0.5–4 Å and 1–8 Å fluxes. X-ray flux curves are formed on samples, which are taken at a sampling rate of 0.5 Hz. In Chapter 4, a comparison between the peak times is presented (Fig. 4).

4. RESULTS

We studied a connection between radio brightness and X-ray intensities. In addition, we investigated delays between radio brightening and X-ray flux peak occurring times. In Fig. 3, a correlation between 8 mm radio brightness and X-ray flux (1-8 Å) intensity maxima are shown. The R^2 coefficient is 0.67.

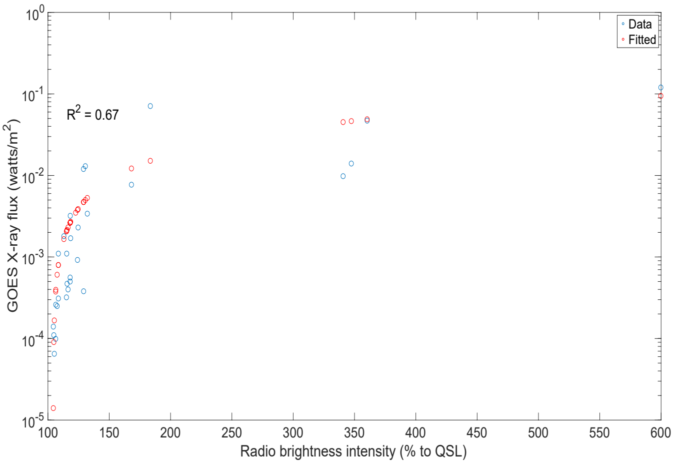

Fig. 3. Correlation between 8mm radio brightness and X-ray flux (1–8 Å) intensity maxima. The blue dots are real measurement results and red dots are fitted points (with a linear fitting). R-square (R^2) value of the fitting is 0.67.

Figure 4 shows delays between radio brightening and the X-ray flux peaking times. It can be noticed that radio brightness intensity can peak before or after the soft X-ray intensity peak. Furthermore, there is no connection or correlation between the radio brightness intensity and delays.

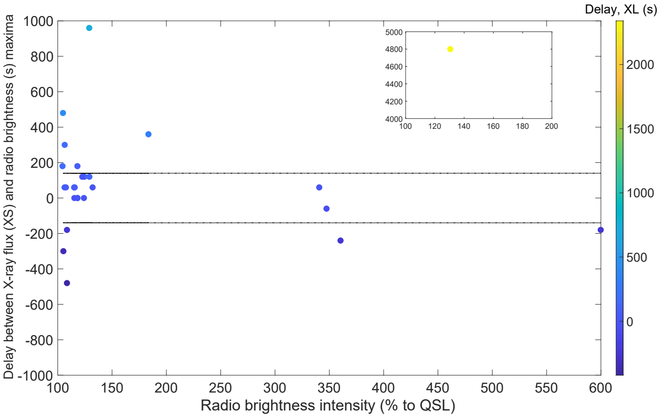

Fig. 4. Delays between radio brightening intensity peak time and soft X-ray peak times. Black lines indicate a possible error of radio brightness intensity peak time due to the fact that the time gap between two consecutive solar radio maps is around 140 seconds. The Y-axis indicates delays between XS (0.5–4 Å) soft X-ray band and radio brightening intensity peak times. The colour bar indicates delays between XL (1–8 Å) soft X-ray band and radio brightening intensity peak times. The outlier point of the data set is shown in the separate plot.

Figure 5 shows connection between soft X-ray 0.5–4 Å and 1–8 Å peak fluxes and radio brightness intensity peak delays. It can be noticed that delays are rather similar in both soft X-ray bands.

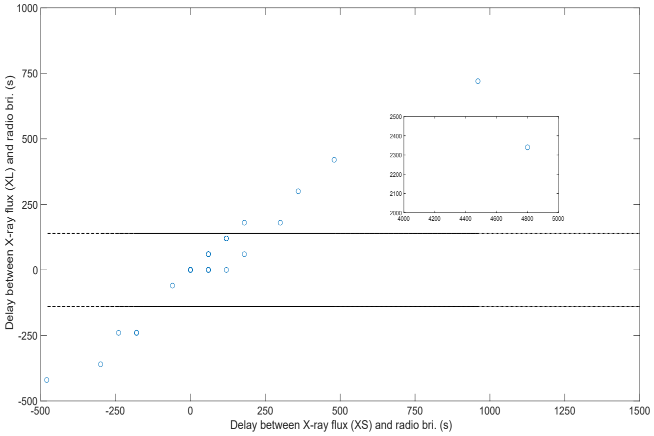

Fig. 5. Intensity peak time delays between soft X-ray bands (0.5–4 Å) and (1–8 Å). Black lines indicate a possible error of radio brightness intensity peak time due to the fact that the time gap between two consecutive solar radio maps is around 140 seconds. The outlier point of the data set is shown in the separate plot.

5. CONCLUSIONS AND FUTURE WORK

The emission at 8 mm originates from the upper chromosphere. Soft X-ray emission, instead, originates from the corona. Thus, it can be expected that millimetre emission should peak before the soft X-ray emission, if the accelerated electron is coming from the photosphere level. It has been shown that source of the strong soft X-rays is a location where the magnetic reconnection occurs [14]. The two examples presented here show that the soft X-ray emission peaked when the rapid energy release was detected in AIA 171 Å image.

In Fig. 6, we present a possible scenario for the solar flare formation from millimetre and soft X-ray emissions' perspective. The high energy particles are rising in the flaring loop from the photosphere to the higher atmospheric layers. These rising high energetic particles are seen as a solar flare at millimetre wavelengths. A source of strong soft X-ray intensity is located on top of the flaring loop when magnetic reconnection occurs. AIA 171 Å images support this interpretation because strong energy release happened on the time when soft X-ray intensity peaked. We can assume that it is a sign of the magnetic reconnection and it can appear either before or after radio intensity is peaking. Below are listed two scenarios which could explain the time differences between millimetre and soft X-ray emission intensity peaks.

- Scenario 1: Soft X-ray emission peaks before millimetre emission (or simultaneously) → Magnetic reconnection occurs on top of the flaring loop (source of strong soft X-ray emission) → High energy electrons are moving towards lower atmospheric layers → Millimetre emission is seen when electrons are crossing to chromosphere.

- Scenario 2: Soft X-ray emission peaks after millimetre emission → The high energy particles are rising in the flaring loop from the photosphere to the higher atmospheric layers → Millimetre emission is seen when they are crossing to chromosphere → Magnetic reconnection (soft-X-ray emission) occurs independently, and it does not cause downstreaming electrons which could be seen at the millimetre range.

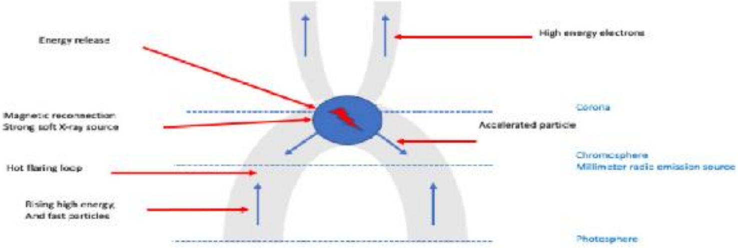

Fig. 6. A solar flare model according to CSHKP (Carmichael, Sturrock, Hirayama, Kopp and Pneuman) scenario and figure is adapted from [14].

This also means that it depends whether millimetre or X-ray emission peaks first. This can also be seen in Fig. 4. The radio millimetre brightness and soft X-ray intensities peak within 4–6 minutes on average (Fig. 4) and their peak intensities follow similar trends (Fig. 3). It has also been earlier reported that the soft X-ray source has starting heights of $0.6 \times R_{\odot}$ [15], which means coronal heights. However, because the intensities seem to correlate, it could mean that the emission mechanisms have something in common.

A majority of the radio brightening peak intensities in this study are relatively weak (<150 %). A more comprehensive analysis could be carried out with a larger number of flares and a wider range of intensities included in the study. We are continuously developing the MRO solar observing system, aiming at even higher cadence between solar radio maps and reducing the uncertainty of the peak time determination. With the new solar activity cycle now ongoing, we will be able to investigate the radio to X-ray connection at all solar activity phases.

REFERENCES

1. Ramesh, R., Kathiravan, C., Mithun, N.P.S., & Vadawale, S.V. (2021). Radio, X-Ray, and Extreme-ultraviolet Observations of Weak Energy Releases in the “Quiet” Sun. *The Astrophysical Journal, 918*, L18. doi:10.3847/2041-8213/ac1da3.
2. Kundu, M.R., White, S.M., Gopalswamy, N., & Lim, J. (1994). Millimeter, Microwave, Hard X-Ray, and Soft X-Ray Observations of Energetic Electron Populations in Solar Flares. *The Astrophysical Journal Supplement Series, 90*, 599. doi:10.1086/191881.
3. Pohjolainen, S., Hildebrandt, J., Karlický, M., Magun, A., & Chertok, I.M. (2002). Prolonged Millimeter-Wave Radio Emission from a Solar Flare near the Limb. *Astronomy and Astrophysics, 396*, 683–692. doi:10.1051/0004-6361:20021431.

4. Tsap, Y.T., Smirnova, V.V., Motorina, G.G., Morgachev, A.S., Kuznetsov, S.A., Nagnibeda, V.G., & Ryzhov, V.S. (2018). Millimeter and X-Ray Emission from the 5 July 2012 Solar Flare. *Solar Physics, 293*, 50. doi:10.1007/s11207-018-1269-6.
5. Valio, A., Kaufmann, P., Giménez de Castro, C.G., Raulin, J.-P., Fernandes, L.O.T., & Marun, A. (2013). POlarization Emission of Millimeter Activity at the Sun (POEMAS): New Circular Polarization Solar Telescopes at Two Millimeter Wavelength Ranges. *Solar Physics, 283*, 651–665. doi:10.1007/s11207-013-0237-4.
6. Wang, L., Liu, S.-M., & Ning, Z.-J. (2020). Statistical Properties of Radio Flux Densities of Solar Flares. *Research in Astronomy and Astrophysics, 20*, 178. doi:10.1088/1674-4527/20/11/178.
7. White, S.M., Benz, A.O., Christe, S., Fárník, F., Kundu, M.R., Mann, … & Warmuth., A. (2011). The Relationship Between Solar Radio and Hard X-ray Emission. *Space Science Reviews, 159*, 225. doi:10.1007/s11214-010-9708-1.
8. Kundu, M.R., White, S.M., Gopalswamy, N., & Lim, J. (1992). Millimeter and Hard X-ray/γ-ray Observations of Solar Flares during the June 91 GRO Campaign. *NASA Conference Publication 3137*, 502–513.
9. Lim, J., White, S.M., Kundu, M.R., & Gary, D.E. (1992). The High-Frequency Characteristics of Solar Radio Bursts. *Solar Physics, 140*, 343–368. doi:10.1007/BF00146317.
10. Kallunki, J., Tornikoski, M., Tammi, J., Kinnunen, E., Korhonen, K., Kesäläinen, S., & Arkko, O. (2018). Forty Years of Solar Radio Observations at Metsähovi Radio Observatory. *Astronomische Nachrichten, 339*, 204. doi:10.1002/asna.201813464.
11. Kallunki, J., & Tornikoski, M. (2018). Measurements of the Quiet-Sun Level Brightness Temperature at 8 mm. *Solar Physics, 293*, 156. doi:10.1007/s11207-018-1380-8.
12. Kallunki, J., Tornikoski, M., & Björklund, I. (2020). Identifying 8 mm Radio Brightenings During the Solar Activity Minimum. *Solar Physics, 295*, 105. doi:10.1007/s11207-020-01673-5.
13. Hanser, F.A., & Sellers, F.B. (1996). Design and Calibration of the GOES-8 Solar X-ray Sensor: The XRS. *GOES-8 and Beyond, 2812*, 344. doi:10.1117/12.254082.
14. Magara, T. A study of solar flares based on comparison between theory and observation, Department of Astronomy, Faculty of Science, Kyoto University, 1998, Ph.D. Thesis.
15. Reid, H.A.S., & Kontar, E.P. (2017). Imaging Spectroscopy of Type U and J Solar Radio Bursts with LOFAR. *Astronomy and Astrophysics, 606*, A141. doi:10.1051/0004-6361/201730701.

sciendo

LATVIAN JOURNAL OF PHYSICS
AND TECHNICAL SCIENCES
2022, N 3

DOI: 10.2478/lpts-2022-0024

MAGNETIC FLUX SWITCHING TYPE PERMANENT MAGNET GENERATOR FOR BICYCLES: MODELLING AND AN EXPERIMENTAL STUDY

V. Bezrukovs*, Vl. Bezrukovs, M. Konuhova,
D. Bezrukovs, A. Berzins, J. Trokss

Engineering Research Institute
"Ventspils International Radio Astronomy Centre",
Ventspils University of Applied Sciences,
101 Inzenieru Str., Ventspils, LV-3601, LATVIA
*e-mail: elmag@inbox.lv

The article introduces two new designs of flux switching permanent magnet alternators with a radial and an axial arrangement of the inductor relative to the magnetic flux switch. The study presents the results of 3D magnetic flux modelling along with the outcomes of physical experiments. In the course of laboratory experiments, the results of theoretical estimations are compared with actual physical performance parameters. The results are presented in the form of power and output voltage curves in relation to the frequency and load current. The study proposes the practical application of the alternators based on the magnetic flux switching principle in the development of a bicycle generator. Laboratory test models are made of a laminated steel using a waste-free technology.

Keywords: *Bicycles, magnetic fields, modelling, permanent magnet machines.*

1. INTRODUCTION

The current global trend towards the use of environmentally-friendly alternative energy sources for autonomous low-power loads re-ignited interest in machines capable of converting low-speed movement into electrical power.

Traditionally, for more than 100 years [1], [2], a permanent magnet synchronous machines, with 3.0 (W) power and output voltage 6.0 (V), attached to the bicycle frame near the wheel, were used as a power source for a lighting lamp to facilitate bicycle riding at night. The torque was transmitted from the tire tread on a bicycle wheel to the generator output shaft via a friction gear, which inevitably reduced the efficiency of energy conversion.

Over the past decades, the design of bicycle generators had been constantly improving and in the second half of the last century a number of companies began to develop generators with a fixed armature winding and permanent magnets, which were structurally connected to the bicycle wheel.

At the beginning of the 2000s, generators with claw-shaped poles, built into the hub of the front wheel, appeared on the market [3]–[5], making this type of devices widespread. At the same time, the generator placement inside of the wheel hub creates a number of problems for connecting the load to the armature winding terminals, which is closed by a rotating body inside of the hub.

More recently, new forms of the vernier hybrid permanent magnet machines [6], [7], which are based on the principle of variable-reluctance have come in sight. Along with simple design, these machines offer a compact direct drive solution for low-speed and low power applications.

A similar principle of variable reluctance is used in permanent magnet machines with magnetic flux switching. This type of machines has been first considered by Rauch and Johnson [8], and can be viewed as an evolution of an inductor generator. The study results of magnetic flux switching machines are presented in [9].

Flux switching machines have a number of properties that allow them to be used for converting mechanical energy into electrical energy in devices where the armature winding with a fixed permanent magnet can be located radially or axially relative to the movable magnetic flux switch [10]–[12]. In this case, a mechanical drive can perform rotational or cyclic movement relative to the stationary part and, in the view of the authors, could be used as an alternator for bicycles.

The authors of this study used the magnetic flux switching principle for the development of a new bicycle generator design. The proposed approach made it possible to combine in one device the supporting structures of the frame and bicycle wheels to create an inductor-type generator.

The use of a magnetic flux switching device as a generator made it possible to find solutions that provided certain advantages in comparison with placing the generator inside the wheel hub. In the process of the current research, related to the development of the magnetic flux switching type permanent magnet generator design for a bicycle, various options for placing an inductor with a fixed winding and a magnet relative to the rotor were considered. Specifically, models with a radial and an axial arrangement of a permanent magnet relative to the armature winding were considered.

2. BASIC RELATIONS

In the process of choosing the design of a brushless alternator, the design of which could be adapted for installation on a bicycle, a number of technical solutions were developed [13]–[17]. In order to study and evaluate the physical properties of the proposed machine design, a laboratory model was manufactured.

The calculation of the size of the magnetic circuit of the experimental model in the design process was performed using the basic relations adopted for the design of the inductor machine [18].

The toothed rotor in the considered device acts as a magnetic flux switch. In this case, the number of teeth Z on the rotor determines the frequency of flux pulsations in the magnetic core of the inductor.

The magnetic circuit was made in the form of two open magnetic cores (OMC) with teeth at the ends, which were shifted by a distance:

$$\tau_1 = \left(k + \frac{1}{2}\right) \cdot \tau_2 , \tag{1}$$

where k = 1, 2, 3 … the number of pairs of teeth for each OMC.

The teeth are separated from the rotor by an air gap – δ.

The teeth on the rods of the OMC, between which the magnet is located, are offset by

$$\tau_2 = 2 \cdot \tau . \tag{2}$$

In the considered device, the number pair of poles corresponds to the number of teeth on the movable part of the magnetic flux switch Z. The pole division τ in electrical degrees is linked to the rotor with the number of poles p by Eq. (3):

$$\tau = \frac{360°}{2 \cdot Z} . \tag{3}$$

When the rotor rotates, the fluctuation of the magnetic flux occurs in OMC with a flux switching frequency in the teeth and is determined according to Eq. (4):

$$f = \frac{n \cdot Z}{60} , \tag{4}$$

where n – the rotation speed, rpm^{-1}.

As a result of the magnetic flux magnitude fluctuations with a frequency f between the maximum Φ_{max} and minimum Φ_{min} values, an electromotive force (EMF) arises in the armature winding with the number of turns W, whose value is determined by Eq. (5) [18]:

$$E = 4{,}44 \cdot W \cdot f \cdot \frac{\left(\Phi_{\max} - \Phi_{\min}\right)}{2} . \tag{5}$$

3. MODELLING AND AN EXPERIMENTAL STUDY OF A GENERATOR WITH RADIAL INDUCTOR PLACEMENT

To assess the efficiency of the proposed magnetic flux switching generator, an experimental model of the magnetic core of the inductor was made of laminated steel with one magnet, two windings and a toothed rotor, the teeth of which are located along the entire circumference with a uniform pitch.

A fragment of an experimental sample of a generator with a radial arrangement of the inductor is shown in Fig. 1, which illustrates the location of an inductor with a magnet between two OMC made from laminated steel with two windings in relation to the toothed rotor.

Figure 2 shows the simulation of the magnetic field distribution in the OMC using ElCut software for physical field modelling for one of the possible positions of the teeth, where the paths of the closure of the flux with the maximum intensity are highlighted in yellow and those with the minimum intensity are highlighted in blue.

The main parameters of the model: dimensions of the magnet 19.5 mm x 12.7 mm x 6.35 mm; the number of turns of armature windings W = 2 x 110 turns; thickness of laminated steel package is 12.7 mm, the number of teeth on the rotor $Z = 40$.

The results of the laboratory trials of the experimental generator model are presented in Fig. 3 as output power P, (W) in relation to the frequency of voltage f, (Hz).

Fig. 1. An experimental model of a generator with a radial arrangement of the magnet and armature windings above the rotor teeth.

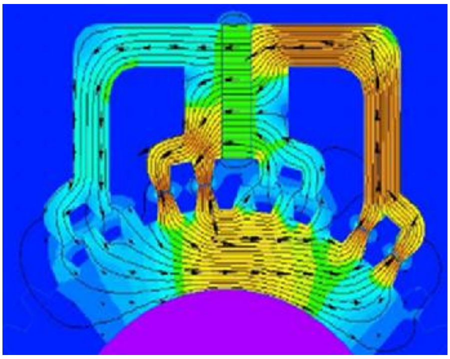

Fig. 2. Modelling of the distribution of magnetic flux in a magnetic core with a radial arrangement of the magnet and armature winding for one position of the teeth.

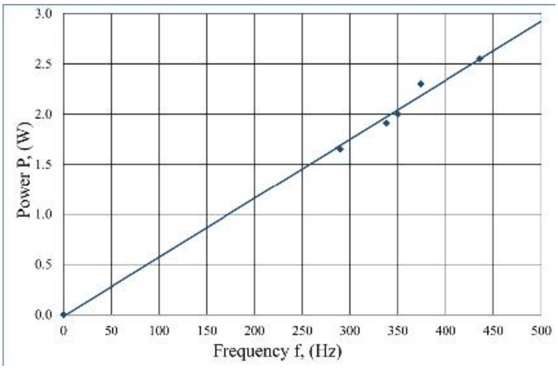

Fig. 3. Output power of the generator P, (W) against the frequency of voltage f, (Hz) for the light bulb load ($U = 6.3$ (V), $I = 0.34$ (A)).

An incandescent lamp with a rated voltage of $U = 6.3$ (V) and a current of $I = 0.34$ (A), which corresponds to a resistance of $R = 18.5$ (Ohm), was used as a load for the generator. The maximum power of the experimental model was $P = 2.56$ (W) at the voltage of $U = 7.12$ (V).

4. MODELLING AND AN EXPERIMENTAL STUDY OF A GENERATOR WITH AXIAL INDUCTOR PLACEMENT

With the axial arrangement of the permanent magnet inductor and OMC with armature windings, it is possible to develop a design, in which the OMC are located opposite of the teeth on the moving rotor, which act as a magnetic flux switch [19], [20]. In this case, the windings are located on both parts of the OMC, and the teeth only provide switching of the magnetic flux in the rods.

The layout of the windings W_1 and W_2 on the rods of the OMC and their position relative to the toggle switches Z fixed in the grooves on the magnetic flux switch are shown in Fig. 4.

The direction of the magnetic fluxes Φ_2, Φ_3, Φ_5, Φ_6 corresponds to the polarity of the N-S permanent magnets located on the outer rods of the OMC. The direction of the magnetic fluxes Φ_1, Φ_2, Φ_3 for one permanent magnet is presented in Fig. 5. The values of magnetic fluxes from permanent magnets Φ_1, Φ_4 through commutation during the movement of the rotor do not change and are equal to:

$$\Phi_1 = \Phi_2 + \Phi_3, \tag{6}$$

$$\Phi_4 = \Phi_5 + \Phi_6. \tag{7}$$

The magnetic flux switch is made of a non-magnetic material, for example, of plastic in the form of a tape, which can be made as a linear rotor or shaped as a ring and placed on the edge of a disc. In this case, the design of the device would not have axial symmetry.

The analysis of the density distribution of magnetic fluxes in OMC was carried out by 3D modelling of the magnetic field using EMWorks software.

In the generator model under investigation, the number of pairs of teeth for each of the OMC equals $k = 2$. In this device, the axial arrangement of the inductor made of laminated steel relative to the toggle switches is used. The toggle switches placed around the circumference and permanent magnets are located on the external rods of OMC and are connected by bridges.

The 3D model of a generator with the representation of the magnetic field density distribution in the rods of OMC is shown in Fig. 6, where the given palette of intensity (T) makes it possible to estimate the degree of saturation of magnetic circuit sections.

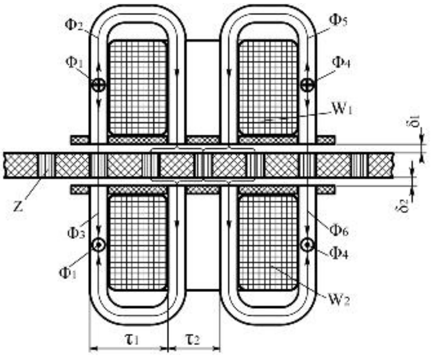

Fig. 4. Diagram of the axially arranged OMC with windings relative to the direction of the rotor rotation and the direction of magnetic fluxes.

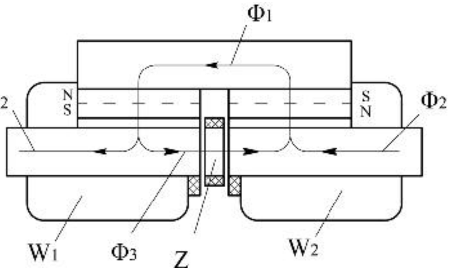

Fig. 5. Diagram of the direction of magnetic fluxes created with permanent magnets in OMC, located opposite of the toggle switches fixed in the grooves of the plastic strip of the magnetic flux switch.

Figure 7 shows the 3D model of the magnetic field intensity (T) in the air gap when the maximum of magnetic flux

$$\Phi_{\max} = \Phi_2 + \Phi_5 \tag{8}$$

is closed through the toggle switches located opposite of the four middle rods 3, 4, 5, 6 covered by the coil. In this position, the minimum of magnetic flux

$$\Phi_{\min} = \Phi_3 + \Phi_6, \tag{9}$$

is closed through the rods 1, 2, 7, 8 where permanent magnets are placed.

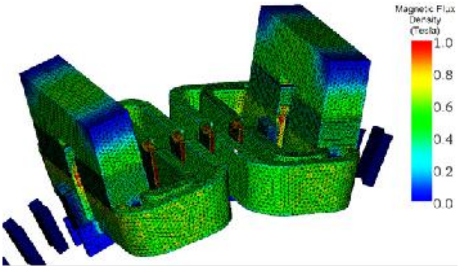

Fig. 6. Design of the investigated model with the representation of the magnetic field density distribution in the rods of OMC and the palette of its intensity (T).

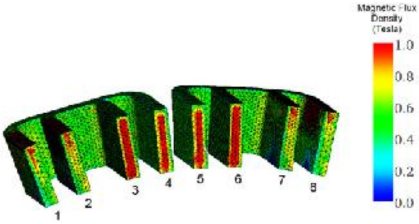

Fig. 7. The 3D model of the distribution of the magnetic field in the rods of OMC at the boundary with the air gap and the palette of its intensity (T).

Figure 8 shows theoretical estimates of the distribution of the magnetic field in OMC for rotating of rotor at angle τ_2. A step of displacement of the toggle switches of the magnetic flux switch equals 0.2 degrees and makes it possible to calculate the magnetic flux magnitude changes in the outer 1, 2, 7, 8 and in the inner 3, 4, 5, 6 teeth shown in Fig. 7.

The test samples of OMC are made of laminated steel type 23ZH90 with a thickness of 0.23 mm using waste-free technology for manufacturing cores by winding. The dimensions of the model are designed for mounting it on a bicycle frame using a steel or plastic disc as a rotor connected to the wheel with an outer diameter of 140 mm and a thickness of 2 mm.

Figure 9 shows one section of OMC with two pairs of teeth and the outer core size of 2.07 mm × 22.9 mm × 18.0 mm × 9.7 mm and the inner one of 2.07 mm × 12.7 mm × 16.0 mm × 9.7 mm.

The dimensions of the four NdFeB (N48) magnets are 8 mm × 15 mm × 4.5 mm.

The coil body in Fig. 10 with overall dimensions of 70 x 43 x 35 mm for an armature winding and one pair of OMC is made using a 3D printing technology. A strip for a movable magnetic flux switch, shown in Fig.11, is made using the same technology. This allows positioning the ends of the rods with high accuracy in relation to the toggle switches located in the grooves of the plastic strip of the magnetic flux switch 15 mm wide and 4.0 mm thick.

The winding of the experimental model consists of two coils with a wire of 0.41 mm in diameter and with the number of $W = W_1 + W_2 = 215 + 215 = 430$ turns. Winding resistance $R_w = 2.6 + 2.6 = 5.2$ (Ohm), inductance $L_w = 34.1$ (mH).

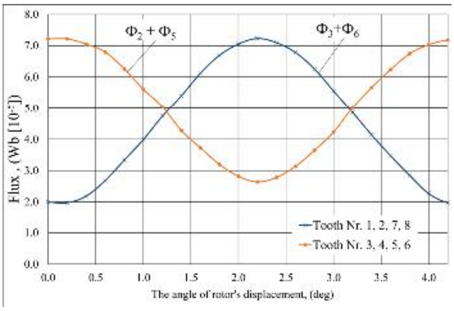

Fig. 8. Magnetic flux changes in the air gap of the generator in the outer 1, 2, 7, 8 and in the inner 3, 4, 5, 6 teeth of the OMC rods for the angle of rotor displacement τ_2.

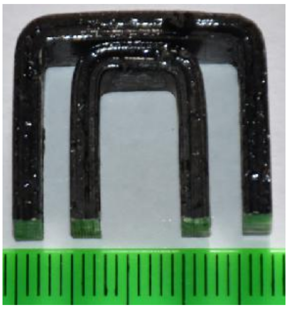

Fig. 9. One section of OMC with two pairs of teeth from laminated steel, size scale in mm.

The arrangement of the generator model on a bicycle frame is also shown in Fig. 11, where the inductor is fixed on the seat of the disc brake mechanism, and the plastic strip of the magnetic flux switch with the number of toggle switches equal to $Z = p = 86$ is made in the form of a ring and is fixed on the steel disc.

The values of magnetic fluxes in the teeth of OMC for two positions of the magnetic flux switch are given in Table 1. In the first position, the toggle switches are located opposite the teeth 3, 4, 5, 6 that corresponds to the maximum value of the magnetic flux $\Phi_{\max}$. In the second position, the toggle switches have a displacement of $\frac{1}{2}\tau_2$ that corresponds to the minimum value of the magnetic flux $\Phi_{\min}$.

In the considered design, the magnetic flux tied with the windings W_1, W_2 is equal to the sum of the fluxes presented in Table 1. The results of the magnetic flux values obtained for the corresponding type of magnets and the size of the OMC allow estimating the value of *EMF* in the windings, which occurs as a result of this flux variations.

Table 1. Values of the Maximum Φ_{max} and Minimum Φ_{min} Magnetic Fluxes in the Teeth of OMC with the Toggle Switch Displacement of $\frac{1}{2}\tau_2$

Tooth number	Magnetic flux	
	Maximum flux (Φ_{max})	Minimum flux (Φ_{min})
3	$1.88\ 10^{-5}$	$6.63\ 10^{-6}$
4	$1.74\ 10^{-5}$	$6.82\ 10^{-6}$
5	$1.74\ 10^{-5}$	$6.52\ 10^{-6}$
6	$1.88\ 10^{-5}$	$6.54\ 10^{-6}$
Total	$\mathbf{7.24\ 10^{-5}}$	$\mathbf{2.65\ 10^{-5}}$

The EMF value for a test model with the number of turns of armature winding $W = 430$ at a frequency of flux fluctuation $f = 300$ (Hz) and the size of the air gaps

$$\delta_1 = \delta_2 = 0.2\,\text{mm} \tag{10}$$

can be calculated using Eq. (5):

$$E = 4{,}44 \cdot 430 \cdot 300 \cdot \frac{(7.24 - 2.65) \cdot 10^{-5}}{2} = 13.14\ \text{(V)}. \tag{11}$$

The results of these calculations show that the chosen dimensions of the magnetic circuit and magnets are sufficient to induce the specified EMF value by switching the magnetic flux in the windings of the generator.

The test sample allows determining the actual technical characteristics of the generator with an axial arrangement of the inductor and estimating the potential for its use as a power supply source for bicycle electronics devices. Thus, the simulation results can serve as a reliable basis for designing a generator with specified characteristics.

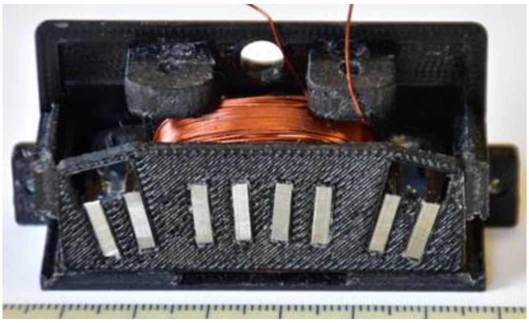

Fig. 10. Coil body with OMC with two pairs of teeth made of laminated steel with armature winding and dimensions size in mm.

Fig. 11. Placement of the axial generator inductor on the bike frame and the plastic strip of the magnetic flux switch with toggle switches on the steel disc.

The results of the experimental model testing are presented in the diagrams in the form of approximated curves in Figs. 12 and 13, displaying the output voltage U, (V) depending on the load current I, (A) and power P, (W) at different frequency of voltage f, (Hz).

An oscillogram of a sinusoidal alternating voltage across the armature winding of an inductor without load for one of the stages of the experimental study is shown in Fig. 14. The curve of the output voltage U, (V) without load depending on the frequency of voltage f, (Hz) is presented in Fig. 15.

As can be seen from the analysis of the curves obtained as a result of the experiment, the maximum generator power significantly increases with increasing frequency.

The experimental results are in close alignment with the numerical solutions obtained during the simulation. The value of the EMF estimated for frequency $f = 300$ Hz using Eq. (11) equals $E = 13.14$ V, while the value of output voltage without load at this frequency, obtained from the experimental model, shown in Fig. 12 is equal to $U = 12.0$ V. Thus, experimental and simulation results differ by less than 10 %. The deviation can be attributed to the uncertainty with the parameter values of the permanent magnets and to difficulties with ensuring a stable air gap of 0.2 mm in the experimental setting. In further studies, the characteristics of the magnets and the width of the air gap could be considered with better accuracy.

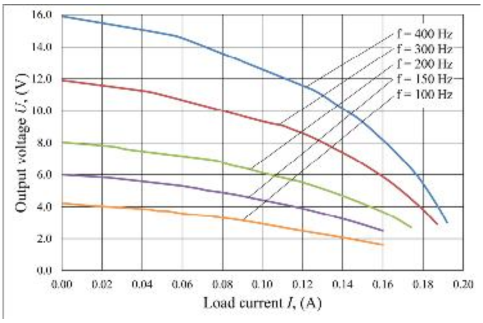

Fig. 12. The output voltage curves U, (V) against the load current I, (A) at different frequency of voltage f, (Hz).

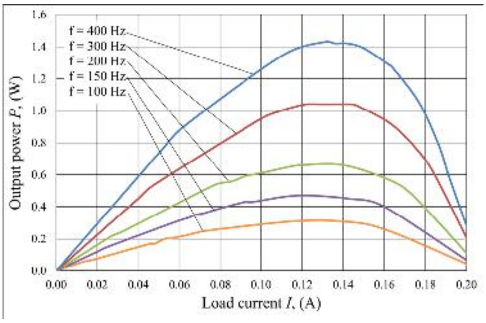

Fig. 13. The power curves P, (W) against the load current I, (A) at different frequency of voltage f, (Hz).

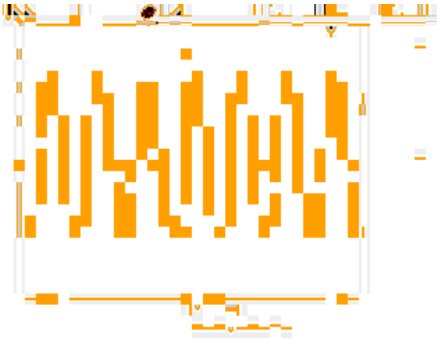

Fig. 14. Oscillogram of the voltage waveform on the armature winding of the generator without load for one of the stages of the experimental study.

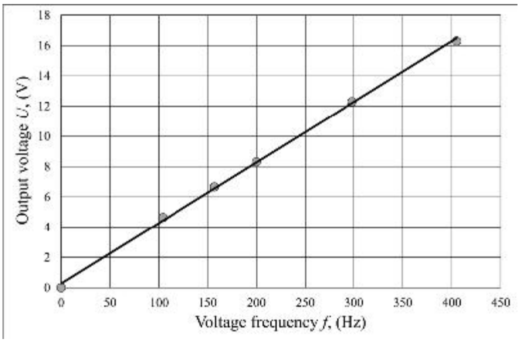

Fig. 15. The output voltage curves U, (V) at the armature winding of the generator without load versus the frequency of voltage f, (Hz).

5. DISCUSSION

In the course of the study, an original design of a permanent magnet generator with magnetic flux switching and an axial arrangement of the inductor has been developed and tested. The results of the study show that the proposed technical solution has good prospects to be used as a power source for charging bicycle electronic devices.

Furthermore, it has been shown that such generators can be manufactured using a waste-free technology for strip of OMC. This technology significantly reduces the production costs of OMC.

The considered generator is characterized by its integration with the bicycle design, where the inductor with permanent magnets and windings is attached to the bicycle frame, and the non-magnetic strip with the toggle switches is placed on the plastic or steel disk connected to the wheel.

Modelling the distribution of magnetic fluxes in the magnetic cores of the inductor, the results of experimental studies and analysis of the created device show that the power of generator can be varied by changing its dimensions and the number of switches on the rotor. This allows the alternator to be adapted to the load requirements – power banks and bicycle electronics.

ACKNOWLEDGEMENTS

The research has been supported by the European Regional Development Fund within the project “Environmentally Friendly Small Power Generator with the Rotor Linear Motion (DrauGen)” No. 1.1.1.1/18/A/125.

REFERENCES

1. Patent 1893: Generator for bicycle, GB 9662.
2. Chefford Master MFG Co Inc. (1948). *Patent US 2453523A 1948: Bicycle Generator Regulated by Rotor Torque Variations*. USA.

3. Wilfried, S. (1994). *Hub Generator, Especially for Bicycles*. Patent EP0591724A1.
4. Bridgestone Cycle Co. (1995). *Hub Generator for Bicycle*. Patent JPH0710057A.
5. Shimano KK. (2003). *Claw-Pole Generator and Hub Dynamo for Bicycle*. Patent JP2003333777A.
6. Spooner, E., Tavner, P., Mueller, M.A., Brooking, P.R.M., & Baker, N.J. (2004). Vernier Hybrid Machines for Compact Drive Applications. In: *Second International Conference on Power Electronics, Machines and Drives (PEMD 2004)*, (pp. 452–457), 31 March–2 April 2004, Edinburgh, UK.
7. Raihan, M.A.H., Baker, N.J., Smith, K.J, & Almoraya A.A. (2018). Development of Low Translator Mass Linear Vernier Machine for Wave Energy Power Take Off. In: *The 7th International Conference on Renewable Power Generation*, (pp. 1–5), 26–27 September 2018, DTU, Lyngby, Copenhagen, Denmark.
8. Rauch, S.R., & Johnson, L.J. (1955). Design Principles of Flux Switch Alternators. *IEE Trans Power Apparatus and Systems, Part III, 74* (3), 1261–1268..
9. Kwon, J.W., Lee, J.H., Zhao, W., & Kwon, B.I. (2018). Flux-Switching Permanent Magnet Machine with Phase-Group Concentrated-Coil Windings and Cogging Torque Reduction Technique. *Energies*, *11* (2758), 1–11.
10. Diab, H., Amara, Y., & Barakat, G. (2020). Open Circuit Performance of Axial Air Gap Flux Switching Permanent Magnet Synchronous Machine for Wind Energy Conversion: Modeling and Experimental Study. Energies, MDPI. Open Access Journal, 13 (4), 1–19.
11. Zhu, Z.Q., & Chen, J.T. (2010). Advanced Flux-Switching Permanent Magnet Brushless Machines. *IEEETrans. Magn., 46*, 1447–1453.
12. Andrada, P., & Martínez, F. (2016). Flux Switching Alternators for Small Wind Generation. *Renew. Energy Power Qual. J., 1*, 67–68.
13. Bezrukovs, V., & Levins, N. (2008). *Generator for Bicycle*. Patent LV13750.
14. Bezrukovs, V., & Levins, N. (2009). *Bicycle Generator*. Patent WO2009084938.
15. Bezrukovs, D., Bezrukovs, V., Bezrukovs, Vl., & Levins, N. (2011). *Contactless Generator for Bicycle.* Patent LV 14377.
16. Bezrukovs, D., Bezrukovs, V., Bezrukovs, Vl., & Levins, N. (2012). *Axial Inductor Generator for Bicycle*. Patent LV 14550.
17. Bezrukovs, D., Bezrukovs, V., Bezrukovs, Vl., & Levins, N. (2013). *Inductor Generator for Bicycle.* Patent LV 14695.
18. Dombur, L. (1984). *Axial Inductor Machines.* Riga: Zinatne, 247.
19. Bezrukovs V., Bezrukovs Vl., Bezrukovs D., Konuhova M., Berzins A. (2020): *Magnetic flux switching type permanent magnet generator.* LV15501, 20.12.2020.
20. Bezrukovs V., Bezrukovs Vl., Bezrukovs D., Konuhova M., Berzins A. (2022): *Magnetic flux switching type permanent magnet generator*. EP3955439A1·2022-02-16.

LATVIAN JOURNAL OF PHYSICS
AND TECHNICAL SCIENCES
2022, N 3

DOI: 10.2478/lpts-2022-0025

AXIAL FLUX SWITCHING PERMANENT MAGNET ALTERNATOR WITH EXTERNAL MAGNETIC CORES

V. Bezrukovs, Vl. Bezrukovs*, M. Konuhova, D. Bezrukovs, A. Berzins

Engineering Research Institute
"Ventspils International Radio Astronomy Centre"
Ventspils University of Applied Sciences,
101 Inzenieru Str., Ventspils, LV-3601, LATVIA
*e-mail: vladislavsb@venta.lv

The article introduces the results of studying the magnetic field distribution in the alternator inductor with an axial arrangement of open magnetic cores (OMC) and external closure of magnetic fluxes. The study compares the efficiency of using magnetic fluxes from permanent magnets (PM) on the example of two model variants of inductors with OMC developed by the authors. The analysis of the density distribution of magnetic fluxes in OMC was carried out by 3D modelling of the magnetic field using EMWorks software. It has been shown that such generators can be manufactured using a waste-free technology for strip of OMC. This technology significantly reduces the production costs of OMC. By modelling the distribution of magnetic fluxes in the OMC of the inductor, the results of experimental studies and analysis of the created device show that the capacity of generator can be varied by changing its dimensions and the number of the toggle switches on the rotor. This allows the alternator to be adapted to the load requirements – power banks and bicycle electronics.

Keywords: *Bicycles, magnetic fields, modelling, permanent magnet machines.*

1. INTRODUCTION

Current global trend towards the use of environmentally-friendly alternative energy sources for autonomous low-power loads re-ignited interest in machines capable of converting low-speed movement into electrical power. Axial flux switched reluctance machines exhibit unique characteristics that specify their superiority over other topologies in specific applications. A number of researchers have studied the efficient design and constructed structures in different types of these machines [1], [2].

More recently, new forms of the vernier hybrid permanent-magnet machines [3], [4], which are based on the principle of variable-reluctance have come in sight. Along with simple design, these machines offer a compact direct drive solution for low-speed and low-power applications.

A similar principle of variable reluctance is used in PM machines with magnetic flux switching. This type of machines has been first considered by Rauch and Johnson [5], and can be viewed as an evolution of an inductor generator. The articles [6]–[9] present the results of studies of magnetic flux switching machines by a number of authors.

The authors of this study used the magnetic flux switching principle for the development of a new bicycle generator design. The proposed approach made it possible to combine in one device the supporting structures of the frame and bicycle wheels to create an inductor-type generator [10]–[12].

The use of a magnetic flux switching device as a generator has made it possible to find solutions that provide certain advantages in comparison with placing the generator inside the wheel hub. In the process of the current research, related to the development of the magnetic flux switching type PM generator design for a bicycle, various options for placing an inductor with a fixed winding and a magnet relative to the rotor have been considered.

The characteristic feature of alternative energy sources is the uneven movement of mechanical energy, which can be converted into electrical energy. In this regard, to increase the efficiency of electric machines, gearbox is used, which adapts the performance of alternators and drive mechanisms. However, in most cases, the most effective appliances are the ones that do not contain the gearboxes. This becomes possible with the use of special types of direct drive electric machines, the designs of which allow for adjustment to the actuating mechanism.

The authors of the article propose a new design of an electric machine as an autonomous power source for bicycle electronics devices. In the process of searching for the necessary design solutions and the possibility of their optimization, several versions of alternators of a new type with certain technical characteristics have been developed.

The constructional characteristics of machines of this type make it possible to manufacture the movable part of the magnetic flux switch in the form of a strip connected to the drive. In this case, a strip made of non-magnetic material can perform cyclic reciprocating movements or be placed on the circumference of a disk that is connected to a rotating shaft.

In the considered case, the actuating mechanism is a bicycle wheel, from which the strip of magnetic flux switch is driven. In the process of choosing the design of a brushless alternator, the design of which could be adapted for installation on a bicycle, a number of technical solutions were developed [13]–[18].

2. THE ALTERNATORS WITH EXTERNAL MAGNETIC FLUX CLOSURE

a) Design of Model I

The design of the brushless energy converter shown in Fig. 1 contains a stationary magnetic core of an inductor with an armature winding and a PM, as well as a magnetic flux switch in the form of a strip, which makes a rotational movement. Since the axis of rotation of the actuating mechanism is located below the inductor, then to connect the strip to the actuating mechanism, the magnetic core of the inductor is made with external closure of the magnetic flux above the movable magnetic flux switch.

The magnetic circuit of the alternator inductor, proposed by the authors in the design [19], contains two groups of open magnetic circuits made of laminated silicone steel, on the rods of which armature windings are located. The external magnetic circuit of the inductor is made in the form of a magnetic bridge made of structural steel, which forms a magnetic circuit that connects the PM with OMC.

Fig. 2a shows the diagram of the arrangement of rods of OMC, where arrows denote the direction of magnetic fluxes in each of the rods. The main magnetic flux Φ from a PM passes through the magnetic bridge and is divided into fluxes in the rods of OMC, while the sum of the magnitude of these fluxes satisfies Eq. (1):

$$\Phi = \Phi_1 + \Phi_2 + \Phi_3 + \Phi_4. \tag{1}$$

The magnetic fluxes Φ_1, Φ_4 in the outer rods of OMC are not associated with the armature winding, at the same time the magnetic fluxes Φ_2, Φ_3 in the inner rods of OMC are connected with the armature winding. The magnitude of these fluxes is determined by the magnitude of the magnetic resistance of the corresponding sections of the air gap. Thus, the magnitude of these fluxes depends on the position of the magnetic toggle switches relative to the teeth at the ends of the rods of OMC.

The circuit for closing the main magnetic flux Φ and its fraction Φ_2 from a PM with poles N-S in the form of a contour line is shown in Fig. 3. The figure illustrates a section of an inductor with an armature winding, consisting of coils W_1, W_2 located on the rods of OMC, and magnetic toggle switches in the grooves of strip of the magnetic flux switch, made of non-magnetic material.

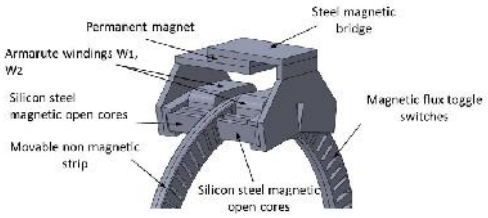

Fig. 1. Design of the arrangement of armature windings on the OMC, PM and magnetic bridges relative to the strip of the movable magnetic flux switch, Model I.

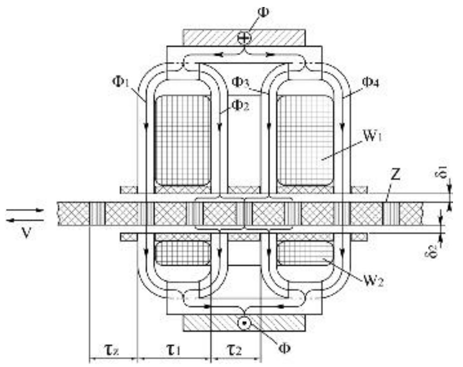

Fig. 2. The illustration of the magnetic circuit design of inductor with an armature winding and rods of OMC, which are separated from the strip of magnetic flux switch by air gaps, for k_1 and $k_2 = 1$, Model I.

When analysing this design, the ways of closing the magnetic leakage fluxes from a PM are not considered.

The magnetic toggle switches in the grooves of the strip of the magnetic flux switch are located with a uniform step τ_z equal to 360 electrical degrees. The teeth at the ends of the rods of the OMC are separated from the strip of the magnetic flux switch by air gaps δ_1 and δ_2.

Figure 4 shows a segment of the magnetic circuit of an inductor with an armature winding and an OMC with the number of pairs of rods equal to two, separated from the strip of the magnetic flux switch by an air gap δ_1. The distance between the pairs of rods in each OMC corresponds to Eq. (2):

$$\tau_1 = (k_1 + {}^1/_2)\,\tau_z. \tag{2}$$

The distance between the rods of adjacent OMC corresponds to Eq. (3):

$$\tau_2 = k_2\ \tau_z. \tag{3}$$

In Eqs. (2) and (3) k_1 and $k_2 = 1, 2 \ldots$ are functional coefficients, while k_1 determines the width of the slot where the armature windings are located, and k_2 corresponds to the number of rods.

During the movement of the strip of the magnetic toggle switches, there is a synchronous change in resistance in the external and internal rods of OMC. In accordance with this change, the values of the magnetic fluxes in the rods change according to the sinusoidal law, but in antiphase. Thus, for the sum of all magnetic fluxes, Eq. (4) is valid:

$$\Phi_1 + \Phi_2 + \Phi_3 + \Phi_4 = \Phi = const. \tag{4}$$

Consequently, the main resulting magnetic flux Φ in the magnetic bridge remains constant, which makes it possible to manufacture it from structural steel.

The calculation of the size of the magnetic circuit of the experimental model in the design process was carried out using the basic relations adopted for the design of the inductor machine [20].

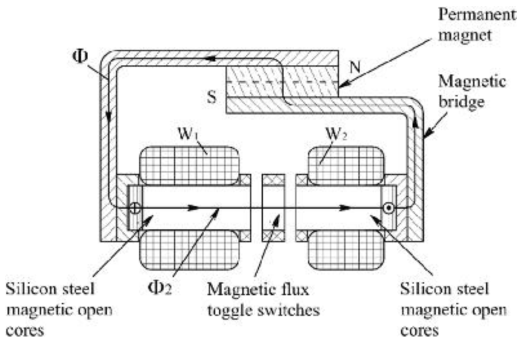

Fig. 3. The contour line of the circuit of closure of the main magnetic flux Φ and its fraction Φ_2, coupled with the windings W_1, W_2 of the inductor, from a PM with poles N-S in the inductor of the alternator, Model I.

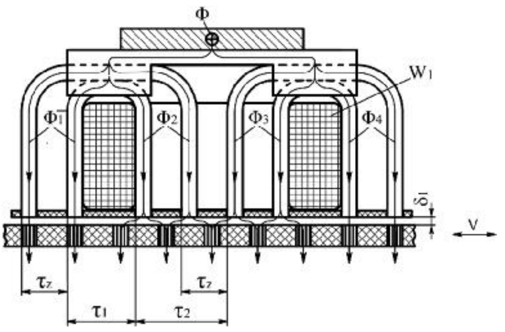

Fig. 4. The illustration of the magnetic circuit segment of inductor with an armature winding and rods of OMC, which are separated from the strip of magnetic flux switch by air gaps, for $k_1 = 1$ and $k_2 = 2$, Model I.

The toothed rotor in the considered device acts as a magnetic flux switch. In this case, the number of teeth Z on the rotor determines the frequency of flux pulsations in the OMC of the inductor. In general, the Z value can be considered as the number of teeth located on a strip of magnetic flux switch of length L, so the distance between the teeth is calculated by Eq. (5):

$$\tau_z = \frac{L}{Z}. \tag{5}$$

When the magnetic flux switch moves at a speed V, the frequency of the magnetic flux pulsations is determined by the switching number per unit of time; therefore, the fluctuation of the magnetic flux occurs in OMC with a flux switching frequency in the teeth and is determined according to Eq. (6):

$$f = \frac{n \cdot z}{60}, \quad (6)$$

where z – the number of magnetic toggle switches on the strip of the magnetic flux switch;

n – the frequency of cyclic oscillations or speed of rotation, rpm^{-1}.

As a result of the magnetic flux magnitude fluctuations with a frequency f between the maximum Φ_{max} and minimum Φ_{min} values, an electromotive force (EMF) arises in the armature winding with the number of turns W, whose value is determined in Eq. (7):

$$E = 4{,}44 \cdot W \cdot f \cdot \frac{(\Phi_{\max} - \Phi_{\min})}{2}. \quad (7)$$

b) Design of Model II

The manufacturing of OMC using tape winding technology contributes to a number of new properties in the alternator design. The proposed manufacturing technology is significantly simplified and becomes a waste-free technology. However, the rods of OMC and their teeth, made of laminated silicone steel sheets, are located perpendicular to the movement of the moving strip of the magnetic flux switch.

In this case, the width of the teeth is determined by the thickness of the sheets and their number, which makes them flexible and allows them to be positioned at different angles. Thus, the design of the inductor allows it to be adapted to operate with a magnetic flux switch, which may be linear, curved or closed in a ring, as shown in Fig. 1 and Fig. 5 [19], [21].

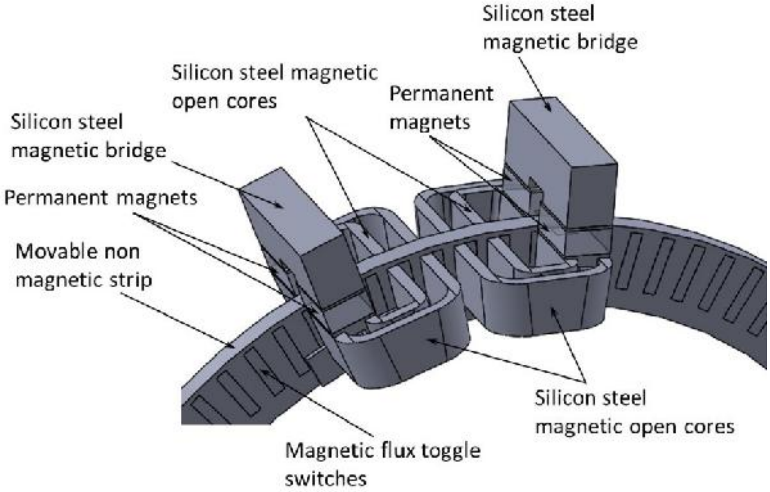

Fig. 5. The model of the arrangement of OMC, PM and magnetic bridges relative to the strip of the movable magnetic flux switch, Model II.

Due to the axial arrangement of the laminated silicone steel sheets, the magnetic circuit consisting of two groups of OMC separated by air gaps and a movable magnetic flux switch can be combined using magnetic bridges. Moreover, in the structure shown in Fig. 5 for $k_1 = 1$ and $k_2 = 1$, the magnetic fluxes from the PM are directed in the radial direction and are distributed in the rods of the OMC, as shown in Fig. 6.

In the considered design (Model II), PM are located on the side surface of laminated silicon steel sheets of the rods of OMC. The direction of the magnetic fluxes Φ_1, Φ_4 for PM and the magnetic fluxes Φ_2, Φ_3, Φ_5, Φ_6 corresponds to the polarity of the N-S PM located on the side rods of the OMC.

Magnetic fluxes from PM in the rods of OMC are divided into two directions, which corresponds to Eqs. (8) and (9):

$$\Phi_1 = \Phi_2 + \Phi_3 , \tag{8}$$

$$\Phi_4 = \Phi_5 + \Phi_6 . \tag{9}$$

The distribution of magnetic fluxes in sheets of laminated silicone steel of magnetic bridges for the case of closing magnetic fluxes Φ_1, Φ_2, Φ_3 for one pair of PM is shown in Fig. 7. In this case, during the movement of the strip of the magnetic flux switch, the magnitude of the magnetic fluxes in the magnetic bridges remains constant.

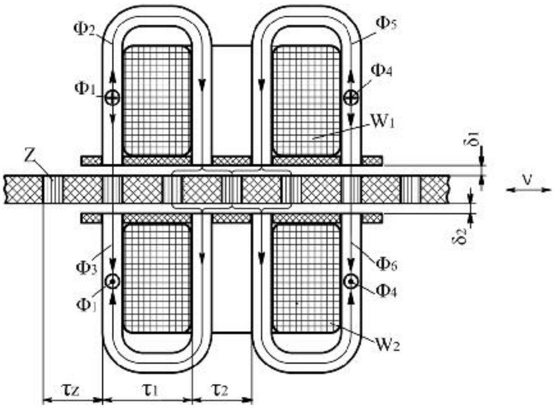

Fig. 6. Axial arrangement of the OMC with windings relative to the movement direction of the strip of magnetic flux switch. The direction of magnetic fluxes, for $k_1 = 1$ and $k_2 = 1$ is shown by arrows (Model II).

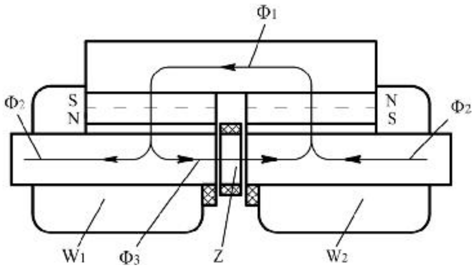

Fig. 7. Direction of magnetic fluxes Φ_1, Φ_2, Φ_3 in silicone steel of magnetic bridges and in the rods of OMC, separated by air gaps and by stripe of magnetic flux switch (Model II).

In the design of OMC with the number of rods equal to two ($k_2 = 2$), PM are located on steel spacers, which serve to distribute magnetic fluxes over the rods of OMC, as shown by the arrows in Fig. 8. In this case, the fluxes Φ_1, Φ_4 from PM in the rods of OMC of one section are divided into four flows in the rods:

$$\Phi_1 = \Phi_2 + \Phi'_2 + \Phi_3 + \Phi'_3, \tag{10}$$

$$\Phi_4 = \Phi_5 + \Phi'_5 + \Phi_6 + \Phi'_6. \tag{11}$$

As one can see, the magnetic fluxes in the rods of OMC can be conditionally divided into shunting magnetic fluxes Φ_3, Φ_6, Φ_3', Φ_6' and working magnetic fluxes Φ_2, Φ_5, Φ_2', Φ_5', which are connected with the armature windings W_1, W_2 and participate in EMF indication.

The polarity of the PM mounted on the steel spacers and the direction of the magnetic fluxes in the laminated silicone steel rods and magnetic bridges are shown in Fig. 9.

The considered inductor designs with an external closure of the magnetic flux expand the application scope of the axial flux switching PM alternator. In the proposed model, it is possible to place the strip of the magnetic flux switch on the disk connected to the rotary mechanical drive.

The use of an external magnetic circuit leads to the fact that the magnetic fluxes in the inductor are closed in two mutually perpendicular planes, which makes it possible to design new options of placement of OMC. At the same time, the study of the properties and estimation of the operating characteristics of these machines introduce a certain difficulty, since in the classical theory of electrical machines, taking into account their axial symmetry, it is sufficient to consider the flat pattern of the distribution of magnetic fluxes in the magnetic core.

To study the properties of the considered alternator designs, reliable results can be obtained only by analysing the volumetric picture of the magnetic field. In modern conditions, this can be done using computer simulation.

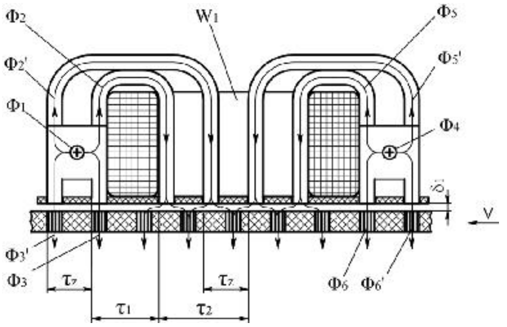

Fig. 8. The illustration of direction of magnetic fluxes from PM in rods of OMC with the number of rods equal to two for one inductor section for $k_1 = 1$ and $k_2 = 2$ (Model II).

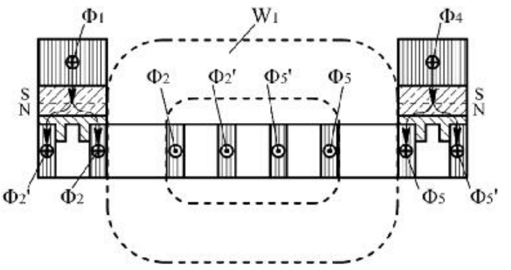

Fig. 9. The illustration of direction of magnetic fluxes created by PM in OMC, located opposite of the toggle switches on the strip of the magnetic flux switch for $k_1 = 1$ and $k_2 = 2$ (Model II).

3. MODELLING OF THE MAGNETIC FIELD DISTRIBUTION IN THE INDUCTOR

The analysis of the density distribution of magnetic fluxes in OMC was carried out by 3D modelling of the magnetic field using EMWorks software. In the generator models under investigation, the number of pairs of teeth for each of the OMC equals $k_2 = 2$. The 3D models of the alternators with the representation of the magnetic field density distribution in the rods of OMC and in the air gap are shown on Figs. 10–13, where the given palette of intensity (T) makes it possible to estimate the degree of saturation of magnetic circuit sections.

Practical studies of the characteristics of alternators and modelling of the magnitude of magnetic fluxes were carried out using OMC made of laminated steel type 23ZH90 with a thickness of 0.23 mm. Figure 14 shows one section of OMC with two pairs of teeth and the outer core size of 2.07 mm × 22.9 mm × 18.0 mm × 9.7 mm and the inner one of 2.07 mm × 12.7 mm × 16.0 mm × 9.7 mm. The size of the air gaps $\delta_1 = \delta_2 = 0.2$ mm.

The dimensions of the PM from NdFeB (N48) for Model I are 22.9 mm × 25.4 mm × 3 mm and for four magnets of Model II are 8.1 mm × 12 mm × 4.5 mm. The winding of the experimental models consists of two coils with the number of turns equal to $W = W_1 + W_2 = 215 + 215 = 430$. Winding resistance $R_w = 2.6 + 2.6 = 5.2$ (Ohm), inductance $L_w = 34.1$ (mH).

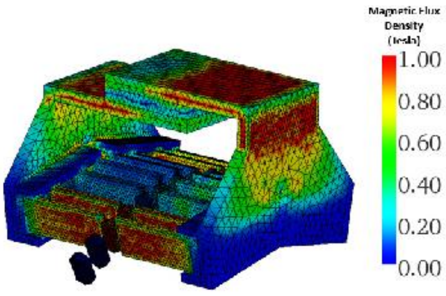

Fig. 10. The design of the investigated model with the representation of the magnetic field density distribution in the rods of OMC and the palette of its intensity (T), (Model I).

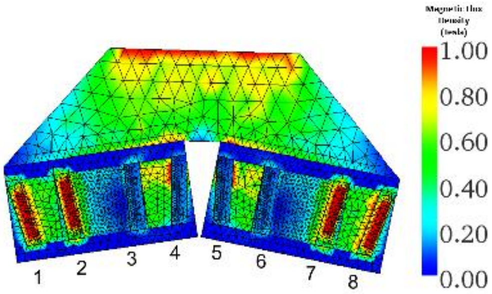

Fig. 11. The picture of the distribution of the magnetic field in the rods of OMC at the boundary with the air gap and the palette of its intensity (T), (Model I).

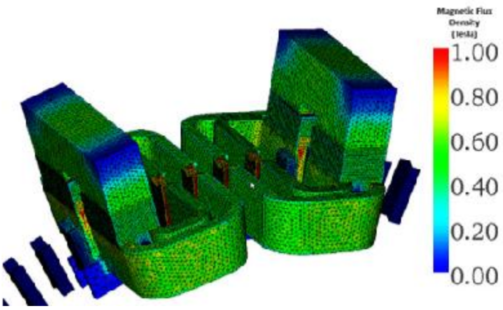

Fig. 12. The design of the investigated model with the representation of the magnetic field density distribution in the rods of OMC and the palette of its intensity (T), (Model II).

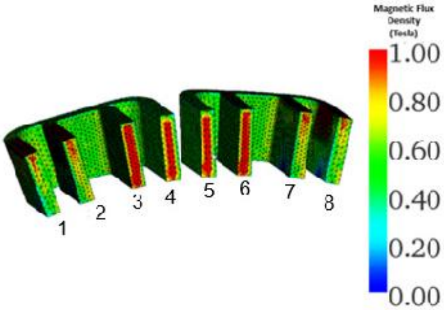

Fig. 13. The 3D picture of the distribution of the magnetic field in the rods of OMC at the boundary with the air gap and the palette of its intensity (T), (Model II).

Figure 15 shows the rated value of the magnetic field in the outer 1, 2, 7, 8 and in the inner 3, 4, 5, 6 teeth of the OMC (see Fig. 8) for displacing the magnetic flux switch of Model II by an angle τ_z with a step of 0.2 degrees.

To compare the performance of Model I and Model II, the results of calculating the magnitude of the magnetic flux corresponding to the two positions of the strip of the magnetic flux switch were used.

In the first case, the magnetic toggle switches are positioned against rods 1, 2, 7, 8, which correspond to the minimum value of the working magnetic flux Φ_{min} in the rods 3, 4, 5, 6 of OMC. The examples of visualization of the magnetic flux distribution in the OMC for this position of the stripe of magnetic flux switch for Model I are presented in Figs. 10 and 11.

In the second case, when the strip of the magnetic flux switch is displaced by a value of τ_z, the magnetic toggle switches are located against rods 3, 4, 5, 6, which correspond to the maximum value of the working magnetic flux Φ_{max} in these rods. The examples of visualization of the magnetic flux distribution in the OMC for this position of the strip of magnetic flux switch for Model II are presented in Figs. 12 and 13.

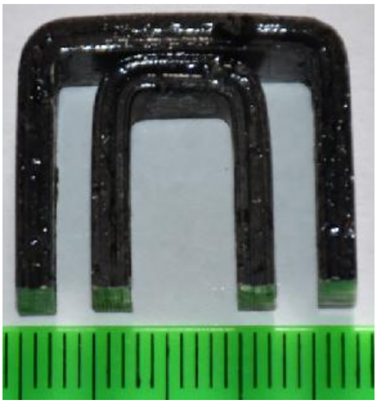

Fig. 14. One section of OMC with two pairs of teeth from laminated steel, size scale in mm.

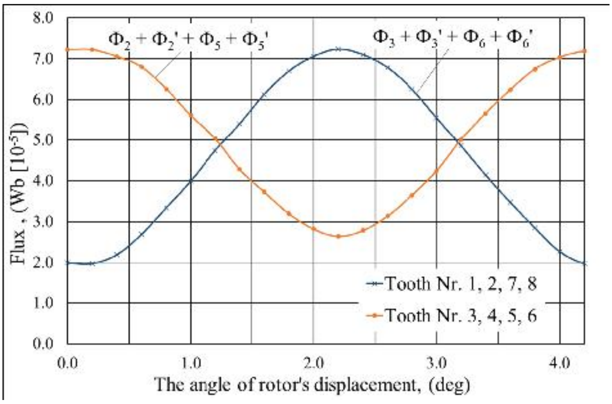

Fig. 15. Magnetic flux changes in the air gap of the alternator in the outer 1, 2, 7, 8 and in the inner 3, 4, 5, 6 teeth for the angle of rotor displacement τ_z for $k_1 = 1$ and $k_2 = 2$, (Model II).

The results of the magnetic flux values obtained for the corresponding type of PM and the size of the OMC allow estimating the value of EMF in the windings by Eq. (5), which occurs as a result of flux variations at a frequency of flux fluctuation f = 300 (Hz).

The rated values of magnetic fluxes in the teeth of OMC for two positions of the magnetic flux switch for Model I and II are given in Table 1. To compare the efficiency of these two models, Table 1 shows the values of the weights of OMC with a magnetic bridge and the weights of PM.

Table 1. The Rated Values of Magnetic Fluxes in the Teeth of OMC for two Positions of the Magnetic Flux Switch for Models I and II

Model	Magnetic flux of teeth Φ_{max} 10^{-5}, *Wb*					Magnetic flux of teeth Φ_{min} 10^{-5}, *Wb*					EMF	Core weight	PM weight
	3	4	5	6	**Total**	3	4	5	6	**Total**	*V*	*kg*	*Kg*
I	1.40	1.26	1.25	1.40	**5.31**	0.22	0.21	0.21	0.22	**0.86**	12.74	0.20	0.013
II	1.88	1.74	1.74	1.88	**7.24**	0.66	0.68	0.65	0.66	**2.65**	13.14	0.12	0.013

The results of these calculations show that the chosen dimensions of the OMC and magnets are sufficient to induce the specified EMF value by switching the magnetic flux in the windings of the generator.

The test sample allows determining the actual technical characteristics of the generator with an axial arrangement of the inductor and estimating the potential for its use as a power supply source for bicycle electronics devices. Thus, the simulation results can serve as a reliable basis for designing a generator with specified characteristics.

4. DISCUSSION

In the article, the novel designs of alternators with PM have been presented and their properties have been discussed and evaluated. The proposed design is characterised the ability of alternator to be connected to the bicycle wheel, which serves as a mechanical drive for the mentioned generator.

The authors have proposed two options for the design of alternators with OMC using external magnetic flux closure from PM. It should be noted that in the design of Model II, the arrangement of PM directly on the rods of OMC leads to a decrease in the weight of the magnetic circuit with the same weight of PM.

The results of the study show that the proposed technical solution has good prospects to be used as a power source for charging bicycle electronic devices. Furthermore, it has been shown that such generators can be manufactured using a waste-free technology for strip OMC. This technology significantly reduces the production costs of OMC.

The modelling of the distribution of magnetic fluxes in the OMC of the inductor and analysis of the created device show that the capacity of generator can be varied by changing its dimensions and the number of the toggle switches on the rotor. This allows the alternator to be adapted to the load requirements – power banks and bicycle electronics.

ACKNOWLEDGEMENTS

The research has been supported by the ERDF project “Environmentally Friendly Small Power Generator with the Rotor Linear Motion (DrauGen)” No. 1.1.1.1/18/A/125.

REFERENCES

1. Torkaman, H., Ghaheri, A., & Keyhani, A. (2019). Axial Flux Switched Reluctance Machines: A Comprehensive Review Of Design And Topologies. *IET Electr. Power Appl.*, 13 (3), 310–321.
2. Radwan-Pragłowska, N., Wegiel, T., & Borkowsk, D. (2020). Modelling of Axial Flux Permanent Magnet Generators. *Energies, 13* (5741), 1–28.
3. Spooner, E., Tavner, P., Mueller, M.A., Brooking, P.R.M., & Baker, N.J. (2004). Vernier Hybrid Machines for Compact Drive Applications. In: *Second International Conference on Power Electronics, Machines and Drives (PEMD 2004)*, (pp. 452–457), 31 March–2 April 2004, Edinburgh, UK.
4. Raihan, M.A.H., Baker, N.J., Smith, K.J, & Almoraya A.A. (2018). Development of Low Translator Mass Linear Vernier Machine for Wave Energy Power Take Off. In: *The 7th International Conference on Renewable Power Generation*, (pp. 1–5), 26–27 September 2018, DTU, Lyngby, Copenhagen, Denmark.
5. Rauch, S.R., & Johnson, L.J. (1955). Design Principles of Flux Switch Alternators. *IEE Trans Power Apparatus and Systems, Part III, 74* (3), 1261–1268.
6. Kwon, J.W., Lee, J.H., Zhao, W., & Kwon, B.I. (2018). Flux-Switching Permanent Magnet Machine with Phase-Group Concentrated-Coil Windings and Cogging Torque Reduction Technique. *Energies*, *11* (2758), 1–11.

7. Diab, H., Amara, Y., & Barakat, G. (2020). Open Circuit Performance of Axial Air Gap Flux Switching Permanent Magnet Synchronous Machine for Wind Energy Conversion: Modeling and Experimental Study. *Energies, MDPI. Open Access Journal*, *13* (4), 1–19.
8. Zhu, Z.Q., & Chen, J.T. (2010). Advanced Flux-Switching Permanent Magnet Brushless Machines. *IEEETrans. Magn.*, *46*, 1447–1453.
9. Andrada, P., & Martínez, F. (2016). Flux Switching Alternators for Small Wind Generation. *Renew*. *Energy Power Qual. J.*, *1*, 67–68.
10. Wilfried, S. (1994). *Hub Generator, Especially for Bicycles*. Patent EP0591724A1.
11. Bridgestone Cycle Co. (1995). *Hub Generator for Bicycle*. Patent JPH0710057A.
12. Shimano KK. (2003). *Claw-Pole Generator and Hub Dynamo for Bicycle*. Patent JP2003333777A.
13. Bezrukovs, V., Bezrukovs, Vl., Bezrukovs, D., Konuhova, M., Berzins, A., & Trokss, J. (2022). Magnetic Flux Switching Type Permanent Magnet Generator for Bicycles: Modelling and an Experimental Study. *Latvian Journal of Physics and Technical Sciences, 3* (59), 48-57.
14. Bezrukovs, V., & Levins, N. (2008). *Generator for Bicycle*. Patent LV13750.
15. Bezrukovs, V., & Levins, N. (2009). *Bicycle Generator*. Patent WO2009084938.
16. Bezrukovs, D., Bezrukovs, V., Bezrukovs, Vl., & Levins, N. (2011). *Contactless Generator for Bicycle.* Patent LV 14377.
17. Bezrukovs, D., Bezrukovs, V., Bezrukovs, Vl., & Levins, N. (2012). *Axial Inductor Generator for Bicycle*. Patent LV 14550.
18. Bezrukovs, D., Bezrukovs, V., Bezrukovs, Vl., & Levins, N. (2013). *Inductor Generator for Bicycle.* Patent LV 14695.
19. Bezrukovs, V., Bezrukovs, Vl., Bezrukovs, D., Konuhova, M., & Berzins, A. (2020). *Magnetic Flux Switching Type Permanent Magnet Generator*. Patent LV15501.
20. Dombur, L. (1984). *Axial Inductor Machines*. Riga: Zinatne, 247.
21. Bezrukovs V., Bezrukovs Vl., Bezrukovs D., Konuhova M., Berzins A. (2022): *Magnetic flux switching type permanent magnet generator*. EP3955439A1·2022-02-16.

LATVIAN JOURNAL OF PHYSICS
AND TECHNICAL SCIENCES
2022, N 3

DOI: 10.2478/lpts-2022-0026

THE STUDY OF PROPERTIES OF AN AXIAL FLUX SWITCHING PERMANENT MAGNET ALTERNATOR WITH OPEN MAGNETIC CORES

V. Bezrukovs, Vl. Bezrukovs*, M. Konuhova,
D. Bezrukovs, A. Berzins

Engineering Research Institute
“Ventspils International Radio Astronomy Centre”
Ventspils University of Applied Sciences,
Inzenieru Str., 101, LV-3601 Ventspils, LATVIA
*e-mail: vladislavsb@venta.lv

The article studies magnetic field distribution in the alternator inductors with an axial arrangement of open magnetic cores (OMC) and an external closure of the magnetic flux. The study compares the efficiency of magnetic flux utilization for four models with different modifications of the geometry of the magnetic circuit of inductors. The analysis of the density distribution of magnetic flux in OMC is carried out by 3D modelling of the magnetic field using EMWorks software. Based on the experimental study of the properties of the base model, the influence of the configuration of the magnetic circuit of the inductor on the efficiency of the alternator is shown. The results are presented in the form of tables and diagrams characterising changes in magnetic fluxes and electromotive force (EMF) in relative units. The results provide the grounds for assessing the potential and possible limits of optimization with respect to the size of air gaps and dimensions of the magnetic flux toggle switches. The study indicates that the proposed alternator can be adapted for various load requirements and optimized for various applications, such as charging power banks and powering bicycle electronics. The study also demonstrates that for such generators, OMC can be manufactured using a waste-free strip production technology.

Keywords: *Bicycle electronics, magnetic field distribution, modelling of magnetic fields, permanent magnet machines.*

1. INTRODUCTION

Current global trend towards the use of environmentally-friendly alternative energy sources for autonomous low-power loads re-ignited interest in machines capable of converting low-speed movement into electrical power. Axial flux switched reluctance machines exhibit unique characteristics that demonstrate their superiority over other topologies in specific applications. A number of researchers have studied the efficiency of the design and constructed structures in different types of these machines [1], [2].

More recently, new forms of the vernier hybrid permanent magnet machines [3], [4], which are based on the principle of variable-reluctance have come in sight. Along with simple design, these machines offer a compact direct drive solution for low-speed and low-power applications.

A similar principle of variable reluctance is used in permanent magnet machines with magnetic flux switching. This type of machines has been first considered by Rauch and Johnson [5], and can be viewed as an evolution of an inductor generator. The articles [6]–[9] present the results of studies of magnetic flux switching machines by a number of authors.

The authors of this study used the magnetic flux switching principle for the development of a new bicycle generator design. The proposed approach made it possible to combine in one device the supporting structures of the frame and bicycle wheels to create an inductor-type generator [10]–[12].

The magnetic circuit of the alternator inductor, proposed by the authors in [13], [14], is produced using the strip technology of manufacturing of OMC and one-sided external closure of the magnetic flux. Figure 1 shows the design of the magnetic circuit, which includes fixed OMC, PM, magnetic bridges and the MFV. In turn, the MFV consists of a non-magnetic strip, in which the MFTS are embedded. Further in the article, the authors consider this design as a base model for comparison.

Previous works on this topic [15], [16] present the results of the studies of an axial flux switching permanent magnet alternators, the design of which is intended to work with a rotary motion drive. In these devices, OMC are manufactured using strip technology. In this case, the teeth at the ends of the rods of the OMC are located perpendicular to the movement of the MFV. This approach opens up new possibilities for the optimization of the toothed zone of the inductor by changing the number of sheets of laminated silicone steel in the teeth.

At the same time, the rods, formed in the form of a stack of laminated steel sheets, are flexible, which allows the angle of inclination of the teeth to be changed in relation to the direction of movement of the MFV. Thus, the use of the technology proposed by the authors allows designing a complex geometry of the magnetic circuit of the alternator and adapting it for placement on a fixed drive housing. In this case, magnetic flux fluctuations are formed by linear or rotational movement of the MFV.

This article presents the study results of properties of several new designs of the magnetic circuit of the alternator inductor with an axial arrangement of the OMC. The comparison of the considered design solutions was carried out using the simulation of the distribution of magnetic fluxes in the rods of OMC.

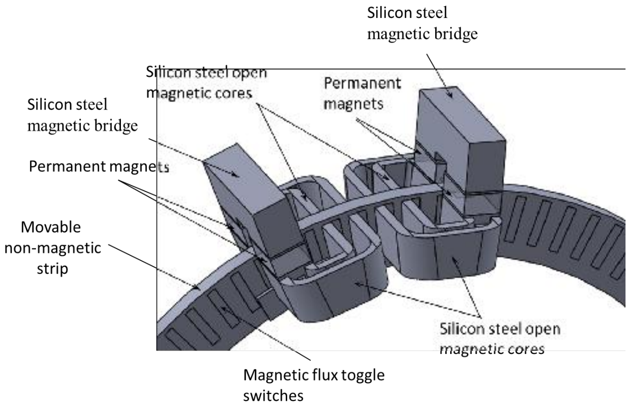

Fig. 1. The model of the arrangement of the OMC, PM and magnetic bridges relative to the MFV – movable non-magnetic strip with embedded MFTS.

The study results are presented in the form of diagrams and expressed in relative units for comparison with the base model. This allows evaluating the potentials and limits of changing the size of air gaps and dimensions of the MFTS, as well as optimising the design of the alternator and improving its performance.

2. MODELLING THE DESIGN OF AN ALTERNATOR INDUCTOR WITH OMC

Let us consider some possible options for the location of magnetic cores and magnets relative to the moving MFV. In this case, the initial requirements for the development of the design of alternator structures follow from the conditions of its operation as a power source for bicycle electronics. It appears that generators dimensions and shape depend on the place of installation on the frame and the possibility of connecting to the bicycle wheel.

For example, Fig. 2 shows the placement of a prototype of an alternator inductor on a bicycle frame and an MFV instead of a disc brake attached to the rear wheel. In Fig. 2, one can see that the alternator inductor is fixed and this greatly simplifies the connection of the terminals of its armature winding to the voltage converter unit, which serves to match the output voltage with the input of bicycle electronics. However, the problem lies in the limited space for placing a part of the magnetic core between the movable MFV and the spokes of the wheel.

The main dimensions of the alternator are determined in accordance with the rated power and voltage value at the output armature winding. However, there is no proven methodology for designing such a device in accordance with the specified requirements and characteristics. Therefore, to calculate the magnetic circuit, the method of 3D modelling of the magnetic field using the EMWorks software has been used.

Initial calculations of the magnetic circuit made it possible to determine the main dimensions and design of the developed device. Alternators were designed in such a way so that their shape would allow solving the problem of placing OMC on a bicycle. Some of the possible design alternatives that have an asymmetrical arrangement of OMC relative to the MFV are shown in Figs. 3 and 4.

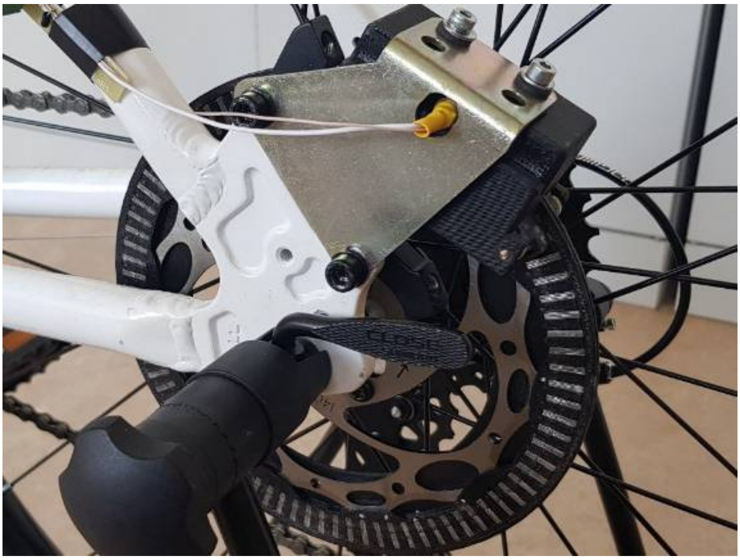

Fig. 2. Placement of the inductor of an axial flux switching PM alternator on a bike frame and location of a movable MFV on the rear wheel brake disc.

Figure 3a shows the design options for the magnetic circuit of the inductor using the example of Model I and Model II, where OMC are located, respectively, perpendicular and parallel to the direction of movement of the MFV. Figure 4a shows Model III and Model IV, in which the OMC are parallel with respect to the direction of movement of MFV.

The study of the properties of the presented alternator design options was carried out by modelling the distribution of the magnetic field in the inductor with a one-sided asymmetric arrangement of OMC. The calculations were performed for two positions of MFTS, shifted by 180◦ electrical degrees.

In the considered special designs of alternators, it has been ensured that the armature winding is located on the rods of OMC, through which the working magnetic flux is closed. At the same time, in the limited space between the disc with MFTS and the spokes of the bicycle wheel, only the magnetic flux contactor will be located.

In the figures shown, position 0° corresponds to the value of the minimum working magnetic flux Φ_{min}, and position 180° corresponds to the value of the maximum working magnetic flux Φ_{max}. In this case, on a scale tied to the colour palette in Figs. 3, 4 it is possible to estimate the magnitude of the magnetic flux density for the sections of the magnetic circuit shown in the following figures: (b) in the inductor; (c) in the MFTS; (d) in the OMC and (e) magnetic flux density in the magnetic closure, view from the side of the air gap.

As a result of the magnetic flux fluctuations with a frequency f between the maximum Φ_{max} and minimum Φ_{min} values, an EMF arises in the armature winding with the number of turns W, whose value is determined in Eq. (1) [17]:

$$E = 4,44 \cdot W \cdot f \cdot \frac{(\Phi_{\max} - \Phi_{\min})}{2}. \qquad (1)$$

The results of the study of the models performed on the basis of the assessment of the values of the working magnetic fluxes, taking into account the dimensions of their OMC and PM, are given in Table 1. In this case, the EMF value is calculated for the flux switching frequency *f* = 300 Hz and corresponds to the number of turns of the armature winding wire, which can be laid in the OMC for each model. For comparison, the table shows the weights of PM and OMC and the ratio of their weights.

The above results suggest that the considered modifications of alternators can be used as a basis for designing devices with special requirements for the external dimensions and geometry.

At the same time, as can be seen from the comparison of the design of the models, the efficiency of the alternators largely depends on the size and geometry of the OMC and PM.

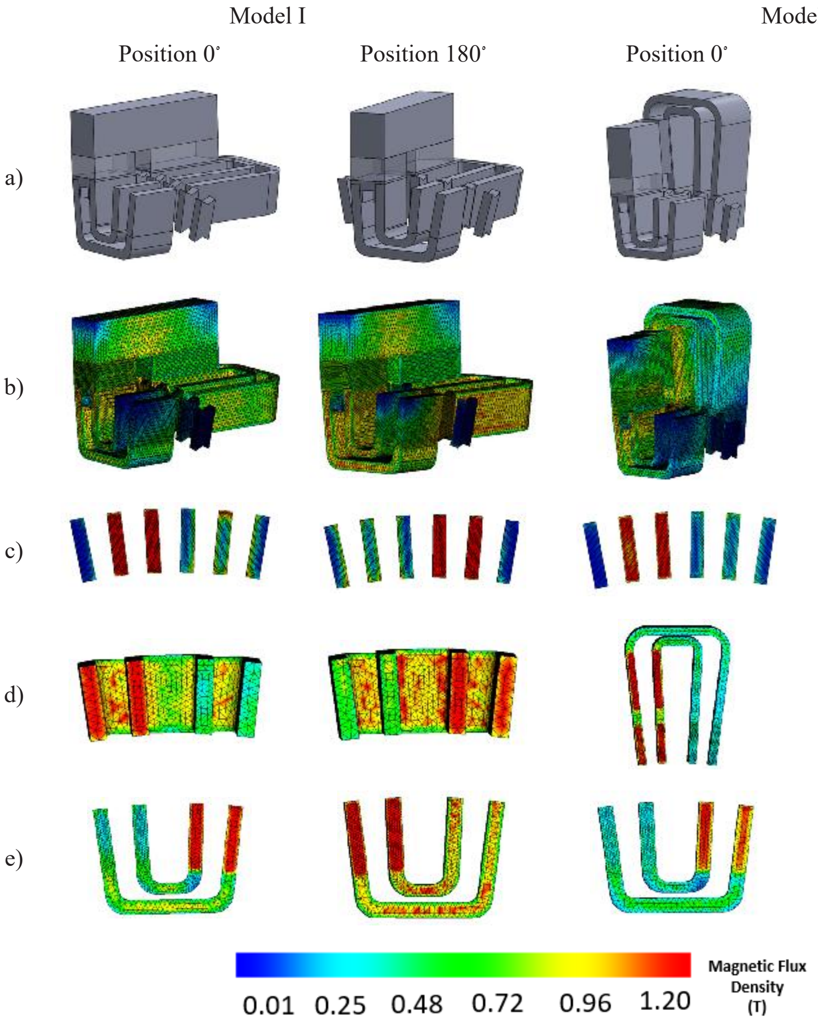

Fig. 3. The 3D modelling of the magnetic field in the alternator with one-sided asymmetric arrangement of OMC relative to the MFV for two positions of MFTS, offset by an angle of 180°:

a) magnetic circuit design of the inductor with perpendicular (Model I) and parallel (Model II) OMC placement; and magnetic flux density b) in the inductor; c) in the MFTS; d) in OMC, and e) in the magnetic closure, view from the side of the air gap.

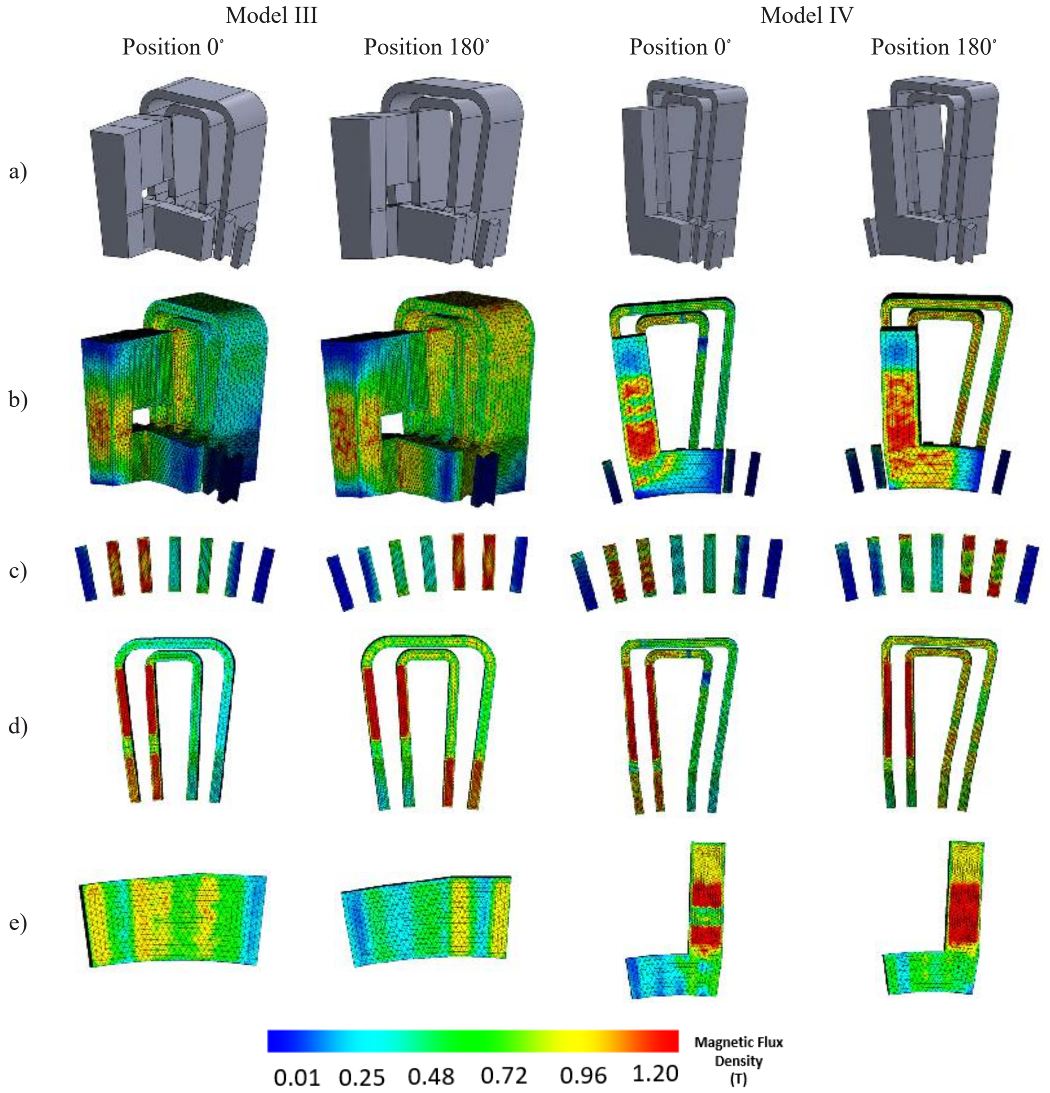

Fig. 4. The 3D modelling of the magnetic field in alternator with one-sided asymmetric arrangement of OMC relative to the MFV for two positions of MFTS, offset by an angle of 180°:

a) magnetic circuit design of the inductor with parallel OMC placement (Models III and IV); and magnetic flux density b) in the inductor; c) in the the MFTS; d) in OMC, and e) in the magnetic closure, view from the side of the air gap.

Table 1. The Results of Modelling the Values of the Working Magnetic Fluxes for the Considered Alternator Models: The Maximum Φ_{max} and Minimum Φ_{min} Magnetic Flux, EMF, the Weights of PM and OMC

Model	Magnetic flux Φ_{max}, 10-5 Wb	Magnetic flux Φ_{min}, 10^{-6} Wb	EMF, V	Weight of the PM, 10^{-3} kg	Weight of the OMC,·10^{-3} kg	The ratio of the weights
I	4.75	16.3	7.55	9.7	72.2	0.1382
II	4.32	8.60	9.60	7.1	58.0	0.1225
III	4.19	9.87	8.88	6.4	61.6	0.1048
IV	3.03	9.18	6.77	6.5	47.5	0.1368

3. THE INFLUENCE OF MFV ON THE PROPERTIES OF AN ALTERNATOR

To explore the influence of the design on the efficiency of alternator with OMC, the model shown in Fig. 1 was selected. As a research tool, the method of 3D modelling of the distribution of magnetic field using SolidWork software with the EMWorks package was used.

The study of the characteristics of the alternators and physical modelling were carried out using OMC made of laminated steel type 23ZH90 with a thickness of 0.23 mm. Figure 8 shows one section of the OMC with two pairs of teeth and the outer core size of 2.07 mm × 22.9 mm × 18.0 mm × 9.7 mm and the inner one of 2.07 mm × 12.7 mm × 16.0 mm × 9.7 mm. The size of the air gaps $\delta_1 = \delta_2 = 0.2$ mm.

The dimensions of the PM from NdFeB (N48) are 8.1 mm × 12 mm × 4.5 mm. The armature winding of the experimental models consists of two coils with the number of turns equal to $W = W_1 + W_2 = 215 + 215 = 430$. Winding resistance $R_w = 2.6 + 2.6 = 5.2$ (Ohm), inductance $L_w = 34.1$ (mH).

The distribution pattern of the magnetic field in the inductor for the position of MFTS equivalent to 180° is shown in Fig. 5. In this position, as can be seen in Fig. 6, in the teeth 3, 4, 5, 6 of the magnetic rods on the side of the air gap, the magnetic flux has the maximum value.

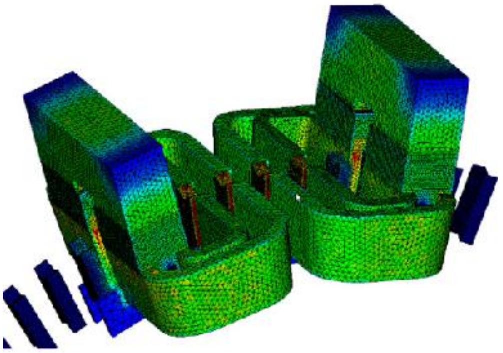

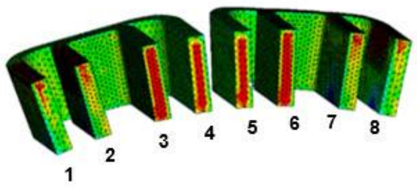

Fig. 5. The design of the investigated model with the representation of the magnetic field distribution in the rods of OMC and the palette of its flux density in Tesla (T).

Fig. 6. The 3D picture of the distribution of the magnetic flux in the rods of the OMC at the boundary with the air gap.

The rated values of magnetic fluxes in these teeth of OMC for two positions of the MFTS shifted by 0° and 180° electrical degrees are given in Table 2, where the values of the weights of OMC with magnetic bridges and the weights of PM are shown. The table also provides the EMF values calculated using Eq. (1) as a result of examining the experimental sample.

As the MFV moves, the reluctance of the air gap between the teeth of the OMC and the MFTS cyclically changes. As a result, the magnetic flux associated with the armature winding placed on the rods 3, 4, 5, 6 changes according to the harmonic law.

Table 2. The Rated Values Φ_{max} and Φ_{min} of Magnetic Fluxes in the Teeth 3, 4, 5, 6 of OMC for Two Positions of the MFTS Shifted by 0° and 180° Electrical Degrees, and Rated and Experimental EMF Values

Magnetic flux of teeth Φ_{max}, 10^{-5} *Wb* Magnetic core					Magnetic flux of teeth Φ_{min}, 10^{-5} *Wb* PM					Rated EMF	Exp. EMF	Weight	
												Magnetic core	PM
3	4	5	6	**Sum**	3	4	5	6	**Sum**	*V*	*V*	10^{-3} *kg*	10^{-3} *kg*
1.88	1.74	1.74	1.88	7.24	0.66	0.68	0.65	0.66	2.65	13.1	12.0	120	13

Figure 7 shows the rated value of the sum of magnetic fluxes Φ_1 in the outer 1, 2, 7, 8 and Φ_2 in the inner 3, 4, 5, 6 teeth of the OMC (see Fig. 6) for displacing the MFTS by an angle of 180° electrical degrees.

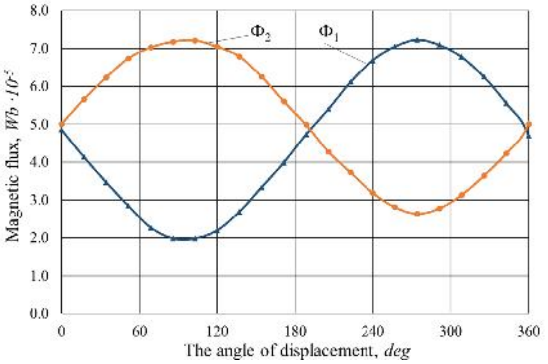

Fig. 7. Change of the magnetic fluxes (Φ_1 and Φ_2) in the air gap of the alternator in the outer 1, 2, 7, 8 and internal 3, 4, 5, 6 teeth in relation to the displacement of the rotor.

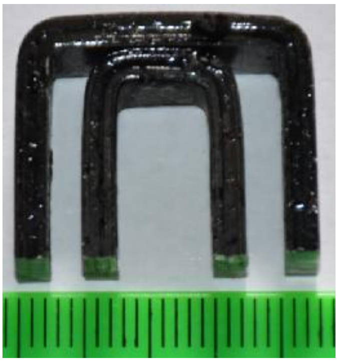

Fig. 8. One section of OMC with two pairs of teeth from laminated steel, size scale in mm.

The results of experimental studies discussed in [15] show that the employed 3D model together with EMWorks software allow estimating the values of magnetic fluxes in the inductor with high reliability. Thus, the study of the influence of the shape modifications of alternator on its power characteristics can be carried out in comparison with the base model, which is used as a physical experimental sample. The calculation results provide the grounds for performing design optimizations, which would lead to an increase in the efficiency of the considered alternator model.

As the first step, let us consider the effect of the size of the MFTS on the EMF value. The elongated rectangular shape of these elements to a certain extent depends on the method of their attachment in the strip of the MFV, which is made of a non-magnetic dielectric material such as glass fibre. Figure 9 shows the relative change in the EMF value for three modifications of the MFTS fastening using protrusions and grooves at the ends of elements.

In this study, the shape of the MFTS with grooves at the ends, as presented in Fig. 10, has been adopted as the base version. The dimensions of this package made of laminated silicone steel are as follows: thickness b_z – 2.1 mm; height h_z – 10 mm; width l_z – 4 mm.

As can be seen, the change in shape led to a decrease in the EMF value for modifications I and III. Thus, in further calculations, the MFTS will be used, which have a modification shape of II.

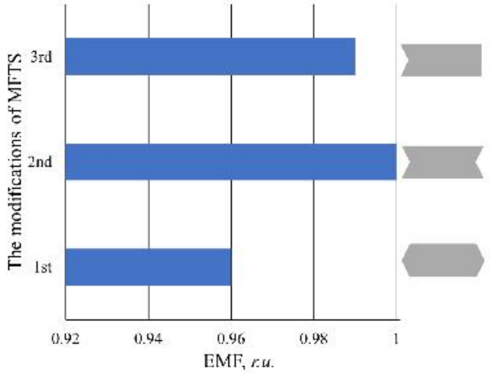

Fig. 9. The EMF value in relative units for three modifications of the MFTS of the alternator.

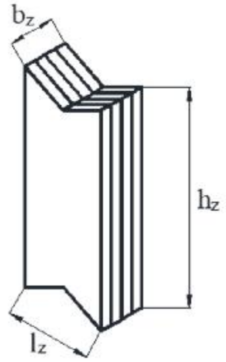

Fig. 10. The dimensions of MFTS: package thickness b_z, height h_z and width l_z.

The critical dimensions that determine the properties of an alternator include thickness b_z and width l_z of the MFTS package, as well as the size of the air gap δ between the teeth of the OMC and the MFV. The choice of the value of these parameters has a significant impact on the efficiency of the device and ultimately determines its power and output voltage. To estimate this impact, it was necessary to create the number of models where selected parameters under investigation were altered. For each of these modifications, the values of magnetic fluxes and EMF were compared to the base version of the device.

Figure 11 shows the modelling results of the magnetic flux for the position of the MFTS at 0° and 180° electrical degrees and corresponding EMF for MFTS package thicknesses b_z from 1.3 to 2.3 mm.

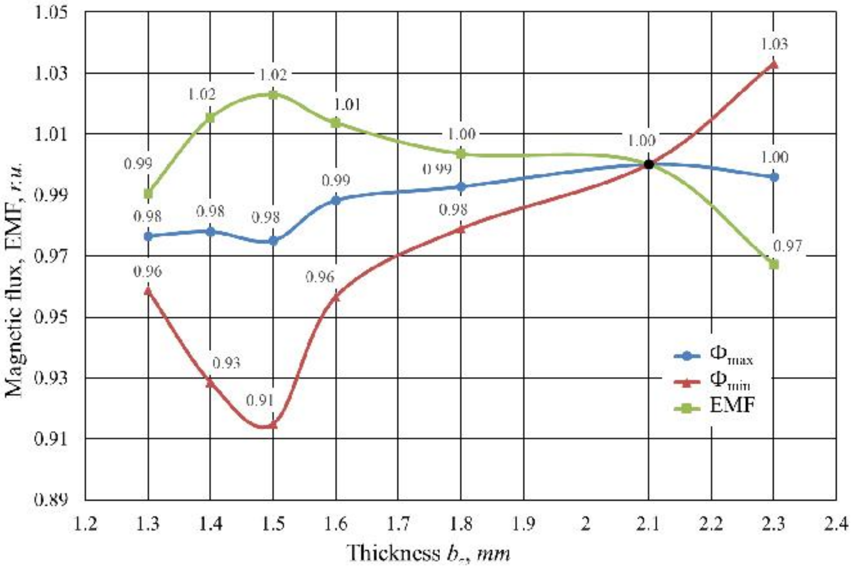

Fig. 11. The magnetic fluxes Φ_{max} and Φ_{min} and corresponding EMF in relative units for MFTS package thicknesses b_z from 1.3 to 2.3 mm.

The change in the values of the magnetic fluxes Φ_{max} and Φ_{min} in this case has a nonlinear character, which leads to the appearance of an extreme zone, where the difference in the amplitudes of the magnetic flux has a maximum value. This, in turn, affects the EMF value, which increases by 2.2 % as the thickness b_z of the MFTS package becomes close to 1.5 mm. It is apparent that the MFV of this design will reduce the overall weight of the MFTS and will not result in a decrease in EMF.

The influence of change in MFTS package width l_z to the magnetic flux for two package thicknesses b_z 1.5 mm and 2.1 mm is shown in Fig. 12. The performed calculations show that the size of the width l_z of the MFTS also has a significant effect on the ratio of the values of the magnetic fluxes Φ_{max} and Φ_{min} and, as can be seen in Fig. 13, is reflected in the EMF value.

It can be noted here that the efficiency of the alternator increases when the MFTS package width l_z becomes close to 5.0 mm with its thickness b_z of 1.5 mm. For the MFTS package dimensions, the EMF value increases by 9 % compared to the base design of the device.

One of the obvious ways to reduce the reluctance of magnetic circuit is to reduce the size of the air gap δ. For the model under investigation, in which the size of the air gaps is $\delta_1 = \delta_2 = 0.2$ mm, an increase in this value leads to a decrease in the magnetic flux and, accordingly, a decrease in the EMF value.

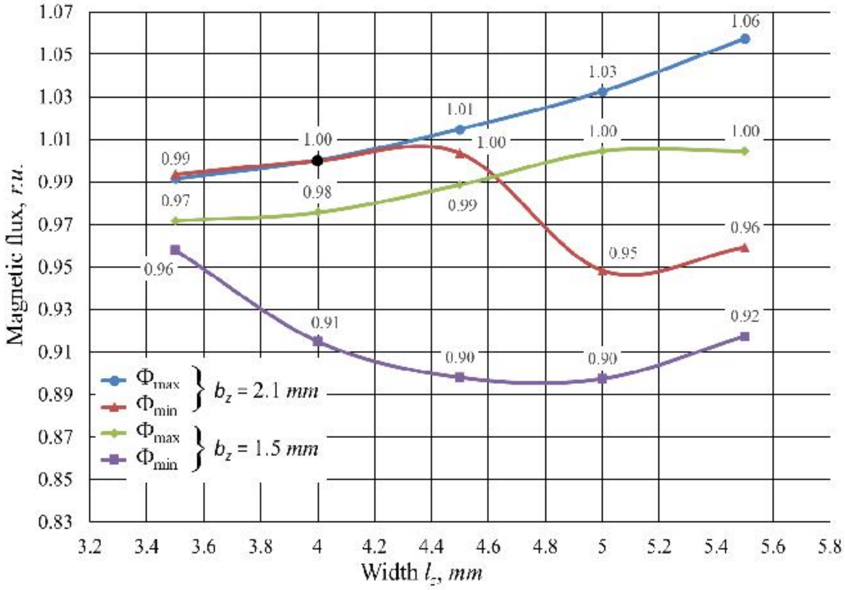

Fig. 12. The magnetic fluxes Φ_{max} and Φ_{min} in relative units for MFTS package width l_z from 3.5 to 5.5 mm, for two package thicknesses b_z 1.5 and 2.1 mm.

The modelling results of the magnetic flux for a variable air gap δ are shown in Fig. 14. This figure shows the magnetic fluxes $\Phi_{\max}$ and $\Phi_{\min}$ and the corresponding EMF values for the MFTS package with thickness of 2.1 mm and the width of 4 mm. As can be seen in Fig. 14, a decrease in the size of the air gap δ leads to a significant increase in EMF; however, the bounds of this change are limited by the quality of the surface finish of the strip of the MFV.

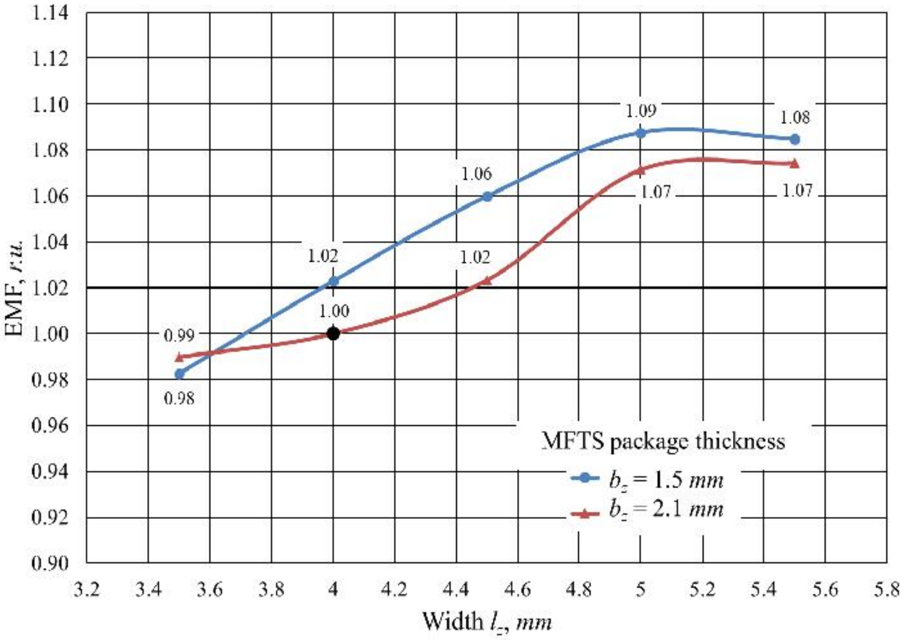

Fig. 13. The EMF values in relative units for MFTS package width l_z from 3.5 to 5.5 mm, for two package thicknesses b_z 1.5 and 2.1 mm.

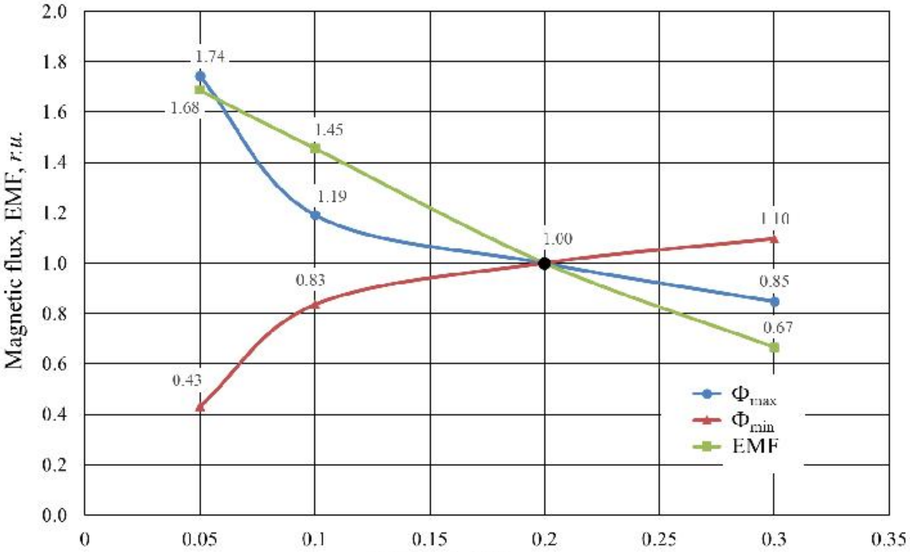

Fig. 14. The magnetic fluxes Φ_{max} and Φ_{min} and corresponding EMF in relative units for air gap δ from 0.05 to 0.3 mm for MFTS package thickness b_z 2.1 mm and width l_z 4 mm.

4. DISCUSSION

The authors have proposed several new designs of alternators with PM and axial arrangement of OMC. The proposed device is characterised by its ability to change the configuration of the arrangement of the OMC of the inductor relative to the MFV. This allows adapting the design of the alternator for mounting it on the bicycle frame and coupling the moving part with the wheel.

The estimation of parameters of the proposed design solutions has been carried out using 3D modelling of the distribution of magnetic flux in the rods of OMC and on the basis of experimental samples. The study results, shown in the form of graphs, are presented in relative units, which allow one to estimate the potentials and limits of optimization of the size of air gaps, and dimensions of the MFTS. This approach allows adapting the proposed alternator to the different load requirements, optimized for power banks and bicycle electronics.

The proposed technical solution has good prospects for use as a power source for charging bicycle electronic devices. It has been shown that for such generators, OMC can be manufactured using a waste-free strip production technology. This technology also significantly reduces input costs and simplifies the manufacturing process.

ACKNOWLEDGEMENTS

The research has been supported by the ERDF project "Environmentally Friendly Small Power Generator with the Rotor Linear Motion (DrauGen)" No. 1.1.1.1/18/A/125.

REFERENCES

1. Torkaman, H., Ghaheri, A., & Keyhani, A. (2019). Axial Flux Switched Reluctance Machines: A Comprehensive Review Of Design And Topologies. IET Electr. Power Appl., 13 (3), 310–321.
2. Radwan-Pragłowska, N., Wegiel, T., & Borkowsk, D. (2020). Modelling of Axial Flux Permanent Magnet Generators. *Energies, 13* (5741), 1–28.
3. Spooner, E., Tavner, P., Mueller, M.A., Brooking, P.R.M., & Baker, N.J. (2004). Vernier Hybrid Machines for Compact Drive Applications. In: *Second International Conference on Power Electronics, Machines and Drives (PEMD 2004)*, (pp. 452–457), 31 March–2 April 2004, Edinburgh, UK.
4. Raihan, M.A.H., Baker, N.J., Smith, K.J, & Almoraya A.A. (2018). Development of Low Translator Mass Linear Vernier Machine for Wave Energy Power Take Off. In: *The 7th International Conference on Renewable Power Generation*, (pp. 1–5), 26–27 September 2018, DTU, Lyngby, Copenhagen, Denmark.
5. Rauch, S.R., & Johnson, L.J. (1955). Design Principles of Flux Switch Alternators. *IEE Trans Power Apparatus and Systems, Part III, 74* (3), 1261–1268.
6. Kwon, J.W., Lee, J.H., Zhao, W., & Kwon, B.I. (2018). Flux-Switching Permanent Magnet Machine with Phase-Group Concentrated-Coil Windings and Cogging Torque Reduction Technique. *Energies*, *11* (2758), 1–11.

7. Diab, H., Amara, Y., & Barakat, G. (2020). Open Circuit Performance of Axial Air Gap Flux Switching Permanent Magnet Synchronous Machine for Wind Energy Conversion: Modeling and Experimental Study. *Energies, MDPI. Open Access Journal*, *13* (4), 1–19.
8. Zhu, Z.Q., & Chen, J.T. (2010). Advanced Flux-Switching Permanent Magnet Brushless Machines. *IEEETrans. Magn., 46*, 1447–1453.
9. Andrada, P., & Martínez, F. (2016). Flux Switching Alternators for Small Wind Generation. *Renew*. *Energy Power Qual. J., 1*, 67–68.
10. Wilfried, S. (1994). *Hub Generator, Especially for Bicycles*. Patent EP0591724A1.
11. Bridgestone Cycle Co. (1995). *Hub Generator for Bicycle*. Patent JPH0710057A.
12. Shimano KK. (2003). *Claw-Pole Generator and Hub Dynamo for Bicycle*. Patent JP2003333777A.
13. Bezrukovs, V., Bezrukovs, Vl., Bezrukovs, D., Konuhova, M., & Berzins, A. (2020). *Magnetic Flux Switching Type Permanent Magnet Generator*. Patent LV15501.
14. Bezrukovs V., Bezrukovs Vl., Bezrukovs D., Konuhova M., Berzins A. (2022): *Magnetic flux switching type permanent magnet generator*. EP3955439A1·2022-02-16.
15. Bezrukovs, V., Bezrukovs, Vl., Bezrukovs, D., Konuhova, M., Berzins, A., & Trokss, J. (2022). Magnetic Flux Switching Type Permanent Magnet Generator for Bicycles: Modelling and an Experimental Study. *Latvian Journal of Physics and Technical Sciences, 3* (59), 48-57.
16. Bezrukovs, V., Bezrukovs, Vl., Konuhova, M., Bezrukovs, D., & Berzins, A. (2022). Axial Flux Switching Permanent Magnet Alternator with External Magnetic Cores. *Latvian Journal of Physics and Technical Sciences, 3* (59), 58-68.
17. Dombur, L. (1984). *Axial Inductor Machines*. Riga: Zinatne, 257.

LATVIAN JOURNAL OF PHYSICS
AND TECHNICAL SCIENCES
2022, N 3

DOI: 10.2478/lpts-2022-0027

ARTIFICIAL INTELLIGENCE MEETS RADIO ASTRONOMY

G. Tuccari[1]*, G. G. Tuccari[2]

[1] National Institute for Astrophysics, Institute of Radioastronomy,
via Piero Gobetti 101, Bologna, IT-40129, ITALY,
Max Planck Institute for Radio Astronomy,
Auf de Hugel 69, D-53121, GERMANY
[2] HAT-Lab srl and Third House Technologies srl
via Milano 97, I-95127 Catania, ITALY
*e-mail: tuccari@mpifr-bonn.mpg.de

Artificial intelligence is widely spreading in all modern technologies. Such a very powerful methodology can have important applications in radio astronomy technology, for instance, in the new DBBC4 VLBI backend development project and in the low frequency array AntArr under development on the Etna slopes in Italy.

In the present paper, we describe the method currently adopted for those projects and some possible applications, which could provide substantial new features in this decade to the radio astronomy science and technology.

Keywords: *Artificial intelligence, DBBC, radio astronomy, radio interference.*

1. INTRODUCTION

When programmable computers were widely deployed, people were curious to know whether these machines might behave as intelligently as humans. Today, artificial intelligence (AI) is a field with many practical applications and active research topics. We look to intelligent software to automate routine labour, understand speech or images, make diagnoses in medicine and support basic scientific research in any field.

The main ability of a computer is to solve problems which are intellectually difficult for human beings but relatively straightforward for a programmed calculator when the problem to be solved can be described by a list of formal, mathematical rules. The challenge for artificial intelligence is solving tasks that are easy for people to carry out but hard for programmers to describe formally, those problems that humans solve intuitively, like recognising spoken words or faces.

The approach is to permit computers to learn from experience and understand the world in terms of a hierarchy of concepts, with each concept defined in terms of its relation to simpler concepts. Getting knowledge from such experience avoids the need for humans to formally specify all of the knowledge that the computer requires to perform a task. Building a hierarchy of rules allows the computer to learn complicated relations formed by simpler intellectual relations. The knowledge is formed by levels, or layers, whose depth is related to the complexity of the hierarchy. This is in some way why it is called AI Deep Learning (DL) and can be considered equivalent to the alternative naming convention Artificial Neural Network (ANN).

AI can make use of a variety of tools nowadays available mature enough to be adopted in the many scientific fields where it was not traditionally adopted. Such tools include software solutions with languages already widely used in scientific work, and hardware platforms which are every day offered from the main manufacturer to operate as computer accelerators, then operating as a central unit or at the edge between sensors and calculation phase. A number of hardware solutions permit the operation in real time, opening a wide spectrum of possible applications.

AI in radio astronomy is today of great interest and investigation by several groups around the globe for a number of tasks, such as radio object classification, pulsar detection, complex network of telescopes control, RFI mitigation, Fast Radio Burst detection (FRSB), radio anomaly detection.

The application of AI methods and techniques could help find solutions to a more severe problem of radio interference mitigation. Radio observations are affected by the strong contribution of terrestrial human activities at any frequency observed in radio astronomy, even in those bands which have been more immune until now. Telecommunications with the high demand for broadband connections are limiting the possibility to detect the many orders of magnitude lower cosmic signals.

On such themes we concentrated the first applications in the development of the suitable techniques to be applied to the ‘AntArr’ and ‘DBBC4’ projects, because both of them could get a great benefit from them. In the paper, we describe two methods under development which provided promising results. Such methods are operated on a hardware platform running in real time and can find applications in different environments or instruments apart from those which we developed them for.

2. AI CONCEPTS

In order to simplify the description of the methods used in this paper we would like to recall some basic AI concepts and this could start by the main comparison between a traditional mode to use a computer through a fixed defined program to perform a task and, as a completely different approach providing the ability, making use of dedicated techniques, to allow the computer to acquire its own knowledge in order to be able to perform that task. Such a level of capability is what is meant when we talk about Machine Learning [1].

There are a number of learning algorithms depending on the task to be handled, and still depending on the algorithm to be adopted a fundamental importance is to be associated with the learning data type. The proper selection of a dataset to be used to get the machine actually able to learn makes a relevant difference in terms of simplification and efficiency.

Deep learning solves the problem of data representation to be used for learning making use of rules that are expressed in terms of other simpler data formats.

As stated above, deep learning allows the computer to relate complex concepts out of simpler concepts. A fundamental deep learning model is the feedforward deep network or 'multilayer perceptron'. A multilayer perceptron is just a mathematical function relating some set of input values to output values. This function is formed by composing many simpler functions.

A complex task could often be divided into more simple tasks and so deep learning resolves this difficulty by dividing the desired complicated task into more affordable nested tasks, each described by a different layer of the model [2]. The input is presented at the visible layer, so named because it contains the variables that we are able to provide to the network, then a series of hidden layers extract increasingly abstract features. These layers are called "hidden" because their values are not known or visible in the given data: the model has to determine what is useful to determine the relationships in the delivered data.

Deep learning is a specific kind of machine learning making use of a learning algorithm. In our development, we considered the linear regression algorithm. The challenge for a regression ANN is to be able starting from the training data to find patterns that generalize to new data. Often machine learning algorithms have settings called hyperparameters that must be determined external to the learning algorithm itself and so we could require it to make use of such additional parameters. Machine learning in such a sense is essentially a form of applied statistics on the use of computers to estimate complicated functions.

A machine learning algorithm is an algorithm that is able to learn from data. For a regression task the computer program is asked to predict a numerical set of values given some input. In order to solve this task, the learning algorithm is asked to provide a function, which is similar to classification, except that the format of output is different. A large experience and applications have been gained in the field of ANN classification and so we could even make use of such experience for our applications.

Convolutional neural networks (CNN) are a specialized kind of neural network for processing data that are organised in a grid-like topology. Those can include time-series data, which can be thought of as a 1D vector reporting samples at regular time intervals or a 2D matrix when more than a single set of time series samples is considered, like those received by a linear array of antennas, or still image data, which can be thought of as a 2D matrix of pixels. Convolutional networks have been widely used in practical applications and their name indicates that the network employs some sort of convolution mathematical operation. Convolution is a type of linear operation, so convolutional networks are simply neural networks that use convolution in place of general matrix multiplication in at least one of their layers.

In general, the convolution is an operation on two functions of a real valued argument. Typical convolutional neural networks do make use of further specializations in order to deal with large inputs efficiently, but these are not always strictly necessary from a theoretical perspective, but can be much more efficient. In our development, we make use of preprocessing before the convolutional layer in order to accommodate a large set of data in a more compact matrix.

3. EXPERIMENTAL APPLICATIONS

We describe here two applications of AI to radio astronomy activities and the two methods which can be applied to both applications. For sake of simplicity, in the description we associate to each application one of the two methods.

AntArr is a low frequency (main 327 MHz, broad range 10 – 1500 MHz) antenna array project under development on the Etna volcano slopes in support of VLBI studies, entirely financed by the INAF (National Institute for Astrophysics) spin-off HAT-Lab srl, a company developing and manufacturing VLBI backend systems, which are widely adopted in the VLBI community for astronomy, geodetic and space science radio astronomy observations.

RFI for such an antenna array is an important limitation in particular at low frequencies where the synthesized beam of the antenna array easily detects the strong radio interference emissions from the array side lobes.

An antenna array consists of two or more antenna elements that are spatially arranged and electrically interconnected to produce a directional radiation pattern. The interconnection between elements can provide a fixed phase (or delay for broadband applications) to each element and then can form a phased array. In optimum and adaptive beamforming [3], the phases and the amplitudes of the feed network are adjusted to optimize the received signal.

The geometry of an array and the patterns, orientations, and polarizations of the elements influence the performance of the array. Adaptive beamforming (Fig. 1) has been considered in order to make use of the null steering toward the worst case RFI directions with the aim to mitigate their effect in quasi-real time. Antenna arrays using adaptive beamforming techniques can reject interfering signals having a direction of arrival different from that of a desired signal.

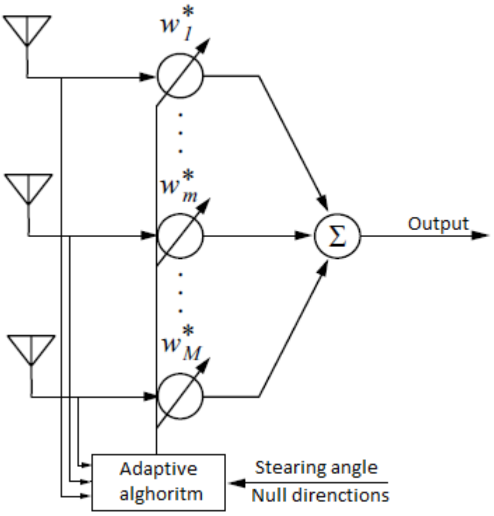

Fig. 1. The schematic functionality view of an adaptive antenna array.

A number of adaptive algorithms [4] have been considered and their latency time has been evaluated with their implementation in a computer software based platform: Direct Matrix Inversion (DMI), Least Mean Squares (LMS), Recursive Least Squares (RLS), Linear Constraint Minimum Variance (LCMV), and Minimum Variance Distortionless Response (MVDR) [5]. All of them are data dependent, so require observed data samples to converge, and computationally complex to operate in a real-time environment, but one of them is widely adopted for its good convergence and ability to deal with a number of interference sources at the same time.

In order to evaluate performance and latency time, a linear array of 8 antennas (Fig. 2) has been considered with the support of a real-time RFI direction tracker, which is a set of antennas independent of the array performing as a complex detector to determine the RFI levels and their angular position. This permits to have in real time the knowledge of the worst case RFI presence and direction of origin information to be used for the mitigation algorithm.

A preliminary simulation has been realised by considering the 8-element linear array with a collection of data received by each of the array element when the main beam of this array is pointing to a desired collection of sources in the sky with the constraint to minimize the RFI contribution, making use of the selected adaptive array beamforming algorithm.

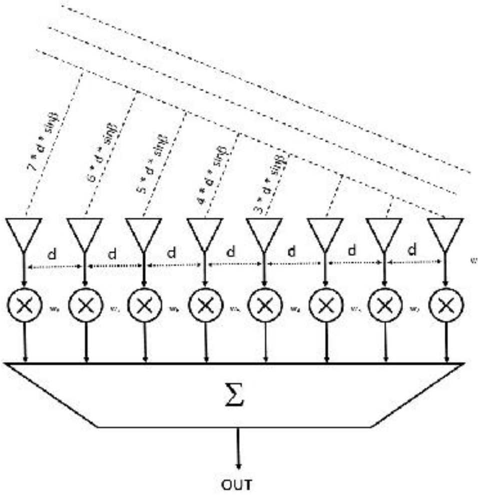

Fig. 2. Conceptual view of a linear 8-element antenna array.

The simulation evidenced a large latency in the calculation, which would not be practical for real-time implementation and then a DNN was considered as a candidate to accomplish the mitigation functionality with the aim to achieve a much lower latency when realised on a hardware platform. On the other hand, we need to take into account that the hardware platform makes use of SoC (System on Chip) programmable devices, which have large part of their functionality realized through very high performance programmable logic (FPGA) with support of efficient on chip processors, so the overall functionality can be shared between such parts to obtain optimized performance in terms of utilised resources and latency. The direct implementation of the adaptive beamforming algorithm MVDR is not efficient for its mathematical complexity to be performed by a FPGA architecture while very different and convenient can be to perform the functionality making use of a DNN (Deep Neural Network) which was then considered and evaluated to perform such a task to mitigate the RFI contribution for the antenna array.

A simulation study has been performed with a large variety of DNN topologies in order to determine a suitable architecture in terms of dimension and number of layers. The neural network under evaluation has been trained with a very wide dataset ranging on a broad range of steering directions (main beam in the source direction) and unwanted RFI directions where the signals needed to be attenuated. All the DNN considered had the constraint to be deployable on a hardware FPGA SoC platform so to be able to operate in real time.

We need to recall that the AntArr project [6], [7] under realization is a bi-dimensional uniformly spaced phased array with amplitude and phase in the single element which can be controlled before its contribution to the array. The beamforming is realized by an adaptive network whose goal is to optimise the SNR in the direction of the pointing where the source is to be observed, minimising the sidelobe contribution in the interference worst case directions. Those directions are determined in real time using a complex (I-Q) RFI antenna configuration. Then the simulated study determines the condition for the real-time network operations, so that a pre-trained network can be adopted to 'draw' an optimized antenna array final beam with an appropriate main beam and sidelobes.

Training with real data will be implemented in far-field regime (> 5 km) making use of a campaign of observations with real RFI and array orientation rotating with respect to the zenith and in near-field regime (< 500 m) making use of weak transmitters on board of a small drone positioned in a variety of positions in the sky above the network.

The simulated training was implemented on a dedicated software platform making use of last generation powerful GPUs performing high-end performance parallel calculation.

The selected trained network showing the best performance was implemented in the hardware platform making use of SoC devices, where the network was synthesized in maximum part in FPGA (hardware) and for the rest in software running inside processors part of the SoC device for real-time performance. The finalized trained network will be tested in a monodimensional AntArr version (one arm) before extending the functionality to the entire array. Figure 3 schematically shows this process.

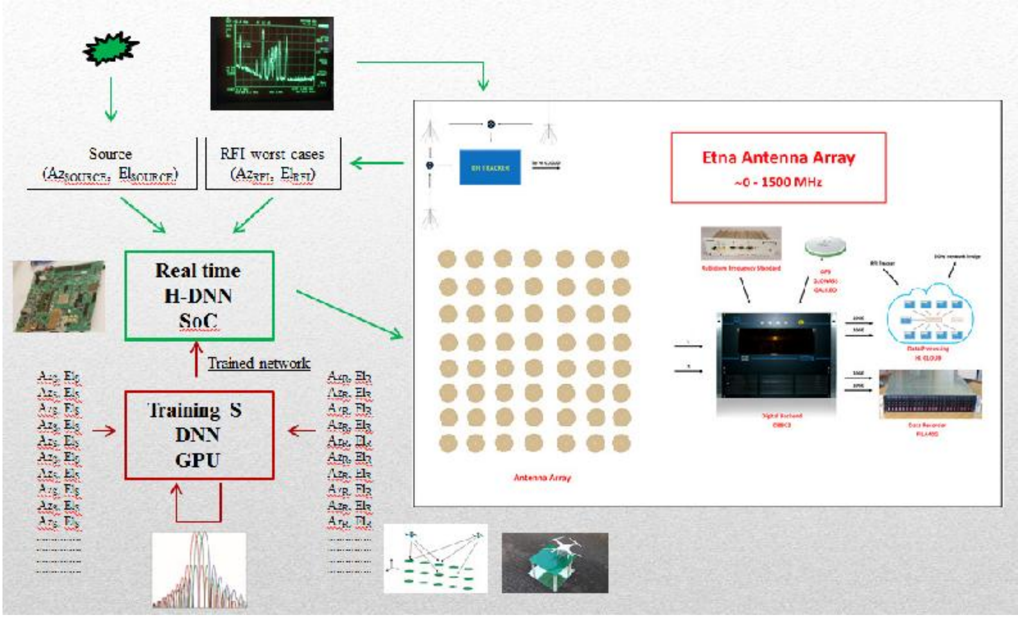

Fig. 3. DNN implementation in AntArr.

The second application we describe is related to the development of the DBBC4 backend. The DBBC4 is a new project for the latest generation of the DBBC VLBI backend family. The project started at the end of 2021. It will last four years. Figure 4 shows the schematic functionality of the system [8].

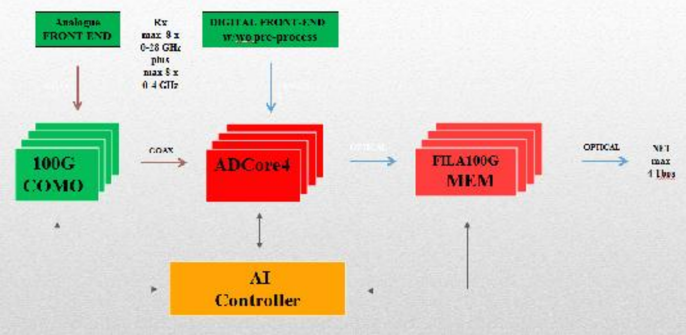

Fig. 4. DBBC4 schematic view.

This new backed system for VLBI observations has the following target performance:

- Input bandwidth up to:

8 x 28 GHz = 224 GHz aggregate in digital front- or backend

plus 8 x 4 GHz = 32 GHz aggregate in ancillary digital frontend

Total full aggregate = 256 GHz

- Output data rate up to: 1 Tbps @ 2-bit, 2 Tbps @ 4-bit, 4 Tbps @ 8-bit
- Modes: DSC (full band for data transfer), OCT (wide bands), DDC (tuneable narrow bands)
- Additional functionalities: Burst-mode, AI-mode, Net-to-Memory/Disk capability
- Compatibility with previous DBBC generations
- New concept with legacy features (DBBC2, DBBC3)
- New functionalities at the current state of the art technology
- Applications: BRAND, EHT, ngEHT, EVN, IVS etc.

The system includes for the first time in a VLBI backend an AI dedicated hardware module (A-EYE) for implementing embedded artificial intelligence functionalities.

Figure 5 shows the evolution of the DBBC family systems where one can see how in two decades the input bandwidth has been increased 500 times (from 512 MHz to 256 GHz) and the output data rate 4000 times (from 1 Gbps to 4 Tbps).

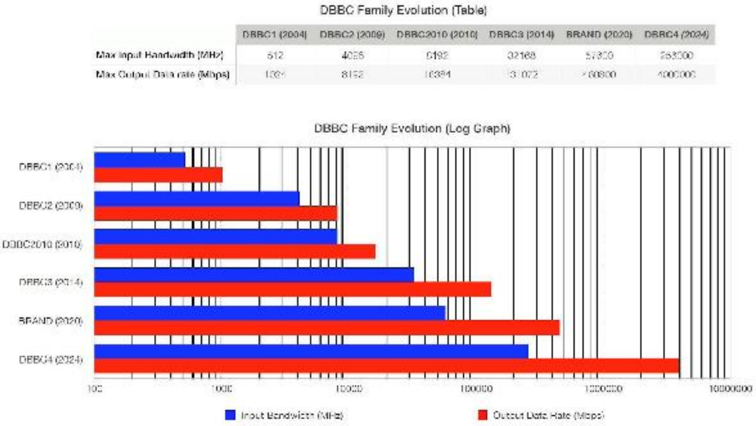
DBBC Family Evolution (Table)

	DBBC1 (2004)	DBBC2 (2009)	DBBC2010 (2010)	DBBC3 (2014)	BRAND (2020)	DBBC4 (2024)
Max Input Bandwidth (MHz)	512	4096	8192	32768	57300	256000
Max Output Data rate (Mbps)	1024	8192	16384	131072	>60800	4000000

Fig. 5. DBBC family evolution in the input bandwidth and data rate.

There are a number of planned AI implementations in the DBBC4 and the first one is aimed at mitigating the RFI effects on the observed VLBI data. More applications are defined and will be introduced during the project development.

An adaptive network is adopted whose goal is to optimise the SNR in presence of impulsive or periodic RFI. A pre-trained DNN is used with the duty to recognise the presence of impulsive or periodic RFI in the observed noise and to act as a trigger to operate modifications to such data, which are expected to improve the SNR.

A simulation run similarly to what described for the AntArr project is underway and will be the object of a dedicated paper. The best network architecture determined through simulation will be used for the implementation to be done in real time.

Training is carried out by evaluating a large number of pre-trained commercial DNN on a dedicated software platform making use of last generation powerful GPUs performing close to real-time performance.

The selected trained network showing the best performance has been implemented in a hardware platform making use of SoC devices, where the network is synthesized in maximum part in FPGA and for the rest in software for real-time performance.

The on-field training is planned to be implemented in far-field regime (> 5 km) with a campaign of observations with real RFI and in near-field regime (< 500 m) making use of weak transmitters on board of a commercial drone positioned in a variety of positions in the sky.

The finalized trained network after having been tested in simulation and in single dish regime will be tested in VLBI observations. Figure 6 shows a schematic view of this process.

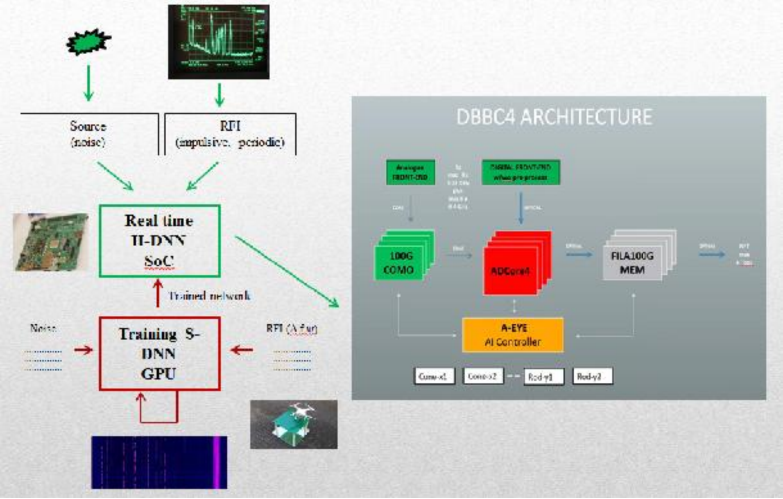

Fig. 6. DNN implementation in DBBC4.

4. RESULTS AND DISCUSSION

We discuss here the results of the simulations performed in the AntArr case, which, as already indicated, are valid and can be even applied to the DBBC4 implementation. In particular, this can find applications to the development of PAF (Phased

Array Feed) compatible with the AI Controller (A-Eye).

Results for the case described in the DBBC4 section will be reported in a different paper, but similarly to the previously indicated results even this solution is applicable to the AntArr implementation.

Initial constraints in the neural network topology and dimensions have been set in order to be able to fit what was developed in the hardware platform used for the simulations (Xilinx Zynq UltraScale+ MPSoC ZCU102) [9], [10]. Such choice involves limitations for the specific device, but offers also the opportunity to evaluate the resources required to perform the planned activities. The board used is considered sufficient for the tasks we tested and can be used as a base for any further development. The board consists of a 16 nm XCZU9EG MPSoC (Multiprocessing Platform System on Chip) device with 1156 pins, 600K logic cells, 32 Mb memory, 2520 DSP slices. On the board, there is a variety of interfaces, 4GB 64-bit DDR4 and 512MB 16-bit DDR4 RAM modules in support of the internal processors (a quad-core Arm® Cortex®-A53, a dual-core Cortex-R5F real-time processors, and a Mali™-400 MP2 GPU). Figure 7 shows the architecture of the SoC device. We used such a device for the simulation and on-field testing, but the final configuration for the application will be selected at a later stage.

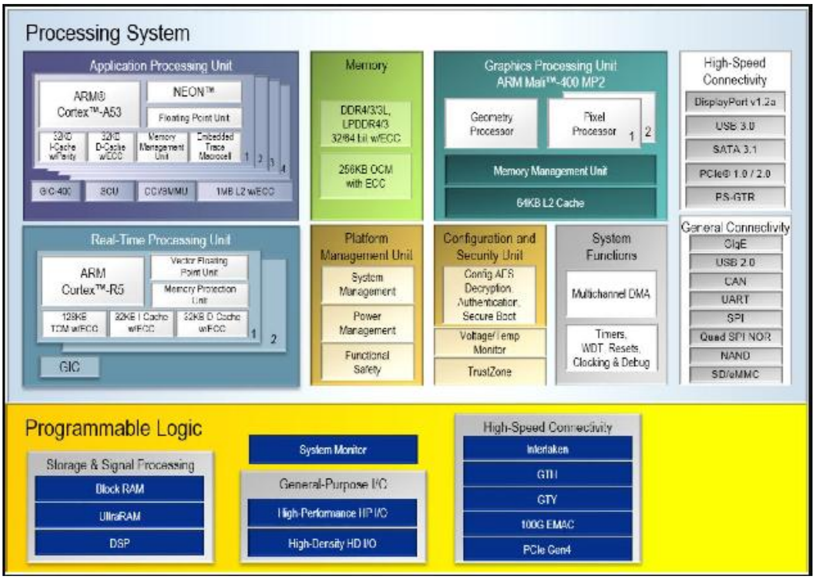

Fig. 7. Architecture of the SoC device used in this application.

A large number of DNN types have been evaluated considering layer type and number of elements per layer. The procedure will be described in detail in a separate document because of a large number of partial results related to different topologies which could be of interest to other developers. Dataset creation for training, validation and test was also the object of a large number of implementations, which deserved additional considerations to be reported. A particular care was found to be required in the data pre-processing to be provided as input dataset. It should be taken into account as the network in order to implement the functionality requires to be aware of the sampled data received by the antennas in the array. Such a number of data would imply an internal to the network capacity to handle sequences of time sampled data, which could be not practical when the period of samples required could be long (in our case 10^5 for each antenna). This suggested preprocessing the data so to have a fixed number of elements as input to the network in spite of the number of samples used. Several methods were tested and in the end a cross-correlation matrix was adopted.

A number of routines was generated in order to: a) create the dataset for the training, for the validation and for the network test; b) calculate the performance of the original adaptive array to be compared with the network under test in terms of SNR (signal level at the main lobe direction with respect to the RFI suppression at the null direction) for training, validation and test set; c) generate what was required to compile and upload the network on the hardware platform and to test the performance in terms of latency with respect to the network running on the simulation computer; d) generate array beam plot and histograms to evaluate the results.

The network which will be used for the real data application is still not fully determined in the number of additional to the first hidden layers. The architecture shown in Fig. 8 is the one providing the best results in simulation which are reported here and so will be used as a base structure for real-time implementation.

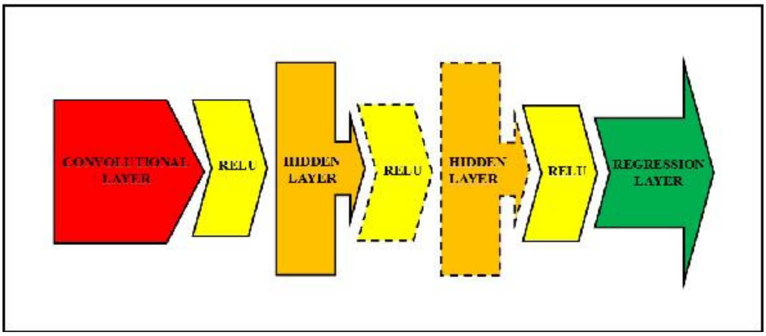

Fig. 8. DNN architecture used for the application.

The training phases have been implemented with many datasets, varying the number of samples in time, array angles of steering, RFI directions. Each network was tested during the training with a validation dataset and finally with a wide test set.

Figure 9 shows a representative result: two array patterns, the lower one as a result of the algorithm adopted for the training (MVDR) and the upper one coming from a validation set. It can be seen that the network fits very well the adaptive array beam, providing excellent behaviours in terms of gain of the steering direction and deep attenuation in the RFI direction. The general testing behaviour for a complete running set of 30000 input dataset elements is shown in the histogram of Fig. 10: the values of attenuation in the RFI direction with respect to the main beam where the array is pointing. It can be seen that the average discrimination is in the order of 42 dB, similar to the adaptive algorithm used as a base for training.

In order to perform valid training and get good performance from the network, the power of the RFI should be kept at the same order of magnitude of the operative conditions. In presence of better RFI level conditions, the network will improve or behave as expected with the training, while when subject to worse or greatly worse conditions the network will still be able to operate even if with gradually worse capacity to properly predict and mitigate the RFI. Figure 11 shows the network prediction degradation, which affects the network learning when the interference power increases with respect to the level used for the training as calculated by simulation introducing different RFI noise conditions. We need to point out that this degradation is related to the training process goodness and not to the behaviour of the network when trained and properly adopted for the expected RFI noise level.

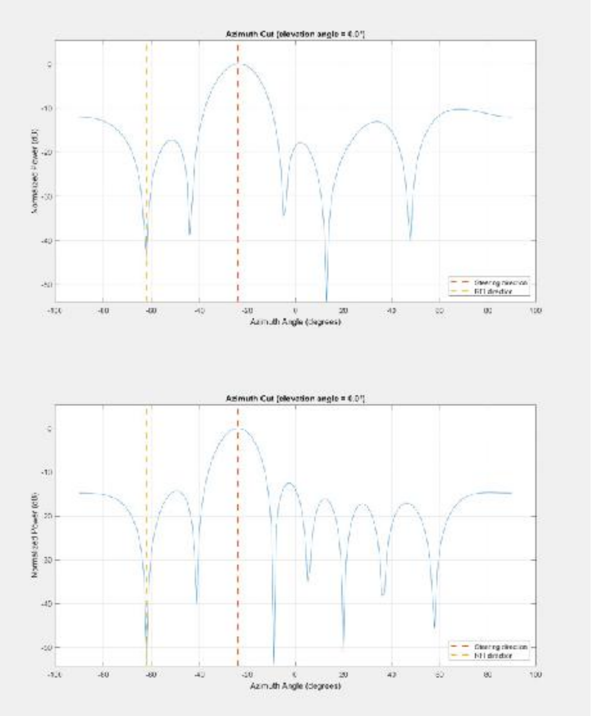

Fig. 9. Array pattern comparison between adaptive algorithm (lower) and DNN (upper).

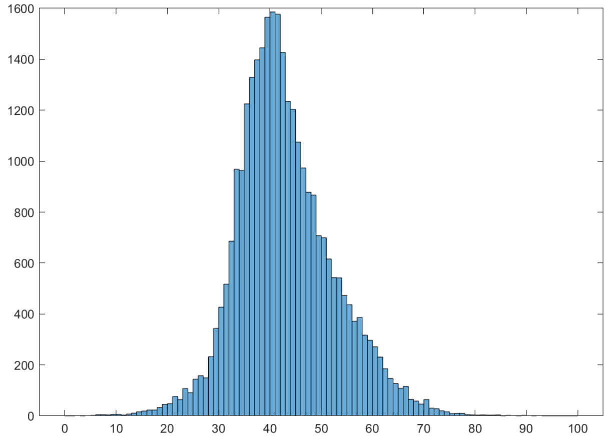

Fig. 10. Attenuation (dB) in the RFI direction with respect to the main beam in a test set of 30000 different cases.

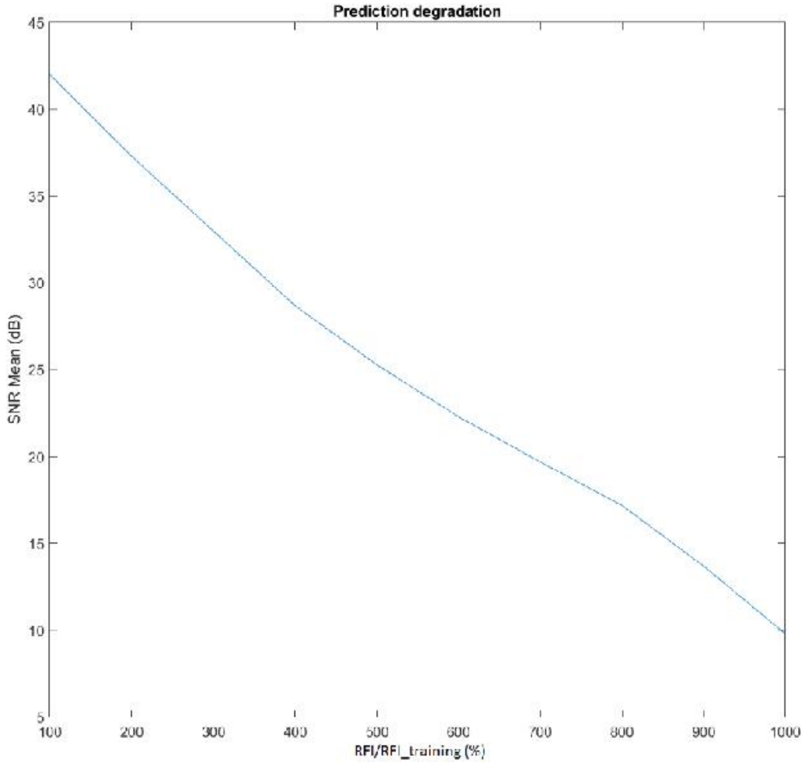

Fig. 11. Network prediction degradation as a function of the RFI increment with respect to the level adopted during the training.

Finally, the latency in the prediction was estimated for the implementation of the convolutional network in the hardware platform in comparison with its implementation in a pure software version. This evaluation for the comparison was done in PC platforms, even of a high level. The table reports the results showing that the implementation in MPSoC is very efficient, able to perform a large number of corrections per second (e.g., for tracking a moving RFI source) with very good RFI attenuation values, comparable with the mathematical adaptive algorithm whose implementation is poorly efficient in the MPSoC platform. This solution is also very convenient in terms of power requirement, which is a valuable feature for a system having to operate continuously.

Table 1 provides the latency times for a standard last generation PC, high-end last generation PC and MPSoc adopted solution. It can be seen that with the adopted DNN the latency time is about twenty times faster in the hardware platform, with the use of a fraction of its available resources, with respect to the PC purely software calculation and this allows performing more than 330 predictions per second implemented in a very dimensionally small device easily integrable to any hardware platform. It is worth noting that the results obtained are related to the analysed linear array, which can be extended to a longer and even bi-dimensional array with increased dimension of the convolutional network. The latency with a higher number of elements and dimensions is not expected to increase proportionally due to the network computation massively parallel.

Table 1. Latency Times for a Standard Last Generation PC, High-End Last Generation PC and the MPSoc Solution

Platform	Processor	Frequency	Latency (ms)	Predictions/s
PC only software	INTEL CORE I7 8665U	2.1 GHz	65	15.4
PC only software	AMD Ryzen Threadripper 3970X	4.0 GHz	54	18.5
MPSoC mainly hardware, in part software	XILINX XCZU9EG MPSoC	220 MHz	3	333.3

5. CONCLUSIONS AND FUTURE ACTIVITIES

The use of artificial intelligence applications is nowadays possible with real-time performance for the presence on the market of technologies, which greatly simplify the implementation and permit to obtain very valuable solutions to problems we could not imagine to easily handle even ten years ago. We have presented two possible applications to the radio astronomy technology placing an emphasis on one of them. The activity described in the mentioned applications has placed the base for real-time implementation after having used simulated data to study a class of deep neural networks with many different architectures in order to determine a possible best one for on-field applications. The method to be adopted even for such a step with not simulated data has been described; a detailed description of the results has not been the aim of this paper and will be the object of another report.

The second type of application has been mentioned, which is under development in parallel with the one described. In this case, instead of dealing with RFI mitigation applied to the space domain, this one operates in the time domain to mitigate impulsive periodic or non-periodic RFI.

Similar to the first application, the basic concept required for the implementation of the appropriate dataset for simulation, study and selection of the DNN class and architecture to be adopted has been described. Further step which will follow for implementation on field in real time has been illustrated. Still with similar results, the successful implementation of such development on MPSoC has been carried out. Results of the second application will be described in another paper.

This activity is well far to be completed because the field it covers is a huge opportunity for implementations and improvements to be achieved in more complex radio astronomy observations from the earth surface due to the increasing RFI pollution. On the other hand, AI is a very promising tool to cover many other aspects of the radio astronomy observations, which provides additional opportunities to this branch of science.

REFERENCES

1. Goodfellow, I., Bengio, Y., & Courville, A. (2006). *Deep Learning*. MIT Press.
2. Hirose, A. (2012). *Complex-Valued Neural Networks* (2nd ed.). Berlin: Springer.

3. Delos, P., Broughton, B., & Kraft, J. (2020). *Phased Array Antenna Patterns (Part 1, 2, 3), Analog Devices*. Technical Report.
4. Mailloux, R. (2005). *Phased Array Antenna Handbook* (2nd ed.). UK: Artech House.
5. Li, D., Yin, Q., Mu, P., & Guo, W. (2011). Robust MVDR Beamforming Using the DOA Matrix Decomposition. *IEEE-ISAS*, 105–110.
6. Tuccari, G., Alef, W., Buttaccio, S., Tornatore, V., & Wunderlich, M. (2014). DBBC3: AntArr Project. In *12th European VLBI Network Symposium and User Meeting*, 7–10 October 2014, Cagliari, Italy.
7. Tuccari, G., Wunderlich, M., Dornbusch, S., Tuccari, G.G. (2020). ANTARR, Etna Low frequency Antenna Array. *Latvian Journal of Physics and Technical Sciences, 1*, 6–12. doi: 10.2478/lpts-2020-0001
8. Tuccari, G. (2021). DBBC4 Project. *HAT-Lab Internal Report Series, 13*.
9. Xilinx. (n.d.). *Scalable Portfolio of Adaptable MPSoCs*. Available at https://www.xilinx.com/products/silicon-devices/soc/zynq-ultrascale-mpsoc.html
10. Zynq UltraScale+ MPSoC: Embedded Design Tutorial. *A Hands-On Guide to Effective Embedded System Design UG1209* (v2020.1). Available at https://dokumen.tips/documents/zynq-ultrascale-mpsoc-embedded-design-tutorial-chapter-1-introduction-ug1209.html

LATVIAN JOURNAL OF PHYSICS
AND TECHNICAL SCIENCES
2022, N 3

DOI: 10.2478/lpts-2022-0028

HYDROGEN HYDRAULIC COMPRESSION SYSTEM FOR REFUELLING STATIONS

V. Bezrukovs, Vl. Bezrukovs*, M. Konuhova, D. Bezrukovs, A. Berzins

Engineering Research Institute
“Ventspils International Radio Astronomy Centre”,
Ventspils University of Applied Sciences,
101 Inzenieru Str., Ventspils, LV-3601, LATVIA
*e-mail: vladislavsb@venta.lv

The article investigates the properties and potential of compressed hydrogen as one of the most promising energy carriers in order to facilitate the development of energy storage capabilities and lay down a stable foundation for the future of a sustainable energy sector. The study considers the use of hydrogen, compressed at high pressure from 50 MPa to 100 MPa, at refuelling stations to supply electric cars. The technical properties of modern hydraulic compressors used for hydrogen accumulation in high pressure buffer containers are considered. The study shows that the design of hydraulic compressors in terms of their technical characteristics optimally corresponds to the primary requirements for their use as booster compressors at refuelling stations. The authors conclude with the proposal of an enhanced design of the hydraulic compressor with the use of fluid flow counters in a control system of a hydrogen compression cycle. The proposed technical solution provides for continuous monitoring of the hydrogen compression process that increases the reliability of control system operation.

Keywords: *Energy storage, fluid flow counters, hydrogen, high pressure, hydraulic compressors, refuelling stations.*

1. INTRODUCTION

Currently, European countries are focused on finding the ways of increasing the share of hydrogen energy in their energy balance, driven by the desire to reduce consumption and dependency on fossil fuels. Hydrogen has the potential of making a significant contribution to the three most important tasks concerning the energy use: to achieve sustainable economic development of the European Union, reduce greenhouse gas emissions and improve air quality [1], [2].

In recent years, the use of hydrogen energy in transport and the concept of a hydrogen economy have benefited from a new wave of strong political support. At the same time, rapidly evolving technologies have increased the feasibility of using hydrogen as a driver for the future carbon-neutral energy system. At the heart of this initiative, there is the desire for energy security and independence. At the same time, the European Union has set an ambitious goal to become the first climate neutral continent by 2050, which is in line with the guidelines of the European Commission [3].

John Moore, the CEO of Bloomberg New Energy Finance (BNEF), at the Asian Clean Energy Summit on 30 October 2021 in Singapore made a prediction that by 2030, green-hydrogen with the price of just over \$2/kg would start competing with coal and natural gas as an energy carrier in steel production, and by 2050, at \$1/kg it would become more profitable than gas in the world markets and compete with the cheapest coal, keeping CO_2 emission at zero. In his opinion, due to hydrogen there will be a kind of final electrification of the world industry [4].

In the real-life environment, hydrogen production can be organised by using a wide range of technologies. Depending on the production method, hydrogen is conventionally labelled green, blue, pink and grey, and specialised terms - safe, sustainable, low-carbon and pure - are also used [5]. Hydrogen, the most widely spread element in the universe, on Earth is found mostly in a bound state. However, the technical capability to produce it by decomposing water with an electric current makes it possible to create and store the reserves of this gas, which has a high energy density and is considered to be an ideal fuel. The utilisation of renewable energy sources, which are practically inexhaustible, for hydrogen generation allows establishing a continuous, sustainable, ecologically clean energy production cycle. Thus, "green" hydrogen is one of the most promising approaches to future energy storage.

Green hydrogen is considered to be the most environmentally friendly and will be an important part of the future 100% sustainable energy system [6]. In the production of green hydrogen, the main emphasis is on the use of wind and solar energy. As a result, a process chain for the production of hydrogen is created by electrolysis of water without emission of carbon dioxide into the atmosphere. Thus, the process of water electrolysis can potentially be carbon free if renewable or nuclear electricity is used [7], [8].

Overall, the development of efficient, cost-effective, competitive and safe technologies for the production and use of hydrogen is the main area of research for the future hydrogen energy industry. The conversion of hydrogen energy into electric current without burning it makes it possible to use this energy source to power the electric vehicles. Currently, there are already examples of successful implementation of hydrogen technology for cars and trucks.[1,2]

2. PROPERTIES OF COMPRESSED HYDROGEN

In general, the cost of hydrogen is determined by the energy cost of its production, but for its widespread use in stationary and mobile systems, a number of issues relating to its storage and transportation should also be addressed [7]. Transportation of gaseous hydrogen is a very expensive operation, because hydrogen density is low, about 0.09 kg/m^3 under standard conditions of temperature and pressure [9]. The density

---

[1] "Volvo AB and Daimler Trucks team up in a hydrogen fuel cell joint venture" (link).

[2] Toyota Mirai 2022 edition (link).

of hydrogen should be increased by compression and accumulated in a reservoir for storage and transportation to its ultimate use location.

The research results presented in [10], [11] allow us to estimate the influence of the compression process on the change of energy properties of hydrogen. Figures 1–3 show how the energy density (kWh/L), stored in compressed hydrogen, depends on temperature and pressure. Analysis of the curves in the temperature range from 20 °C to 80 °C shows that the hydrogen density increases exponentially with increasing pressure and tends to decrease with increasing temperature.

The graphs clearly show that as the pressure increases, the energy density of hydrogen increases almost linearly only up to 80 MPa. A further increase in pressure is not accompanied by an adequate increase in energy density and is impractical. This increases the cost of the equipment used to compress hydrogen, while the performance of the vehicle is not significantly improved.

Derived curves shown in Figs. 1–3 enable us to estimate weight and energy density of compressed hydrogen contained in a typical 145-litre Toyota Mirai[2] tank with 70 MPa and 20 °C. In this case, energy density is 1.28 kW/L and, consequently, the value of hydrogen storage is equal to 185.6, kWh and gas weight is 5.6 kg.

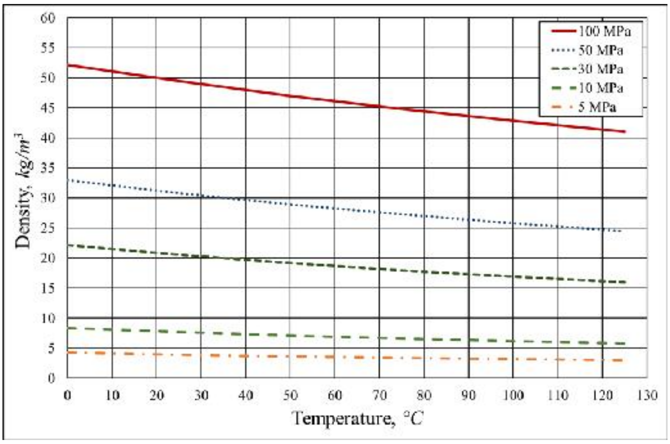

Fig. 1. Hydrogen density as a function of temperature at pressure from 5 MPa to 100 MPa.

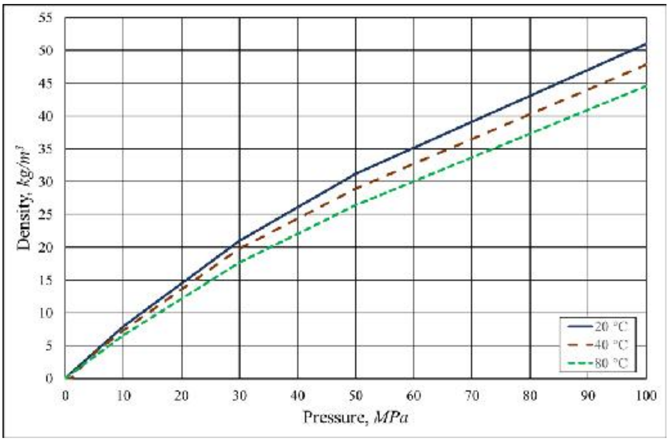

Fig. 2. Hydrogen density as a function of pressure in the interval of temperature from 20 °C to 80 °C.

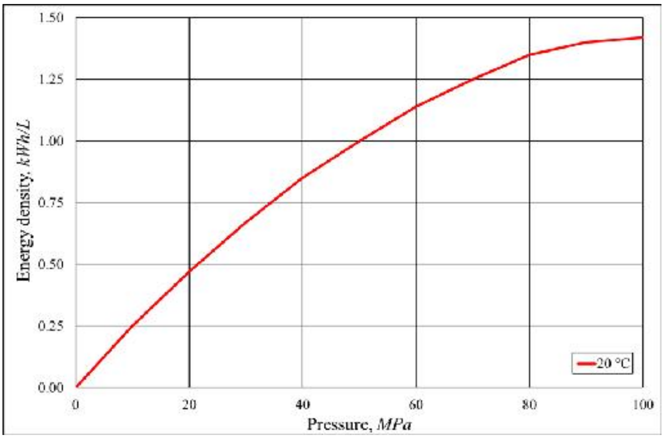

Fig. 3. Energy density of compressed hydrogen as a function of pressure at temperature of 20 ºC.

Pressurised storage of gases, including hydrogen, is a rather mature technology. However, the use of hydrogen tanks in vehicles coupled with the challenge of using very high pressures, requires strict regulations backed up by safety and performance studies.

3. USE OF COMPRESSED HYDROGEN AT REFUELLING STATIONS

In order to use hydrogen at refuelling stations, the necessary infrastructure must be in place to store and prepare the hydrogen for injection into the vehicle fuel tank. For this purpose, hydrogen pressurised at 50 MPa to 100 MPa is used. Accordingly, refuelling stations must be provided with the appropriate equipment, which should only be operated by specially trained personnel [12].

However, due to leakages, the ability to store hydrogen at these high pressures for a long time is limited. Respectively, booster compressor capacities and buffer tanks for high pressure hydrogen must be installed at refuelling stations [13].

Compressed hydrogen is transported by road transport in containerised hydrogen tubes. For example, Linde[3] – a leading industrial gas and engineering company, for this purpose uses trailers shown in Fig. 4.

In practice, large trailers with tank pressures of 25 MPa or less, per tube, with a total hydrogen weight of 560 kg are used for long-term storage and transport; one of its examples is shown in Fig. 5.

Fig. 4. Containerised hydrogen tubes mounted on a trailer for the transport of hydrogen in central Europe (Co. Linde) [14].

---

[3] Linde Engineering. High-performance hydrogen refuelling technologies. (link).

Fig. 5. Example of a large trailer with tank pressure of 25 MPa, per tube, with a total weight of 560 kg of hydrogen [15].

Articles [7], [16] review different contemporary technologies of hydrogen compression, their working principles, advantages and limitations. It should be noted that, from a wide variety of compressors, the ones with a liquid piston have the lowest energy consumption, as only this technology is able to provide a quasi-isothermal compression process.

The liquid piston is not a new concept, as the earliest known application dates back to 1906. This solution was used in an internal combustion engine for pumping water, known as the Humphrey pump [17]. The Humphrey pump followed the Atkinson cycle and demonstrated efficiencies of between 5 % and 10 % [18].

The liquid piston gas compression concept uses a column of liquid to directly compress gas in a fixed volume chamber. The use of a liquid piston eliminates gas leakage from the compression chamber and eliminates the friction of the mechanical sliding seals present in the cylinders of mechanical compressors.

The use of liquid as a piston provides for a significant increase in efficiency of gas compression. Using a simplified model, it has been demonstrated that this concept can increase the compression efficiency from 70 % to over 83 % [19].

It should be pointed out that the gas compression process is accompanied by high heat generation and the temperature of the gas has an effect on the working fluid. In fact, the fluid and the gas are compressed together, but since the fluid has a higher density and a higher heat capacity, the heat generated during compression is effectively absorbed by the fluid and the surrounding walls of the compression chamber.

Once the compression cycle is complete, the heated fluid is moved from the compression chamber to the heat exchanger, where it is cooled. As a result, hydraulic compressors have an advantage over reciprocating compressors in terms of cooling, as there is no need for external heat exchangers on the compression chambers. This reduces the weight of the compressor and the cost of the entire system [7].

Hydrogen compression technology using a hydraulic compressor has been successfully implemented in Linde appliances, which offers fully integrated systems for use in booster compressor stations. For example, the Type IC50/60 Ionic Compressor, with a connected load of 186 kW, produces up to 56 kg/h of hydrogen compressed to 50 MPa and pumps it into a buffer tank. The unit can be operated at ambient operating temperatures of -20 °C / +40 °C, and the inlet pressure to the system can vary from 0.6 MPa to 20 MPa.[4]

4. ALTERNATIVE DESIGN OF HYDRAULIC COMPRESSOR

A schematic diagram of a refuelling station using hydrogen at inlet pressure from 0.6 up to 25 MPa, either brought by trailer or generated by electrolysis at the station

---

[4] IC50/60 Ionic Compressor. Compressor module for gaseous hydrogen refuelling station, datasheet. Linde Engineering (link).

itself, is shown in Fig. 6. The proposed concept is especially attractive when combined with the use of green hydrogen produced by electrolysis, fed from wind turbines, solar panels or the electricity grid. Using the booster hydraulic compressor, the low-pressure hydrogen is raised to the required 70 MPa for cars and 35 MPa for trucks and pumped into the buffer storage tanks. The high-pressure hydrogen is then filled into the vehicle tanks via a dispenser.

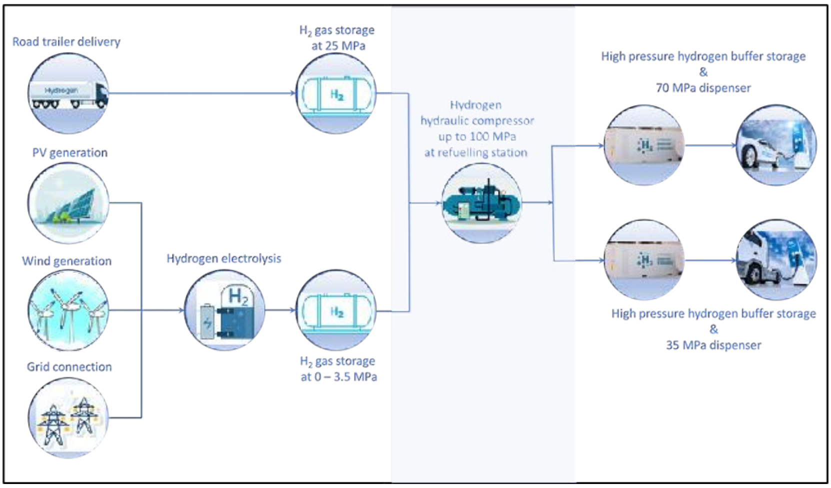

Fig. 6. Schematic diagram of the delivery, storage and preparation of compressed high-pressure hydrogen for use in refuelling stations.

The authors developed an alternative solution of hydraulic compressor design, whose structural scheme is shown in Fig. 7 [20]. It is assumed that the device is designed for use as a booster compressor in a refuelling station system that uses hydrogen brought in by a truck in tubes or produced locally by electrolysis of water in limited quantities. For example, an Enapter electrolyser can produce up to 500 L/h or 1.0785 kg H_2 at 20 °C and 3.5 MPa.[5]

The proposed device contains a tank H_2 for low pressure hydrogen storage, two operating cylinders V_1 and V_2 of the first compression stage, an operating cylinder V_3 of the second compression stage and a buffer cylinder V_4 for high pressure hydrogen storage, connected to each other by pipelines.

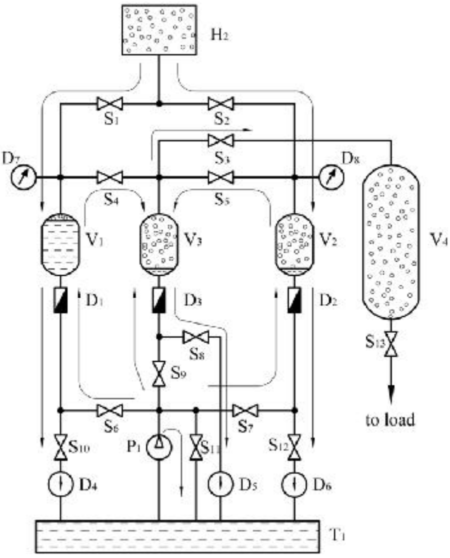

Fig. 7. Schematic diagram of the connection between the working cylinders and the hydrogen tanks in the hydraulic compressor.

---

[5] AEM Electrolyser EL 4.0, datasheet. Enapter (link).

Hydraulic compression system consists of a tank T_1 with working fluid and high-pressure liquid transfer pump P_1, connected by pipelines to the operating cylinders V_1, V_2 and V_3. The level of working fluid in the cylinders and, consequently, the gas compression ratio, is controlled by fluid flow counters D_1, D_2, D_3. The flows of hydrogen and working fluid are switched by the servo-controlled valves S_1 to S_{13}. The optical fluid flow control sensors D_4 – D_6 help control the flow of working fluid in pipelines, while cylinders V_1, V_2 and V_3 are filled with hydrogen. The pressure level in the pipelines is controlled by pressure gauge D_7, D_8.

The arrows in the diagram (Fig. 7) show the direction of flow of working fluid from tank T_1 through pump P_1 and the direction of hydrogen flow from storage H_2 to buffer cylinder V_4 after performing a compression cycle in operating cylinders V_1–V_3.

The valves are switched on according to a specified algorithm, which implements the following cycle of hydraulic compressor operation. At the initial state, all valves are closed, and the pump is switched off. The first step is to open the valve, e.g., S_2, through which hydrogen from tank H_2 enters operating cylinder V_2 and then the S_2 valve is closed.

The next step is to switch on the pump P_1 and open valve S_7, through which working fluid from the tank T_1 flows into the operating cylinder V_2 by pipeline and through the fluid flow counter D_3. The amount of working fluid entering the operating cylinder V_2 is measured by fluid flow counter D_3 and corresponds to a given degree of compression of hydrogen in this cylinder. Simultaneously with this process valve S_1 opens and hydrogen from tank H_2 flows into operating cylinder V_1 and then valve S_1 closes.

When cylinder V_2 has been filled with a certain volume of working fluid, valve S_7 is closed and valves S_5 and S_6 are opened. The compressed hydrogen flows through valve S_5 into operating cylinder V_3 of the second compression stage, at the same time working fluid flows through valve S_6 and fluid flow counter D_1 into operating cylinder V_1, where hydrogen compression occurs. During this time, the transfer of compressed hydrogen from the operating cylinder V_2 to the operating cylinder V_3 is completed, so valve S_5 is closed and valves S_2 and S_{12} are opened.

During this period, hydrogen from tank H_2 through open valve S_2 presses working fluid from operating cylinder V_2 into tank T_1 through fluid flow counter D_2 and optical sensor D_6. At the same time, a certain amount of the working fluid will remain on the walls of the operating cylinder due to its viscosity.

The signal to close valves S_2, S_{12} will come after the optical sensor D_6 has detected that the flow of working fluid in the pipeline has been interrupted. During this cycle, fluid flow counter D_2 operates in reverse mode, which allows determining the volume of fluid remaining in the operating cylinder and dispense working fluid in the next cycle. At the end of the cycle, the operating cylinder V_2 is filled with low pressure hydrogen and prepared for a new compression cycle.

Working cycle of hydrogen compression in operating cylinder V_1 occurs in antiphase with respect to the working cycle of cylinder V_2. After closing of valve S_5, valves S_4, S, are opened and compressed hydrogen from cylinder V_1 flows into operating cylinder V_3, but cylinder V_2 is filled with working fluid.

In the next step, simultaneously with the start of hydrogen compression in cylinder V_2, valve S_4 is closed and valves S_1, S_{10} are opened. This allows filling cylinder V_1 with hydrogen and draining the working fluid from the cylinder. Hydrogen from tank H_2 through open valve S_1 squeezes working fluid from operating cylinder V_1 into tank

T_1 through flow counter D_1 and optical sensor D_4. A signal to close valves S_1, S_{10} will come after the optical sensor D_4 determines that there is an interruption of the working fluid flow in the pipeline. The fluid flow counter D_1 works in the same way as fluid flow counter D_2.

After several repetitive cycles, the hydrogen pressure in operating cylinder V_3 reaches its maximum and becomes equal to the pressure in the cylinders V_1, V_2. After this all valves are closed and valves S_3, S_9 are opened, through which working fluid is supplied to operating cylinder V_3 and compressed hydrogen enters buffer cylinder V_4. The degree of compression of hydrogen in cylinder V_3 is regulated by supply of working fluid, the volume of which is determined by the fluid flow counter D_3.

Valves S_3, S_9 are closed after hydrogen has been removed from cylinder V_3, from which the working fluid is removed via fluid flow counter D_3 and optical sensor D_5. This occurs after opening valve S_8 and repeating the cycle of filling cylinder V_3 with compressed hydrogen from cylinders V_1, V_2. The S_8 valve is closed on a signal from optical sensor D_5, and the fluid flow counter D_3 operates in the same way as counters D_1, D_2.

This completes the pressure booster cycle and the accumulation of hydrogen in buffer cylinder V_4. The compressed hydrogen is supplied via valve S_{13} to the dispenser of the refuelling station.

Valve S_{11} serves for bypass of working fluid flow from pump P_1 outlet in cases when valves S_6, S_7, S_9 are closed, while pump P_1 is still switched on. This allows the working fluid removal from cylinders V_1–V_3 to be completed without stopping the P_1 pump.

The peculiarity of the considered compressor design is the use of fluid flow counters to determine the boundary of the compression cycles, so the hydrogen compression ratio is carried out without the use of fluid level sensors installed in the operating cylinders. The signals used to generate switching commands for the valves can be adjusted according to the operating algorithm and current status of the system.

As a result, the reliability of the device is increased, as the control system is continuously informed about the degree of filling of the operating cylinders with working fluid. At the same time, the information provided by the safety loop makes it possible to avoid emergencies in the event that certain sensors are misguided. In this case, the cyclic process can be restored without returning to the initial state of the device and draining the working fluid into the tank T_1 from the working cylinders.

5. DISCUSSION

In order to achieve mass usage of hydrogen in vehicles, an adequate infrastructure and network of hydrogen refuelling stations are needed. The core element of any such filling station is a booster compressor that can ensure the high pressure of hydrogen up to 100 MPa required for refuelling.

The technical features of the hydraulic compressors are optimally adapted to the basic requirements for use as booster compressors in refuelling stations.

The hydraulic compressor concept proposed by the authors can serve as one of the key components in the technological chain that starts with the hydrogen production by the means of electrolysis of water and concludes with the fuel dispensation at a refuelling station.

The technical solution of controlling the operation cycle of the hydraulic compressor using fluid flow counters proposed by the authors provides for continuous control of the hydrogen compression process, which increases the reliability of the control system.

ACKNOWLEDGEMENTS

The research has been supported by the Latvian Council of Science project lzp-2020/2-0049 "Experimental Studies and Development of Technology on Hydraulic Compression of Hydrogen".

REFERENCES

1. Peschel, A. (2020). Industrial Perspective on Hydrogen Purification, Compression, Storage, and Distribution. *Fuel cells*, *20* (4), 385–393.
2. Fragiacomo, P., & Genovese, M. (2020). Developing a Mathematical Tool for Hydrogen Production, Compression and Storage. *International Journal of Hydrogen Energy*, *45* (35), 17685–17701.
3. European Commission. Communication from the Commission to the European Parliament, the Council, the European Economic and Social Committee and the Committee of the Regions. (2020). *A Hydrogen Strategy for a Climate-Neutral Europe*. Brussels, 8.7.2020. COM (2020) 301 final.
4. Grib, N. (2019). Hydrogen Energy: Myths and Reality. *Oil and Gas Vertical* (in Russian), *19*. 61–69. Available at http://www.ngv.ru/magazines/article/vodorodnaya-energetika-mify-i-realnost/
5. IEA. (2021). Global Hydrogen Review 2021, *IEA*, Paris. Available at https://www.iea.org/reports/global-hydrogen-review-2021
6. Yu, M., Wang, K., & Vredenburg, H. (2021). Insights into Low-Carbon Hydrogen Production Methods: Green, Blue and Aqua Hydrogen. *International Journal of Hydrogen Energy*, *46* (41), 21261–21273.
7. Sdanghi, G., Maranzana, G., Celzard, A., & Fierro, V. (2019). Review of the Current Technologies and Performances of Hydrogen Compression for Stationary and Automotive Applications. *Renewable and Sustainable Energy Reviews*, *102*, 150–170.
8. IEA. (2020). *Global Installed Electrolysis Capacity by Region*, 2015–2020, *IEA*, Paris. Available at https://www.iea.org/data-and-statistics/charts/global-installed-electrolysis-capacity-by-region-2015-2020
9. Ross, D.K. (2006). Hydrogen Storage: The Major Technological Barrier to the Development of Hydrogen Fuel Cell Cars. *Vacuum*, *80* (10), 1084–1089.
10. H2 Tools. (n.d.). *Hydrogen Compressibility at Different Temperatures and Pressures*. Pacific Northwest National Laboratory. Available at https://h2tools.org/hyarc/hydrogen-data/hydrogen-compressibility-different-temperatures-and-pressures
11. Davies, K. L., & Moore, R.M. (2006). *UUV FCEPS Technology Assessment and Design Process*. University of Hawaii.
12. HyResponder Consortium. (n.d.). *Hydrogen Refuelling Stations & Infrastructure*. Available at https://hyresponder.eu/wp-content/uploads/2021/06/L12_HyResponder_L4_210622.pdf
13. Pique, S., Weinberger, B., De-Dianous, V., & Debray, B. (2017). Comparative Study of Regulations, Codes and Standards and Practices on Hydrogen Fuelling Stations. *International Journal of Hydrogen Energy, 42* (11), 7429–7439.

14. Mair, G.W., Thomas, S., Schalau, B., & Wang, B. (2021). Safety Criteria for the Transport of Hydrogen in Permanently Mounted Composite Pressure Vessels. *International Journal of Hydrogen Energy*, *46* (23), 2577–12593.
15. US Department of Energy. (2013). *Hydrogen Delivery Technical Team Roadmap*. Office of Energy Efficiency and Renewable Energy. Available at https://energy.gov/sites/prod/files/2014/03/f12/hdtt_roadmap_june2013.pdf
16. Zou, J., Han, N., Yan, J., Feng, Q., Wang, Y., Zhao, Z., … & Wang, H. (2020). Electrochemical Compression Technologies for High-Pressure Hydrogen: Current Status, Challenges and Perspective. *Electrochem. Energ. Rev., 3*, 690–729.
17. Humphrey, H.A. (1909). An Internal-Combustion Pump and Other Applications of a New Principle. *Proc. Inst. Mech. Eng.,* 1123.
18. Joyce, N.G. (1984). The Humphrey pump – An internal combustion pump. In: *Proceedings of the Conference on Small Engines and Their Fuels in Developing Countries* (pp. 31–44), Reading, Berkshire, England.
19. Van de Ven, J. D., & Li, P.J. (2009). Liquid Piston Gas Compression. *Applied Energy*, 86 (10), 2183–2191. doi:10.1016/j.apenergy.2008.12.001
20. Bezrukovs, V., Bezrukovs, Vl., Bezrukovs, D., Orlova, S., Konuhova, M., Berzins, A., … & Pranskus, P. (2021). *Hydrogen Hydraulic Compression Device*. PCT/IB2021/058102. Application date 13 August 2021.